MXenes as Support for Electrocatalysts towards Oxygen Reduction Reaction in Alkaline Media

PhD Thesis

By **Luc BOUSCARRAT**

Supervisors:

Gaurav GUPTA

Richard DAWSON

Nuno BIMBO

Engineering | Lancaster University

Engineering Department

Lancaster University

ABSTRACT

MXenes as Support for Electrocatalysts towards Oxygen Reduction Reaction in Alkaline Media

Submitted by Luc Jean-Marie André François Bouscarrat

For the degree of Doctor of Philosophy

Lancaster University

December 2022

Due to increasing concerns about the ever increasing energy demand, the global energy system needs to transition away from fossil fuels, as they have been one of the main causes for climate change and air pollution. Fuel cells offer a good alternative to conventional thermal devices, as they usually use hydrogen and oxygen to produce electricity without greenhouse gases emissions. One of the main drawbacks to fuel cell commercialisation is the use of expensive catalysts, such as platinum, and their long-term stability under operation. Therefore, the design and study of cheap and durable catalysts is required to push the development of fuel cells. MXenes, a new family of two-dimensional transition metal carbides and nitrides materials, have shown some potential as support for ORR catalysts. However, the performance of electrocatalysts is directly related to the available surface where the electrochemical reaction could take place, and MXenes have pretty low specific surface areas compared to conventional supports used in the field of catalysis.

This thesis reports the development of a synthesis method focused on improving the final catalyst surface area using MXene (Ti_3C_2) as support, by intercalating the precursors between the MXene layers before annealing. This is shown to lead to the formation of porous MXene structures, with increased surface area and decomposition products from the precursors on the surface of the MXene layers, which hindered the MXene layer restacking during thermal treatment. The samples where then tested in a three-electrode setup using the RDE method to evaluate the ORR performance of the synthesized materials. It was found that the addition of the precursors improved the overall performance of the materials. The different samples were also characterized to understand the connection between physico-chemical properties and electrochemical properties.

ACKNOWLEDGMENTS

The work done in this thesis would not have been possible without the support and patience of my supervisors: Dr Nuno Bimbo, Dr Gaurav Gupta and Dr Richard Dawson. Their guidance and feedback throughout the thesis have been a great help. I am also grateful to Phil Maughan, which has helped me with the synthesis of the MXenes and has always been keen on discussing our respective work with MXene materials. I would also like to thank the other PhD students, postdocs and professors who had time to spare to discuss research topics.

I would like to express my gratitude to Peter Jones and Jessica Fisher, who always made sure the equipment was up and running and the labs tidy. Dr Nathan Halcovitch and Dr Sara Baldock have trained me with the XRS and SEM equipment available at Lancaster University and have always been available when I needed advice related to this equipment. I would like to thank Professor Paul Bingham from Sheffield Hallam University, who made the Mössbaeur equipment from SHU available to test some of my samples.

I would finally like to thank my family and friends for their undying support throughout my PhD. They have helped me push through during the moment when I was doubting myself. A special thank you goes to Catalina, who always believed in me.

DECLARATION OF AUTHORSHIP

The work presented in this thesis was carried out by the author with the supervision of his academic supervisors: Dr Richard Dawson and Dr Nuno Bimbo, except for the following exceptions.

XPS measurements were carried out by Dr Shaoliang Guan at the National XPS facility at Harwell Campus. The deconvolution and analysis were done by the author.

Mössbaeur experiments and the peak fittings were carried out by Alex Scrimshire from the Materials and Research Institute of Sheffield Hallam University. The analysis of the measurements was done by the author.

The work presented has not been submitted in substantially the same form for the award of a higher degree elsewhere.

Whenever the work of others has been quoted, the sources has always been given.

Luc Bouscarrat

TABLE OF CONTENTS

LIST OF ABBREVIATIONS

ADT	Accelerated Durability Test
AEMFC	Anion-Exchange Membrane Fuel Cell
AFC	Alkaline Fuel Cell
BE	Binding Energy
BET	Brunauer, Emmett and Teller (characterization)
CHP	Combined Heat and Power
CL	Catalyst Layer
CNF	Carbon nanofiber
CNT	Carbon Nanotube
DEFC	Direct Ethanol Fuel Cell
DMFC	Direct Methanol Fuel Cell
ECSA	Electrochemical Surface Area
EDL	Electrostatic Double-Layer
EDS	Energy Dispersive X-ray Spectroscopy
FWHM	Full width at Half Maximum
GDL	Gas Diffusion Layer
HER	Hydrogen Evolution Reaction
HF	Hydrofluoric acid
HT-PEMFC	High Temperature Proton-Exchange Membrane Fuel Cell
KE	Kinetic Energy
LT-PEMFC	Low Temperature Proton-Exchange Membrane Fuel Cell
MCFC	Molten Carbonate Fuel Cell
MEA	Membrane Electrode Assembly
MSI	Metal-Support Interaction
NRR	Nitrogen Reduction Reaction
OER	Oxygen Evolution Reaction
ORR	Oxygen Reduction Reaction
PAFC	Phosphoric Acid Fuel Cell
PBI	Polybenzimidazole
PEMFC	Proton-Exchange Membrane Fuel Cell
RDE	Rotating Disk Electrode
RHE	Reference Hydrogen Electrode
RRDE	Rotating Ring-Disk Electrode
RT	Room Temperature
SCE	Saturated Calomel Electrode
SEM	Scanning Electron Microscopy

SHE	Standard Hydrogen Electrode
SOFC	Solid Oxide Fuel Cell
SSA	Specific Surface Area
TMD	Transition Metal Dichalcogenide
TPB	Triple phase boundary
XPS	X-Ray Photoelectron Spectroscopy
XRD	X-Ray Diffraction

LIST OF FIGURES

14

LIST OF TABLES

CHAPTER 1: Introduction

1.1. Scope and motivation

The hydrogen economy and fuel cells have seen an increasing interest in the past few years, along with other low-carbon technologies, due to increasing worldwide concerns about the use of fossil fuels. The main concern is environmental, as the greenhouse gas emissions produced by the fossil fuels have shown to have drastic and irreversible consequences on climate and ecosystems. Moreover, other emissions coming from the use of fossil fuels, such as nitrous oxide and particulates, have shown to degrade air quality, especially in highly populated areas, which is a global health concern. Finally, due to the finite nature of fossil fuels, there is a need to develop "green", non-fossil fuel energy sources to be able to meet an ever increasing global energy demand. Hydrogen and fuel cells, combined with other "green energy" technologies, could become an alternative to fossil fuels and help reduce the impact of the increasing energy demand on the environment.

Fuel cells are a type of electrochemical devices, in which oxygen and a fuel, typically hydrogen, react at the cathode and anode, respectively, to produce electricity and by-products (H_2O in the case of hydrogen fuel). The oxygen is reduced at the cathode, while hydrogen is oxidized at the anode. Both of these reactions require the presence of catalysts on the electrodes to improve the overall performance of the fuel cell. The oxygen reduction reaction (ORR) plays a key role in term of performance, as it has sluggish reaction kinetics compared to hydrogen oxidation reaction (HOR). Therefore, it is usually a necessity to use a higher amount of catalyst on the cathode side of the fuel cell to be able to overcome the sluggish kinetics of ORR. The catalyst most commonly used in fuel cell for ORR is platinum, usually in the form of Pt nanoparticles on a carbon support. One of the bottlenecks in term of fuel cell development comes from this Pt/C catalyst. Although platinum being one of the best materials to catalyse ORR, it is also a very expensive materials, which hinders the commercialization of fuel cells. Moreover, some stability issues arise during fuel cell operation, such as carbon support corrosion, Pt particles dissolution, aggregation, and Ostwald ripening, which result in a degradation of the fuel cell performance in the long term. It is therefore important to develop cost-effective and durable cathode catalysts with similar performance than the Pt/C benchmark. While the development of cheap ORR electrocatalysts with good activities is challenging, certain fuel cell types, such as alkaline fuel cells (AFC), allow a broader range of materials to be used as catalysts. Indeed, alkaline electrolytes presents two advantages compared to acidic electrolytes. First, the ORR kinetics are better in alkaline media,

which opens up the use of a variety of other catalysts. And second, the chemical stability of these catalysts is better in alkaline media than they are in an acidic environment.

This thesis investigates a new family of materials discovered in 2011, called MXenes, and their applications towards ORR in alkaline media. MXenes are a family of two-dimensional layered transition metal carbides and nitrides, which have shown to have some great potential in electrochemical applications. Compared to conventional materials used in fuel cell catalyst layers, MXene have a pretty small surface area and the MXene layers can also re-stack closely together which would hinder accessibility of the MXene surface for electrochemical reactions. Therefore, methods to obtain MXene (Ti_3C_2) based materials with greater surface area are investigated to obtain cathode composite materials for AFCs. More specifically, a focus is set on improving the final materials surface area, while using the MXene as a support for the synthesis, with the aim to improve the ORR activity of the materials.

1.2. Structure of thesis

This thesis is split into seven chapters:

Chapter 1 introduces the motivation and the structure of the thesis.

Chapter 2 defines the background of the thesis by introducing concepts about energy conversion and storage, specifically on fuel cells, the different types of fuel cells and their particularities. More emphasis is given to ORR mechanisms in alkaline media and the range of catalysts available for ORR in AFCs. MXenes synthesis and applications towards ORR are also going to be reviewed. This chapter does not aim to be a thorough review of all works done on these topics, but focuses on pertinent concepts and studies, which would help with the understanding of the content of this thesis.

Chapter 3 defines and describes the materials and methods used during the synthesis, as well as the characterization of the different samples. The different characterization methods are also briefly introduced and explained to allow a better understanding of interpretations of the results reported in chapter 4, 5 and 6.

Chapter 4 reports the synthesis and physico-chemical characterization of Ti_3C_2 MXene treated with urea. First, the initial MXene synthesis and intercalation is described. Then, several characterization techniques, such as XRD, SEM, BET and XPS, are used in order to understand the influence of the urea content, as well as the temperature of the thermal treatment on the bulk and surface chemistries, and on the morphology of the synthesized samples.

Chapter 5 focuses on the electrochemical characterization of the samples synthesized in chapter 4. The main objective of this chapter is to evaluate the ORR performance of the different samples

and to link the results with the physico-chemical characterization done previously whenever possible.

Chapter 6, based on the results obtained in chapter 4 and 5, investigates the introduction of $FeCl_3$ as precursor for Fe-species during the synthesis process. Several characterization techniques (XRD, Mössbauer spectroscopy, SEM, BET, XPS…) are used to determine the influence of the precursor introduction on the chemistry and morphology of the samples. Moreover, the influence of using Ti_3C_2 as support is investigated by synthesizing a reference sample using XC72-R carbon instead of MXene. Electrochemical characterization is then performed on the materials to evaluate their performance towards ORR in alkaline media.

Chapter 7 summarises the results presented in the results chapters, draws main conclusions of the work done in this thesis and gives some recommendations for future work.

CHAPTER 2: Background

2.1. Introduction

This chapter is going to introduce the main background and various concepts concerning electrochemical energy conversion, as well as fuel cells materials' synthesis and their electrochemical properties. As this thesis investigates the use of MXenes for alkaline fuel cells (AFC) applications, this chapter is going to briefly review fuel cells, oxygen reduction reaction (ORR) mechanisms in alkaline media, materials used as supports or/and catalysts in the electrodes, as well as MXenes synthesis and their different electrochemical/catalytic applications that have been investigated so far.

2.2. Electrochemical energy conversion

Electrochemical energy conversion devices can be found everywhere in today's world, from batteries and supercapacitors which both store and convert energy, to fuel cells and electrolysers, and other electrochemical or photoelectrochemical processes. Electrochemical energy conversion is defined as follows: it is the conversion of electrical energy into chemical energy and/or the conversion of chemical energy into electrical energy. During this operation, at least two reaction pairs undergo a chemical transformation.[1] Electrochemistry has been a field that has taken more and more importance in the world over the past years, especially due to a growing need for improved mobile technologies and the development of batteries for electronic applications. In the past decades, due to the growing public awareness of the climate urgency and due to governments starting to pass policies to reduce their environmental impact, in additions to climate targets set nationally or internationally, the electrochemistry field has shown more and more diversification in term of research areas, such as supercapacitors, different chemistries in batteries and biological electrochemical systems.[2] Even fuel cells and electrolysers have seen a growing interest for a wider range of applications. This diversification allows for more flexibility in systems and end-products design.
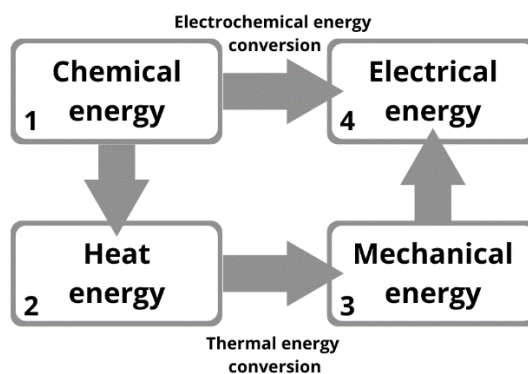
Figure 2.1: Comparison between electrochemical energy conversion and classic thermal energy conversion to produce electricity

Electrochemical conversion systems differ from the usual thermal systems. Indeed, electrochemical conversion devices are direct conversion systems, as the energy conversion occurs without intermediate steps, while thermal systems are indirect systems, as shown on Figure 2.1.[1] To produce electricity in a usual thermal power plant for example, the combustion of a fuel is required to produce heat, which will be used to heat up water into steam, which then used to drive an electrical generator to produce electricity. On the contrary, based on the different mechanisms involved, electrochemical conversion is directly transforming chemical energy into electrical energy through an electrochemical reaction. Another advantage of electrochemical conversion is that its efficiency is not limited by the Carnot cycle efficiency, which is the case for thermal conversion systems. In the next sections, important types of electrochemical conversion systems are going to be introduced, namely batteries, supercapacitors, and fuel cells / electrolysers. Fuel cells are going to be further discussed, as they are the systems of interest for this thesis.

2.2.1. Batteries

Batteries are the most common electrochemical energy conversion and storage devices currently in use. Batteries can be mostly divided into two types: primary and secondary batteries. Primary batteries cannot be electrically recharged, but they have high energy density and good storage characteristics. Secondary batteries can be electrically charged and therefore bring an advantage in term of costs. Batteries are closed systems, in which the two electrodes are involved in the charge-transfer mechanisms and in the energy storage. Therefore, conversion and storage of energy happens in the same system. The energy storage in batteries happens in the bulk of the materials, leading to high energy density devices, but usually the reaction kinetics are quite slow compared to some other electrochemical devices.[3]

There is a wide variety of batteries available on the market and/or studied for research. Portable electronic devices have been the main driver for quick development of batteries, and the four main types of rechargeable batteries for these devices are: lead-acid batteries, Ni-Cd batteries, Ni-MH batteries and Li-ion batteries, which are the most used nowadays.[4] Other types of batteries have gotten more traction in the research field, such as metal-ion systems (Na-ion, Mg-ion, Zn-ion…)[5,6], metal-air systems (Li-air and Zn-air)[7-9], redox flow batteries[10] and others. These technologies are based on different mechanisms, chemistries and processes, leading to different properties, such as energy densities and power densities, and they have different degradation. Depending on the applications, different technologies may be preferred. It is interesting to note that metal-air batteries, while being a completely different system to fuel cells, are based on common mechanisms at the cathode (the air side) where the oxygen is reduced. Therefore, similarities can be drawn in term of materials and electrocatalysts to some extent.

2.2.2. Supercapacitors

Supercapacitors (electrochemical capacitors) are a type of electrochemical system that bridges the gap between conventional capacitors and batteries. Indeed, they usually have higher specific power, but lower energy density compared to batteries, while having lower specific power and higher energy density compared to capacitors.

Supercapacitors differ from batteries due to the differences in mechanisms involved in charge storage in these devices. While batteries energy storage happens in the bulk, as mentioned earlier, supercapacitor technologies are based on different storage mechanisms, electrical double-layer capacitance and electrochemical capacitance, which are more superficial storage mechanisms. It leads to lower energy densities since not all of the material is participating in the charge storage but allows for faster reaction kinetics and higher specific power. This can be beneficial for applications which require quicker charge transfer, rather than a compact energy storage. The three different types of supercapacitors are as follows:[11]

- Electrical double-layer (EDL) capacitors: the basic principle is to store the electrical energy through the formation of an electric double layer at the electrode-electrolyte interface. The EDL is a structure that forms at the surface of the solid when it is exposed to a liquid. To counteract the accumulated charges on the surface of the solid, the ions of opposite charge contained in the liquid self-organise at the interface in the electrolyte. During charging and discharging, a charge imbalance is created at both electrodes and the anions and cations form an EDL at the surface of both electrodes.

- Pseudocapacitors: unlike EDL capacitors, pseudocapacitors have highly reversible chemical reactions happening at the electrode, which allow charge storage at the surface

of the electrode. Pseudocapacitors can have a capacitance up to 100 times higher than regular EDL capacitors, but usually have a lower power density due to slower charge storage mechanisms comparatively.

- Hybrid capacitors: these supercapacitors store the electrical energy through both EDL and pseudocapacitives mechanisms.

2.2.3. Fuel cells and electrolysers

2.2.3.1. Introduction

Fuel cell history started in 1839 when William Groove generated electricity from hydrogen and oxygen by reversing water electrolysis: the basic principle of fuel cells was discovered.[1,12] Since then, numerous studies in the field of fuel cells have been undertaken and different technologies have been developed, but the principle remains the same: a fuel cell is an electrochemical system which allows the conversion of the chemical energy into electrical energy, as long as fuel and oxidant are supplied. Fuel cells are galvanic cells, in which the free energy of a chemical reaction is converted into electrical energy. It differs from batteries and supercapacitors, as it does the conversion of chemical energy stored in fuels into electrical energy, and therefore, electricity can be produced a long as fuels are fed to the device. On the other hand, a fuel cell does not store energy, it just converts it: fuel cells are open systems. In that aspect, a fuel cell is comparable to a combustion engine, except that a combustion engine converts chemical energy into useful mechanical work, which has a limited efficiency compared to electrochemical conversion.

Fuel cells have been widely studied, resulting in the development of a wide range of technologies. Different types of fuel cells currently exist; they are usually classified by the type of electrolyte used. Some of the mechanisms involved differ from one type of fuel cell to the other, but they all function in the same basic way. At the anode, a fuel is oxidized, and at the cathode, an oxidant is reduced. Then either protons or oxide ions, depending on the type of fuel cell, are transported through the ion conducting but electrically insulating electrolyte, to combine with either oxide or protons to generate electricity.

As electrolysers are not the focus of this study, only a brief introduction is going to be given. Electrolysers, and in particular water electrolysers, are based on the opposite principle compared to fuel cells. They require an applied potential which forces a non-spontaneous electrochemical reaction to happen at the electrodes. In the case of water electrolysers, electrical energy is used to split water molecules into H_2 and O_2. The hydrogen produced is used to store energy and then can be used as fuel to produce electricity using fuel cells when needed.

2.2.3.2. Fuel cell types

This section presents the main types of fuel cells. Although fuel cells are based on the same underlying electrochemical principles, they function at different operating temperatures or conditions (fuel purity, fuel chemistries…) and require different materials for their components. A summary of the principal characteristics of the major fuel cells is given in Table 2.1. Moreover Figure 2.2 is a schematic summarizing different fuel cell types and the various species involved during operation.
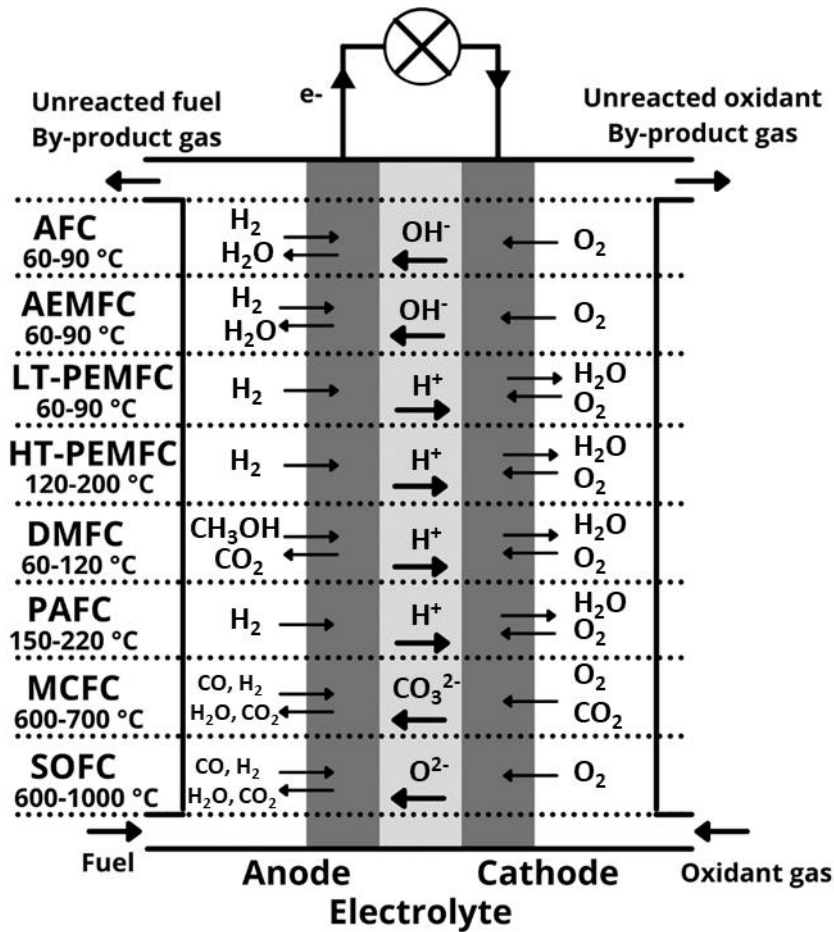
Figure 2.2: Schematic of the reactions and processes involved in common fuel cells [13]

Alkaline fuel cell (AFC):

AFCs are one of the oldest fuel cell systems designed. They were developed as primary electric power supply for the Apollo space missions in the 1960s. The reactions happening during AFC operation are:

At the anode: $H_2 + 2OH^- \rightarrow 2H_2O + 2e^-$

At the cathode: $\frac{1}{2}O_2 + 2e^- + H_2O \rightarrow 2OH^-$
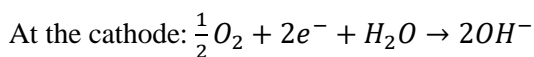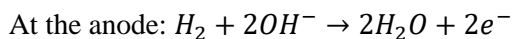
AFCs use an aqueous solution of potassium hydroxide (KOH) or sodium hydroxide (NaOH) as the electrolyte, as they are highly soluble and low cost. The most commonly used as electrolyte is KOH with a concentration around 30-50wt%. The temperature range for an operating AFC can go from 60°C to 90°C, depending on the KOH concentration of the electrolyte. During operation, the transported ions in the electrolyte are hydroxide ions (OH⁻), from the cathode to the anode. In the end, electricity, as well as by-product water and heat are produced. Excess water and heat need to be removed to keep the cell in favourable working conditions. Indeed, if water is not removed from the system, the electrolyte ends up less and less concentrated, and would lead to performance degradation due to the ions' conductivity losses.

An important advantage concerning AFCs is that the O_2 reduction kinetics at the cathode in alkaline electrolytes is faster than in acid electrolytes. Electrochemically, it means that the activation voltage obtained at the cathode in alkaline electrolytes is usually lower than in acid electrolytes, although the mechanisms behind it are still not well understood. Another advantage is due to the fact that there are more metal-based catalysts which are stable in alkaline media compared to acid environment. It opens the possibility to use non-noble metals as catalysts especially for oxygen reduction reaction (ORR), such as nickel (Ni), instead of platinum (Pt), making the electrodes fabrication process a lot cheaper than for other types of fuel cells. The different ORR catalysts available for AFCs, either commercially available or academically studied, are going to be covered in another part of this chapter. (Section 2.3.3)

One of the biggest issues with AFCs is the need to use almost pure H_2 and O_2 (or purified air) reactants. Indeed, AFCs are really sensitive to impurities, especially carbon dioxide poisoning.[14,15] In the presence of CO_2, OH⁻ ions react and form carbonates, following the reactions:

$$CO_2 + 2OH^- \rightarrow (CO_3)^{2-} + H_2O$$

$$CO_2 + 2KOH \rightarrow K_2CO_3 + H_2O$$
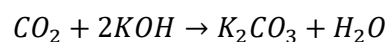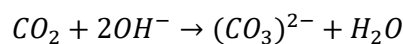
The formed carbonates can then precipitate (K_2CO_3) due to its lower solubility and several problems can occur in the operating fuel cell. First, it will reduce the concentration of hydroxyl ions, limiting the ion conductivity of the electrolyte solution. The precipitates can also obstruct the pores in the electrodes, limiting the gas influx.

Proton-exchange membrane fuel cell (PEMFC):

In the case of PEMFCs, the ions that are transported in the electrolyte are protons (H⁺) and are formed at the anode and transported to the cathode, where they react to form by-product water and heat. PEMFCs use a thin proton-conducting polymer membrane (20-200 µm) as an electrolyte, which is between the 2 electrodes, to form the membrane electrode assembly (MEA)

(<1 mm thick). The MEA consists of the polymer membrane, the electrodes and the gas diffusion layer (GDL). The most common polymer used for low temperature PEMFCs (LT-PEMFC) is Nafion. Due to the membrane requiring to be hydrated by water to maintain sufficient proton conductivity, the operating temperature is restricted to the 60-90 °C range. To overcome this temperature window restriction, another type of PEMFC has been developed and labelled high-temperature PEMFC (HT-PEMFC). HT-PEMFCs rely on another type of polymer to make their membranes, which does not need to be hydrated to keep a high proton conductivity. The membrane is usually made out of acid-doped PBI (Polybenzimidazole).[16,17]

The reactions involved in an operating PEMFC are:

At the anode: $H_2 \rightarrow 2H^+ + 2e^-$

At the cathode: $\frac{1}{2}O_2 + 2H^+ + 2e^- \rightarrow H_2O$
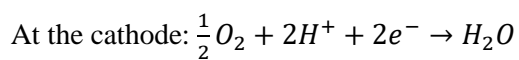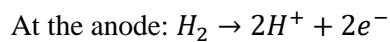
Anion-exchange membrane fuel cell (AEMFC):

AEMFCs are a type of fuel cell that have attracted more and more attention, as they share some of the AFCs advantages compared to PEMFCs, while having a similar stack design as PEMFCs. Indeed, AEMFCs are also made of a MEA, but the polymer membrane is in an alkaline environment, which allows the crossing of OH⁻ species instead. Some of the polymer membranes that have been developed and proposed for AEMs are based on polyphenylene oxide (PPO)[18], poly(ether ether ketone) (PEEK)[19], and others.[20,21] Similar to AFCs, oxygen is reduced at the cathode to form OH⁻ ions, which are transported through the membrane to the anode, where the fuel is oxidized to generate water and heat. But unlike AFCs, AEMFCs allow the use of a wider range of fuels in addition to H_2, such as ethanol and methanol for instance.[21]

Phosphoric acid fuel cell (PAFC):

Phosphoric acid FCs are considered to be the first generation of commercial fuel cells. PAFCs use highly concentrated phosphoric acid as electrolyte (H_3PO_4). The electrolyte is stabilised using a SiC-based matrix. During operation of a PAFC, H_2 is used as fuel at the anode and O_2 or air is used as the oxidant at the cathode. The half-reactions happening at the electrodes are the following:

At the anode: $H_2 \rightarrow 2H^+ + 2e^-$

At the cathode: $\frac{1}{2}O_2 + 2H^+ + 2e^- \rightarrow H_2O$
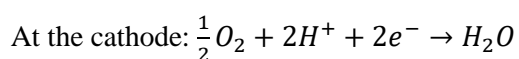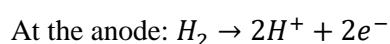
PAFCs have a major advantage compared to PEMFCs. This type of fuel cell has a better tolerance to CO compared to PEMFCS, as the tolerance to CO increases slightly with increasing temperature.

Molten carbonate fuel cell (MCFC):

In the case of the MCFC, CO_2 and O_2 react at the cathode to form CO_3^{2-}, the charge carrier going through the electrolyte. CO_3^{2-} travels from the cathode to the anode to combine with hydrogen to form H_2O and release electrons. The reactions involved in a MCFC are quite different from the previous fuel cells:[1]

At the anode: $H_2 + {CO_3}^{2-} \rightarrow CO_2 + H_2O + 2e^-$

At the cathode: $\frac{1}{2}O_2 + CO_2 + 2e^- \rightarrow {CO_3}^{2-}$
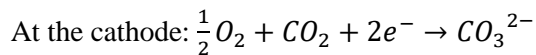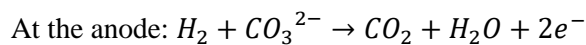
This type of fuel cells operates at temperature ranging from 600 to 700 °C and can therefore use cheaper catalyst like Nickel as it has sufficient activity towards ORR at these high temperature range. Moreover, MCFCs can use a wider range of fuels, such as CO, which can be reformed internally. The main drawbacks come from the high operating temperature as well, as it raises a lot of engineering problems. MCFCs require the use of expensive materials to achieve good chemical and mechanical stability.

Solid oxide fuel cell (SOFC):

SOFCs are fuel cells using solid, non-porous ceramic as electrolyte. The specific requirement of SOFCs electrolyte materials is that they need to conduct oxygen ions from the cathode to the anode. In general, the most common material used as electrolyte is yttria-stabilized zirconia which conducts oxygen via oxygen vacancies.[22] The electrochemical reactions at the cathode and anode are as follow:

At the anode: $H_2 + O^{2-} \rightarrow H_2O + 2e^-$

At the cathode: $\frac{1}{2}O_2 + 2e^- \rightarrow O^{2-}$
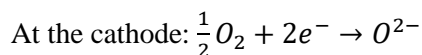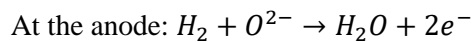
They operate at high temperature, which range from 600 to 1000°C. The high operating temperature allows the use of a wider range of fuels, as well as better resistance to contamination/poisoning, and leads to higher efficiencies compared to low temperature fuel cells, especially if the waste heat is recycled and used in combined heat and power (CHP) systems. Indeed, the usual electrical efficiency of SOFCs is around 50 to 60% in a classic system and can go up to around 70% in SOFC/gas-turbine systems. Moreover, the overall efficiency can reach

up to over 80% when used in CHP applications.[23,24] The issues coming with high operating temperatures are mostly materials related. Indeed, the materials used for SOFC are very specific and needs to have good mechanical properties, similar thermal expansion properties and good chemical and electrochemical stabilities in extreme thermal conditions.

Table 2.1: Characteristics of the principal fuel cells technologies[1,12,13,16,21,25]

Fuel cell type	Electrolyte	Charge carrier	Fuel	Operating temperature	Power range	Main Applications
AFC	Aqueous KOH (NaOH)	OH^-	Pure H_2	60-90 °C	5-150 kW	Space Military
AEMFC	Polymer matrix (PPO, PEEK, PBI…)	OH^-	Pure H_2 Methanol Ethanol	60-90 °C	-	Automotive portable
PEMFC	Polymer matrix (LT: Nafion) (HT: PBI)	H^+	Pure H_2	LT: 60-90 °C HT: 120-200 °C	<1-250 kW	Automotive portable
DMFC (DEFC)	Polymer matrix (Nafion)	H^+	Methanol (Ethanol)	60-120 °C	<1-100 kW	Automotive portable
PAFC	Phosphoric acid in SiC matrix	H^+	Pure H_2 (tolerates 1.5% CO)	150-220 °C	50-1000 kW	Power CHP
MCFC	Molten Li_2CO_3 in $LiAlO_2^-$	CO_3^{2-}	H_2, CO, CH_4, …	600-700 °C	<1-1000 kW	Power CHP
SOFC	Y_2O_3-stabilized or Y_2O_3/CaO-stabilized zirconia	O^{2-}	H_2, CO, CH_4, …	600-1000 °C	<1-3000 kW	Power CHP

As described in the previous section, based on several technologies, fuel cell systems have a wide range of properties which are available depending on the needs of specific applications. The advantages and disadvantages of specific fuel cell technologies have already been discussed when the different fuel cell types have been introduced, and a brief summary is given in Table 2.2. It shows clearly that the choice of a specific fuel cell technology is critical when designing a system and is highly dependent on the end application.

Table 2.2: Main advantages and disadvantages of different fuel cell types[1,12,13,16,21,25]

Fuel cell type	Advantages		Disadvantages
AFC	+	Better cathode performance	- KOH sensitive to CO_2 poisoning
	+	Non-precious metal catalysts	- Needs water removal at the cathode
	+	Low cost	
AEMFC	+	Better cathode performance	- Requires water management
	+	Non-precious metal catalyst	- CO_2 poisoning
	+	Low cost	
	+	Wider choice of fuel	
PEMFC	+	High power density	- Expensive commercial catalyst (Pt)
	+	Low temperature	- More expensive components
	+	Good start-stop capabilities	- Requires water management
			- Poisoning by CO and S
PAFC	+	Better CO tolerance compared to PEMFCs	- Highly corrosive electrolyte
			- Lower power density
			- Expensive materials
MCFC	+	Fuel flexibility	- Requires CO_2 recycling
	+	Non-precious metal catalysts	- Expensive materials/components
		Waste heat can be used for CHP	- Hazardous electrolyte (molten, corrosive)
			- Degradation issues
SOFC	+	Fuel flexibility	- Expensive materials/components
	+	Non-precious metal catalysts	- High-temperature issues
	+	Waste heat can be used for CHP	
	+	Solid electrolyte	
	+	High power density	

2.3. Oxygen reduction reaction

The oxygen reduction reaction (ORR) is one of the most studied reactions in the area of electrochemistry, due to its key role in various electrochemical energy conversion and storage devices, especially in fuel cells and metal-air batteries. The ORR is a crucial reaction for these devices because it is the limiting step amongst the reactions involved due to its sluggish kinetics compared to the oxidation of the fuel or metal happening at the anode. Due to the sluggish and highly irreversible nature of ORR, it is required to use electrocatalysts on the cathode, where the reaction happens, to minimize as much as possible the overpotential necessary to start the reaction. Despite ORR mechanisms having been widely and thoroughly studied, they are still not completely understood due to their complexity and the various steps and reactions involved, which also depend on the medium the ORR is done and /or the various species and catalysts involved.

2.3.1. ORR principles in alkaline media

In aqueous electrolytes, the ORR happening at the cathode goes through several steps:

- The diffusion and adsorption of O_2 molecules on the surface of electrocatalysts,
- The electron transport from the anode to the adsorbed O_2 molecule,
- The O=O bindings weakening and splitting,
- The products of the reduction (OH⁻ ions) being removed into the electrolyte.

The reduction of O_2 to OH⁻ ions can proceed either through a highly efficient one step process via a 4-electron pathway or a sluggish two steps process via a 2-electron pathway.[26]

In the case of alkaline electrolyte, the 4-electron pathway is as follows:

$$O_2 + 2H_2O + 4e^- \rightarrow 4OH^- \ (0.401\ V\ vs\ SHE)$$

<div align="right">Eq. 2.1</div>
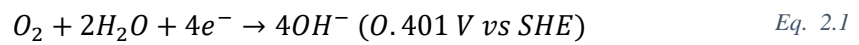
where SHE stands for standard hydrogen electrode.

The 2-electron pathway follows the first steps described in Eq. 2.2 with HO_2^- as a product, followed by either a further reduction of HO_2^- into OH⁻ (Eq. 2.3) or its chemical disproportionation (Eq. 2.4).

$$O_2 + H_2O + 2e^- \rightarrow HO_2^- \ (-0.076\ V\ vs\ SHE)$$

<div align="right">Eq. 2.2</div>

$$HO_2^- + H_2O + 2e^- \rightarrow 3OH^- \ (0.878\ V\ vs\ SHE)$$

<div align="right">Eq. 2.3</div>

$$2HO_2^- \rightarrow 2HO^- + O_2$$

<div align="right">Eq. 2.4</div>
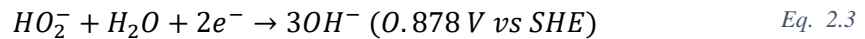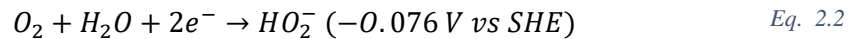
2.3.2. Cathode materials for AFCs

The cathode of the fuel cell is composed of several layers, which all play an important role for the good operation of the device. A basic schematic of a fuel cell electrode is shown in Figure 2.3, and it consists of three components: the current collector, the gas diffusion layer (GDL) and the catalyst layer (CL).[27]
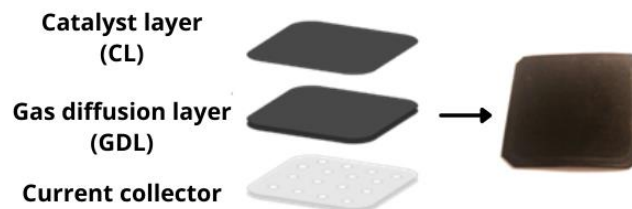
Figure 2.3: Schematic of a fuel cell electrode

- The current collector, also called backing material, is usually a metal mesh (mostly steel or nickel based), which allows the good electrical connectivity of the cell with the rest of the system. The current collector needs to have a high permeability to gases, to allow

hydrogen (anode) and air/O$_2$ (cathode) to pass through, a high electrical conductivity, as well as a good resistance to corrosion and a good structural integrity, as it is the backbone of the electrode.

- The gas diffusion layer (GDL) has two main purposes: it needs to allow the flow of reactant gas from the feed to the CL while stopping the electrolyte from crossing the cathode to prevent the flooding of the fuel cell system. The GDL also requires to be electrically conductive. Therefore, it is usually made of a mix of PTFE for its hydrophobic properties and carbons to increase the electrical conductivity of the final GDL composite. Ideally the GDL should have a high electrical conductivity and be hydrophobic, but it is usually a trade-off between the two and tuning of the composition is required.

- The catalyst layer (CL) is the electroactive layer, where the electrochemical reactions are going to take place, more especially at triple phase boundaries (TPB), as shown in Figure 2.4. It contains the electrocatalyst, a carbon support material, usually carbon black, which allows the transfer of electrons between the catalyst particles and the rest of the fuel cell system, and PTFE as a binding agent to give integrity to the CL. The PTFE, with its hydrophobic properties, also provides more TPBs where gas, electrolyte, and electrocatalyst particles meet. The composition of the CL should therefore allow good gas transport, ionic transport (OH$^-$ products in the CL at the cathode side), and a high electronic conductivity. In general, the amount of PTFE in the CL is much lower than in the GDL, due to the high electronic conductivity necessary.
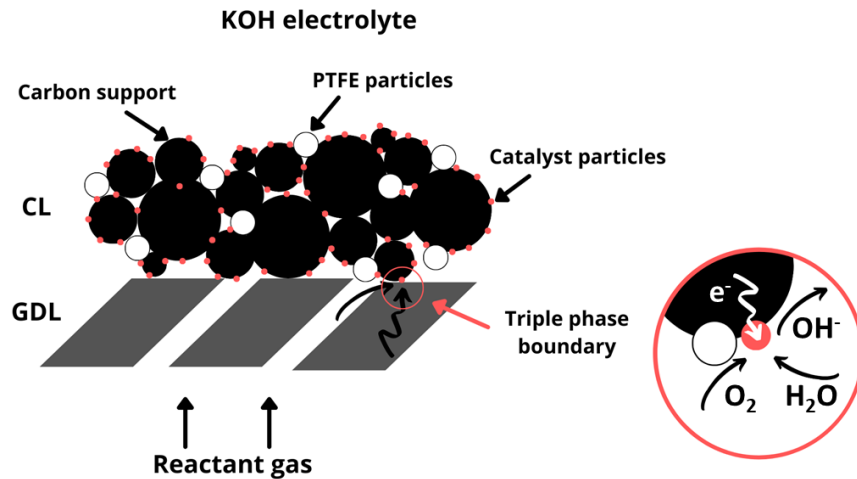
Figure 2.4: Schematic of the catalyst layer and the triple phase boundary at the cathode side of an AFC

In this part and the rest of this thesis, we will focus on materials used in the cathode's CL of an AFC, and especially on the catalyst materials, where the ORR happens during operation. To

design electrocatalyst materials, several characteristics need to be considered. Indeed, materials need to meet some requirements to be used as ORR electro-catalysts. They need to possess:

- **high catalytic activity towards ORR**: having a high catalytic activity which is intrinsic to the materials is the first box to tick when it comes to design electrocatalysts. For ORR the reference catalyst is platinum (Pt), used in practice as Pt nanoparticles on porous carbon support materials (Pt/C). Activity towards ORR is usually measured as mass activities ($mA.g_{Pt}^{-1}$) or surface activity ($mA.cm_{Pt}^{-2}$), especially for Pt-based catalyst and would be measured at 0.9V vs RHE. Other factors can be used to evaluate the performance of a catalyst towards ORR, such as the

- **high electrical conductivity**: The CL needs to be electrically conductive to allow for fast and efficient electron transfer. If the materials in the CL have high electrical resistance, the internal resistance of the fuel cell will be high, leading to power loss due to a larger iR drop, which will reduce the overall efficiency of the fuel cell.

  Preferably, both the catalyst particles and the support materials must have good electrical conductivity to allow fast electron transfer, for instance Pt/C catalysts. But materials which meet the other condition of being a good electrocatalyst towards ORR do not always have good electrical conductivity, such as some metal oxides like Co_3O_4[28], metal oxide-supported catalysts like Pt/NbO_x[29] or other type of catalysts/supports which will be discussed later. In this case, due to the low electrical conductivity of the materials, it is necessary to use a conductive support (usually carbon-based) or in the case of metal oxides used as support, to design composite support materials, made of the metal oxide and another conductive support. The conductive support allows the final electrocatalyst to have higher electrical conductivity but can also increase the intrinsic activity of the materials through metal-support interactions (MSI).

- **high chemical/electrochemical stability**: As described previously, the electrolyte used in fuel cells is either strongly acidic or basic, with the presence of oxygen, which is a highly oxidizing agent, at the cathode. The electrochemical stability of the electrocatalyst, both the catalyst particles and the support, is vital in practice. Indeed, the potential at the cathode will usually be higher than the oxidation potentials of most metals and carbon materials. That's why the materials chosen for the cathode must be so they have slow kinetics of oxidation in the operation conditions of the fuel cells.

- **preferential morphology**: The morphology of an electrocatalysts has a great influence on how well the materials is going to perform. Indeed, the materials composition (catalyst

particles to support materials ratio…), the particles size and shape, the total surface area available, as well as the electrochemical surface area, the porosity, the particles distribution, and other morphological properties of the materials are going to affect the electroactivity of the final electrocatalyst, as well as its durability during operation.

2.3.3. Catalyst materials for AFCs

Using alkaline electrolyte brings a lot of advantages concerning ORR. Indeed, ORR kinetics are more rapid in alkaline media compared to acidic media. Moreover, alkaline media provides a less corrosive environment to some catalysts.[26] Therefore, a wider range of catalysts are available to use for fuel cell applications in alkaline fuel cells. This section gives a very brief summary of the different types of catalyst which can be used in alkaline media and is separated into two parts: precious-metal catalysts and non-(precious metal) catalysts.

2.3.3.1. Precious metal catalysts

The most common material used to catalyse ORR is platinum. The majority of ORR studies have been done on Pt nanoparticles supported on carbon (Pt/C).[30-32] The main factor influencing the ORR activity of Pt nanoparticles is their size, several studies have shown that the activity of Pt/C usually increases when the particle size decreases, until it reaches a particle size (around 3-5 nm), under which the activity decreases.[31,32] This decrease in activity was attributed to excess of HO_2^- formed on the surface, which would not be further reduced.

One way to make fuel cells more efficient and cost-effective is to reduce the amount of Pt used in the catalyst materials. To do this, researchers have focused on creating Pt alloys, which are materials made by mixing Pt with other, less expensive metals.[33] These alloys typically have a layer of pure Pt on top and a core made of Pt mixed with another metal. The Pt layer helps prevent the other metal from dissolving, while the underlying alloy changes the electronic structure of the Pt surface in a way that enhances its activity towards ORR.

As mentioned earlier, the main advantage of using alkaline electrolyte is the possibility to use a wider range of catalysts. Indeed, other precious metal catalysts such as palladium (Pd),[34] gold (Au)[35] and silver (Ag)[36] can be used as catalysts for ORR. They are also designed as nanoparticles on different types of supports, but mostly carbons. Their activities and stabilities are a lot better than in acidic environment, but their performance is on average slightly lower than Pt/C catalysts.

2.3.3.2. Non-(precious metal) catalysts

Non-(precious metal) catalysts available in alkaline media include a variety of different chemistries and structures. The main groups of non-(precious metal) catalysts are the following:

- Hetero atoms (N, B, S, P…) doped carbons. Although carbon structures (carbon black, carbon nanotubes, graphene…) are usually used as support for catalysts, doped carbons have shown to have improved catalytic activities towards ORR in alkaline media. It is believed that the inclusion of the hetero atoms forms active sites with the carbon structure, which helps the O=O bond breaking step of the ORR mechanisms.[37-41]

- Transition metals / N-doped carbon hybrid catalysts. One of the most promising non-precious metal catalysts are M-N-C catalysts. They consist of a N-doped carbon support with transition metals (Fe or Co mostly) which have been integrated onto the support by either forming M-N$_x$ moieties or metal nanoparticles interacting with the N-C support.[42-45]

- Transition metal oxides. Some spinels (Co_3O_4, Mn_3O_4…)[28,46,47] and perovskites ($LaCoO_3$, $LaNiO_3$…)[48-50] have shown to have good catalytic activity towards ORR and good stability in alkaline media. They require to be deposited on carbon supports, as their electrical conductivity is limited.

2.4. MXenes

Since the discovery of graphene in 2004 by Novoselov and Geim[51], the scientific community has shown a growing interest in 2D materials. Due to their particular thickness to lateral size aspect ratio (usually under 5 nm thick with a lateral size >100 nm to a few µm) they show different properties compared to their bulk form. They have exceptional electronic, mechanical, and optical properties compared to bulk materials, enabled by the electron confinement in two dimensions. These 2D materials properties coupled with their high surface area are of interests for specific applications such as sensors, electronics, catalysis, energy storage and conversion. Several 2D materials have been discovered and engineered since then, such as hexagonal boron nitrides,[52] metal oxides/hydroxides,[53] transition metal dichalcogenides (TMDs)[54] or g-C$_3$N$_4$.[55] 2D materials also have been used as building blocks for other materials applications, such as layer by layer structures and mixed composites,[56,57] or for example as support for other materials for structural reasons or to improve the overall properties of the materials for a specific application.

More recently, a group of 2D materials has been discovered by Naguib et al. from Drexel University in 2011.[58] They have received a significant research focus in different fields because of several of their properties, such as hydrophilic surfaces, chemical stabilities, surface

chemistries, and particular physico-chemical and electrical properties. They have principally been investigated for energy storage applications such as batteries and supercapacitors applications,[59-63] but have also found applications in catalysis,[64,65] sensors[66,67] and more.

2.4.1. Background on MXenes

The MXenes are a family of materials with chemical formula $M_{n+1}X_n$ (n = 1, 2 or 3). They are derived from parent MAX phases, which are ternary layered materials with a hexagonal crystal structure (P63/mmc) which have been widely studied.[68] The name MAX phase comes from the chemical composition of the materials, with M corresponding to early transition metals (Sc, Ti, V, Cr, Y, Zr, Nb, Mo, Hf, Ta and W), A corresponding to elements from the columns 12-16 of the periodic table (Al, Si, P, S, Ga, Ge, As, Cd, In, Sn, TI and Pb), and X corresponding to C and/or N. The crystal structure and chemical composition of MAX phases are summarized in Figure 2.5. So far, more than 70 MAX phases have been reported experimentally, and even more MAX phases being predicted from computer simulation.[59] Only a few MXenes have been able to be synthesized from these MAX phases, but the numbers are growing alongside a better understanding of these materials and the development of new synthesis routes. The variety of available chemistries has made MXenes very interesting, as the properties have the potential de be tuned by modifying the chemistry of the MXenes. And in addition to that, there is a possibility to have elements mixed in ordered or solid-solution manners in the different layers, such as X being potentially a mix of C and N, for instance in Ti_3CN,[69] or M being and a mix of Mo and Ti in Mo_2TiC_2.[70-73] A list of the MXenes that have been experimentally synthesized is reported in Table 2.3, with the parent materials they have been synthesized from.
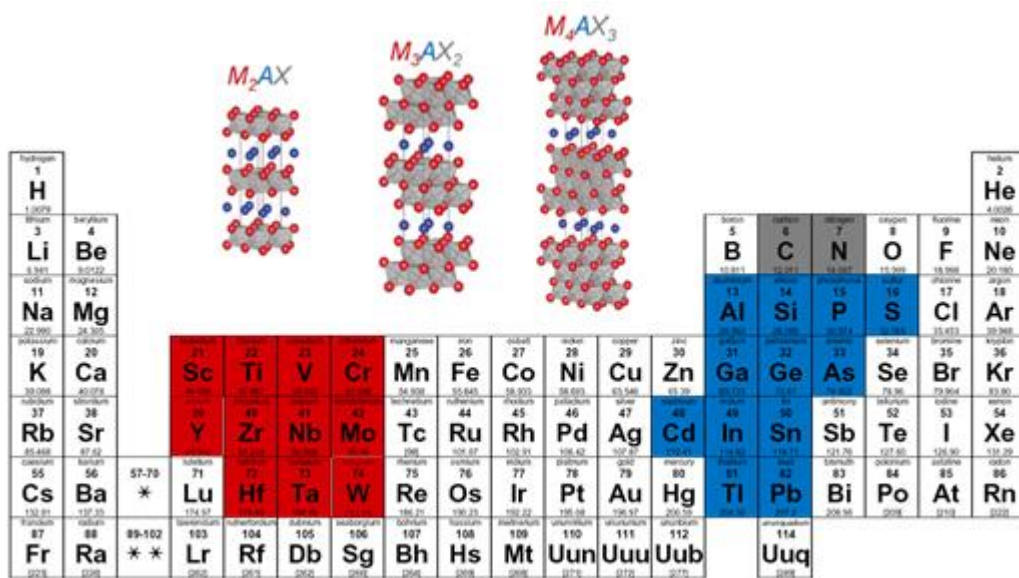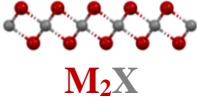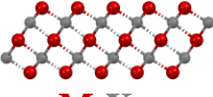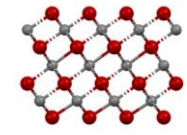
Figure 2.5: Cristal structure and elements of MAX phases. The M-elements are represented in red, the A-elements in blue and the C and/or N in grey. Adapted from ref [74,75]

As most 2D materials, a lot of their properties and applications are related to their surface chemistry, it is also important to consider the different surface groups that are present on a given materials. In the case of MXenes, depending on the synthesis methods, which will be discussed in the next part, the surface groups can be a mix of -OH, -O, -F and -Cl. These surface groups are more or less stable depending on the environment in which the MXene is or the temperature, and they will influence the properties of the MXenes.

Type	MXene	MAX phase	Etching method	Ref
M_2X	Ti_2CT_x	Ti_2AlC	HF	[76]
			HCl + LiF	[77]
			HCl + F salts	[78]
			$ZnCl_2$	[79]
	Ti_2NT_x	Ti_2AlN	HCl + KF	[80]
	Nb_2CT_x	Nb_2AlC	HF	[81]
	Mo_2CT_x	Mo_2Ga_2C [a]	HF, HCl + LiF	[82]
	Mo_2NT_x (nitration)	Mo_2Ga_2C [a]	HF	[83]
	V_2CT_x	V_2AlCT_x	HF	[81]
	V_2NT_x (nitration)	V_2AlCT_x	HF	[83]
	$(Ti_{0.5},Nb_{0.5})_2CT_x$	$(Ti_{0.5},Nb_{0.5})_2AlC$	HF	[76]
	$(Ti_{0.5},V_{0.5})_2CT_x$	$(Ti_{0.5},V_{0.5})_2AlC$	HF	[84]
	$(Mo_{2/3}Y_{1/3})_2CT_x$	$(Mo_{2/3}Y_{1/3})_2AlC$	HF	[85]
	$Mo_{1.33}CT_x$ [b]	$(Mo_{2/3}Sc_{1/3})_2AlC$	HF, HCl + LiF	[86]
		$(Mo_{2/3}Y_{1/3})_2AlC$	HF	[85]
	$W_{1.33}CT_x$ [b]	$(W_{2/3}Sc_{1/3})_2AlC$	HF, HCl + LiF	[87]
		$(W_{2/3}Y_{1/3})_2AlC$		
	$Nb_{1.33}CT_x$ [b]	$(Nb_{2/3}Sc_{1/3})_2AlC$	HF	[88]
M_3X_2	$Ti_3C_2T_x$	Ti_3AlC_2	HF	[58]
			HCl + LiF	[77]
			HCl + F salts	[78]
			$ZnCl_2$	[79]
			NH_4HF_2	[89]
			Hydrothermal NaOH	[90]
		Ti_3SiC_2	HF + H_2O_2	[91]
	Ti_3CNT_x	Ti_3AlCN	HF	[76]
	$Zr_3C_2T_x$	$Zr_3Al_3C_5$ [a]	HF	[92]
	$Hf_3C_2T_x$	$Hf_3(Al,Si)_4C_6$ [a]	HF	[93]
	$(Mo_{2/3}Ti_{1/3})_3C_2T_x$	$(Mo_{2/3}Ti_{1/3})_3AlC_2$	HF	[73]
	$(Mo_{2/3}Sc_{1/3})_3C_2T_x$	$(Mo_{2/3}Sc_{1/3})_3AlC_2$	HF	[94]
	$(Cr_{2/3}Ti_{1/3})_3C_2T_x$	$(Cr_{2/3}Ti_{1/3})_3AlC_2$	HCl + LiF	[73]
	$(Cr_{1/2}Ti_{1/2})_3C_2T_x$	$(Cr_{1/2}Ti_{1/2})_3AlC_2$	HF	[76]
	$(Ti_{1/2}V_{1/2})_3C_2T_x$	$(Ti_{1/2}V_{1/2})_3AlC_2$	HF	[84]
M_4X_3	$Ti_4N_3T_x$	Ti_4AlN_3	Molten salts (LiF, NaF, KF)	[95]
	$Nb_4C_3T_x$	Nb_4AlC_3	HF	[96]
	$V_4C_3T_x$	V_4AlC_3	HF	[97]
	$Ta_4C_3T_x$	Ta_4AlC_3	HF	[76]
	$Mo_2Ti_2C_3T_x$	$Mo_2Ti_2AlC_3$		[73]
	$(Nb_{0.8},Ti_{0.2})_4C_3T_x$	$(Nb_{0.8},Ti_{0.2})_4AlC_3$	HF	[98]
	$(Nb_{0.8},Zr_{0.2})_4C_3T_x$	$(Nb_{0.8},Zr_{0.2})_4AlC_3$	HCl + LiF	[98]

[a] Non MAX phase precursor

[b] $M_{1.33}X$ from selective etching of M-layer elements in $(M,M')_2AX$ forming atom vacancies

2.4.2. MXenes synthesis and processing

The most common approach to synthesize MXenes is through selective etching of the parent MAX phase, except for some MXenes which were synthesized using other parent materials as shown in

Table 2.3, resulting in a multi-layered MXene with the presence of surfaces groups labelled $M_{n+1}X_nT_x$ (where x can be -O, -OH, -F in most cases). The M-A bonds are chemically active, while the M-X bonds are more stable chemically, allowing the selective etching of the A-element layer. A schematic of the selective etching is shown on Figure 2.6. Several etching methods have been developed and are appropriate' in some cases, to very specific MXene synthesis. Moreover, the etching methods used lead to different MXenes properties after etching, such as flake size, numbers of layers, presence of defects, surface groups… The different etching methods for the different MXenes synthesized so far have been summarized in Table 2.3, and are now going to be discussed further.
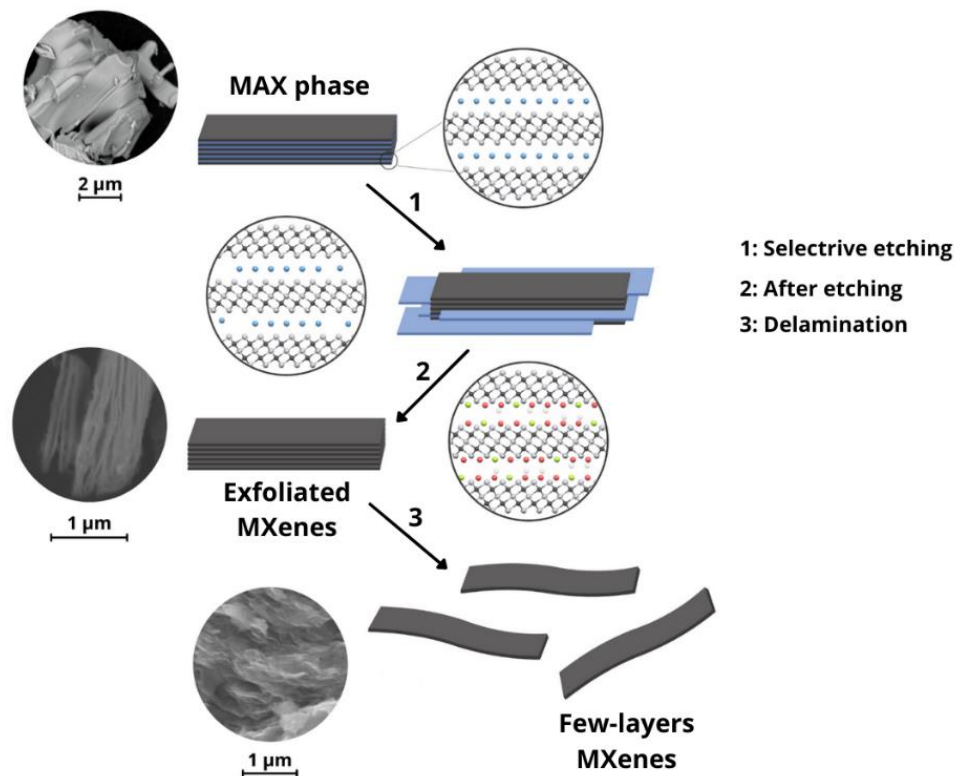
Figure 2.6: Schematic showing the etching process of MXenes with SEM pictures of the different steps (SEM pictures of Ti3AlC2 MAX phase and Ti3C2 MXenes)

2.4.2.1. HF etching method

The first instance of MXene synthesis was done using this method by researchers from Drexel University in 2011. The A-element layer was selectively etched and a 2D material was synthesized with an accordion-like structure (see Figure 2.7). The protocol followed for the first

MXene synthesis is as follow and was done to synthesize Ti_3C_2 from the Ti_3AlC_2 parent MAX phase. Ti_3AlC_2 was added to a 50% hydrofluoric acid (HF) solution at room temperature for 2h.[58] The solution is then washed and centrifuged with deionized water several times before collecting the powder. Filtration of the solution after the washing steps can also be done, as well as freeze drying, which would lead to different porosity and surface area properties.

The etching reaction of $M_{n+1}AlX_n$ using HF is presumed to be following the reaction steps described below (other MAX phases that can be etched to MXenes using HF are etched through a similar set of reaction steps):[58,76]

$$M_{n+1}AlX_n + 3HF = AlF_3 + M_{n+1}X_n + 1.5H_2 \qquad \text{Eq. 2.5}$$

$$M_{n+1}X_n + 2H_2O = M_{n+1}X_n(OH)_2 + H_2 \qquad \text{Eq. 2.6}$$

$$M_{n+1}X_n + 2HF = M_{n+1}X_nF_2 + H_2 \qquad \text{Eq. 2.7}$$
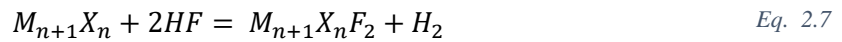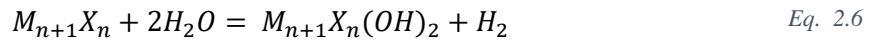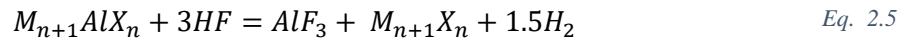
The reaction described in Eq. 2.5 shows the selective removal of Al (A-element layer) by the F^- ions, leading to the synthesis of the bare MXene. It shows that the fluorine ions are the active species which react with the A-element layer to form salts as a biproduct in addition to the MXenes. The reactions showed in Eq. 2.6 and Eq. 2.7 correspond to the reaction of the bare MXene surface with its environment, leading to the formation of -OH and -F surface groups.
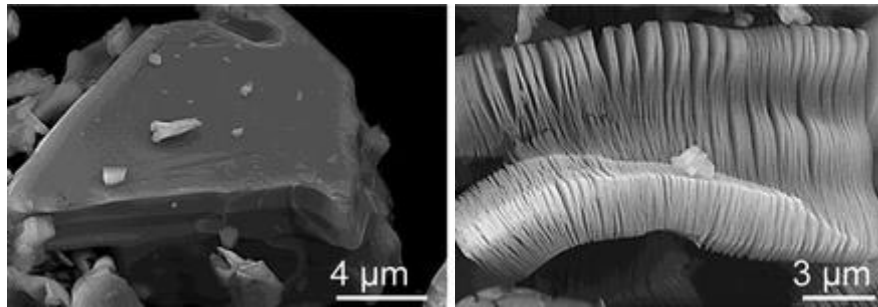
Figure 2.7:SEM pictures of Ti3AlC2 MAX phase (left) and Ti3C2 after HF treatment (right)[76]

The etching conditions for the different MXenes synthesis vary a lot depending on the precursor materials, as the energies of the different M-A bonds varies when different elements are considered.

Another thing to consider when synthesizing MXenes is the n-value (1, 2 or 3) of $M_{n+1}X_n$. Indeed, higher n-value MAX phases are generally more stable. The higher the n-value is, the higher the HF concentration and/or time and/or temperature are going to be required. For instance, in a study done by Naguib & al., Ti_2C has been synthesized using 10 wt% HF at RT for 10 hours, while Ti_3AlC_2 required 50% HF at RT for 2 hours.[76]

As Ti_3C_2 is the most widely studied MXene, the synthesis and processing conditions are a bit more understood than for other MXenes. M. Alhabeb et al. studied the synthesis and processing

of Ti_3C_2 using different conditions.[99] Ti_3C_2 was synthesized successfully using HF solutions ranging from 5, 10 and 30 wt%, but the lower the concentration was, the longer the etching time required was, respectively 24, 18 and 5 hours. Moreover, the MXene morphology varied depending on the HF concentration used, and the open accordion-like morphology was more prevalent at higher concentration, while the layers are just slightly open with lower concentrations. This was ascribed to the presence of a larger amount of H_2 formed during the etching, leading to a more open structure.

2.4.2.2. HCl + F-salt etching method

Although HF seems to be a method that works in the synthesis of a lot of MXenes and leads to good yields during the synthesis, the main drawback of this method is its highly hazardous nature. HF is already a highly toxic chemical that requires a lot of precautions to be used, even at low concentrations, but as seen previously, the HF concentration required for MXene synthesis are usually around 40-50 wt%. The need to synthesize MXenes in a safer environment has led to the development of other methods, such as the HCl + F-salt etching. This method is a lot safer than the etching using HF solutions. Despite the fact that some HF is formed in situ during the etching process, no direct manipulation of HF is required and most of the fluorine should be used by the end of the synthesis.

2.4.2.3. Other methods

Other etching methods for MXenes have been developed but are usually quite specific to certain MAX phases and have not been able to be widely used to synthesize other MXenes. These other methods are out of the scope of this thesis, and therefore, are not described. The MXenes which have been synthesized using other etching methods and the references to the work related are given in Table 2.3.

2.4.3. MXene-based materials for Oxygen Reduction Reaction

Due to the variety of chemistries available and their 2D morphology, combined with their good electrical properties and hydrophilic nature, a lot of attention have been given to MXenes for electrochemical and catalytic applications. MXenes have been mainly studied as materials for applications such as batteries and supercapacitors, but to a lesser extent, MXenes have also been of interest for catalytic applications, such as HOR, HER and ORR.

2.4.3.1. MXenes as catalysts for ORR

As mentioned earlier, the adsorption strength of O-containing intermediates during ORR is an important factor influencing the electrocatalyst activity. Therefore, the chemical environment at the electrocatalyst-electrolyte interface, and especially the different surface groups available are going to be of paramount importance. In the case of MXenes, the different hydrophilic surface groups, mainly -O/-OH/-F, are going to determine the adsorption capabilities of O-containing intermediates. Some theoretical studies have been undergone to evaluate the ORR properties of MXene-based compound depending on the surface groups available. Particularly, Liu et al. have investigated theoretically the influence of -O and -F surface groups on the ORR performance of $Ti_{n+1}C_nT_2$ towards ORR.[100] They have found that -F surface terminations would display higher ORR activity compared to -O, but would not be as stable due to weaker chemical bonding to the surface.

Experimentally, Lin et al. have evaluated the ORR performance of multi-layer and single-layer $Ti_3C_2T_x$ in 0.1M KOH. No particular emphasis on the chemistry of the surface groups has been studied but based on the etching method used (HF) and the XPS spectra of the MXenes, the surface is most likely -F rich. The aim of the study was to compare the ORR activity of stacked and delaminated $Ti_3C_2T_x$ and they found that SL-$Ti_3C_2T_x$ exhibited better ORR activity than ML-$Ti_3C_2T_x$, with an onset potential around 0.85 V (vs RHE) and an apparent electron transfer number of 3.7, while showing reasonable stability after 1000 ADT (Accelerated Durability Test).[101] However, ORR performance of $Ti_3C_2T_x$, even delaminated, is still far from the Pt/C benchmark. Therefore, more emphasis has been put towards the use of MXenes as support materials or as co-catalyst.

2.4.3.2. Noble metals supported on MXenes for ORR

Platinum:

Being the best catalyst for ORR applications, Pt has been the first material which has been deposited on Ti_3C_2 and tested. Pt nanoparticles supported on Ti_3C_2 were found to have a similar activity compared to Pt/C in $HClO_4$ electrolyte and ended up being more durable during ADT. The better resistance of Pt/Ti_3C_2 to degradation was found to be due to the MXene layer preventing Pt nanoparticles aggregation and loss during testing.[102] Moreover, Ti_3C_2 has shown to enhance the Pt activity through a stronger metal-support interaction on Ti_3C_2 compared to carbon, which would allow for better electron transfer. Later on, Zhang et al. have investigated Pt/Ti_3C_2 for ORR in both acidic (H_2SO_4) and alkaline (KOH) media, and was found to follow a quasi-four-electron process in alkaline medium, while being a mixed 2 and 4-electron process in acidic

conditions.[103] Moreover, the Pt/Ti$_3$C$_2$ has shown better stability than Pt/C in both acidic and alkaline media after ADT, demonstrating a shift in E$_{1/2}$ of 49 mV compared to 80 mV for Pt/C in H$_2$SO$_4$, and a shift of 21 mV while Pt/C had a 30 mV shift in KOH (Figure 2.8). Structural characterization has shown similar trend compared to the first study concerning the reason of the improved durability, which is less Pt particles aggregation and the prevention of high oxidative corrosion to the catalytic sites. It was also suggested that the n value might be dependent on the number of layers of the MXene stacks, as many Pt particles are stuck in the middle of the layers and could lead to intermediate products being trapped by the MXene layer surfaces. Indeed, MXenes layers are prone to restacking even when they have been delaminated, which can lead to problems in term of active sites access for the reactants. Moreover, MXenes display low specific surface area of around 3-10 m².g^{-1} after synthesis and ~20 m².g^{-1} after delamination, which is very low for a support when it comes to electrocatalytic applications. Some researchers have made use of additional materials to prevent the re-stacking of the MXene layers, as well as increasing SSA. In the case of Pt-based catalysts, MXene-CNT hybrid supports have been investigated and have shown better ORR performance than with solely using MXenes. The CNT allows to keep the MXenes layers apart, while improving ECSA of the final electrocatalyst, and also boost the mass and charge transfer during the ORR process. Xu et al. have shown that Ti$_3$C$_2$ provides a stronger interactions with Pt than a carbon support would, leading to greater ORR activity.[104] Indeed, their Pt/CNT-Ti$_3$C$_2$T$_x$ sample exhibits a Pt 4f$_{5/2}$ binding energy shifted by 0.21 eV to higher value compared to Pt/C, indicating stronger interaction and was owed to the -OH and -F surface groups of the MXenes which act as anchor points to facilitate the dispersion and the binding of Pt nanoparticles. The mass and specific activity of Pt/CNT-Ti$_3$C$_2$T$_x$ ended up being 3.4 and 2.5 times higher than Pt/C in acidic medium. The CNT addition, in addition to the previous advantages, was also thought to improve O atoms desorption compared to Ti$_3$C$_2$ alone, as well as increase catalytic stability. Other morphologies of electrocatalyst have been tested too. For instance, Wang et al. have developed Pt-NWs/Ti$_3$C$_2$T$_x$-CNT for HT-PEMFC applications, which displayed better activity towards ORR compared to both Pt/C and Pt-NPs/Ti$_3$C$_2$T$_x$-CNT.[105] XPS analysis of the material put in light the shift in Pt 4f binding energy, as well as a higher content of metallic Pt^0 compared to Pt/C and was thought to be the reason for the better catalytic stability and higher activity.
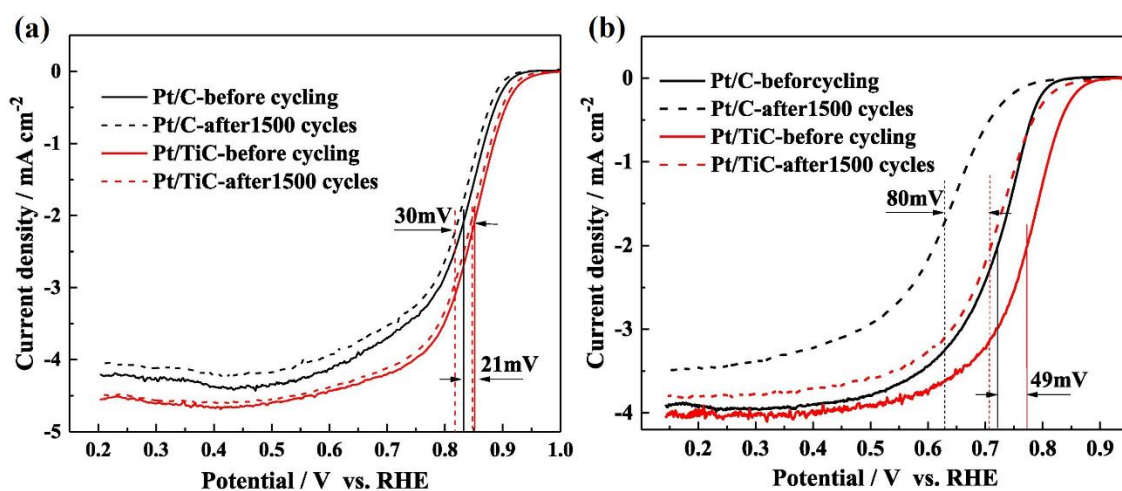
Figure 2.8: LSV curves of Pt/C and Pt/Ti₃C₂ at 1600 rpm in O₂-saturated (a) 0.1M KOH and (b) 0.5 M H₂SO₄ before and after ADT [103]

Several theoretical/DFT analysis have been performed to see how the MXenes influences the electronic properties and the overall ORR performance of the active sites when decorated with electrocatalytically active species. For example, Liu et al. have also predicted that -F surface groups were improving ORR activity for $Pt/v-Ti_{n+1}C_nT_2$, following the same trend than $Ti_{n+1}C_nT_x$ discussed earlier.[100] Xu et al. have compared the adsorption and dissociation energies of O_2, as well as the O binding energy on Pt, on $Ti_3C_2T_x$ and CNT-modified $Ti_3C_2T_x$ support in acidic solution through first principle simulations.[104] They found that the calculated dissociation energies for the Pt supported on both MXene supports were smaller compared to Pt(111) surface, which suggest a better ORR activity. Moreover, the Pt/CNT-MXene displayed a lower O binding energy compared to Pt/MXene, which would explain the better ORR performance of the CNT-modified MXene support compared to simply using MXene.

More recently, Lee et al. have investigated the influence of the number of layers in the Ti_3C_2 MXene structure on the metal-support interaction between deposited Pt and Ti_3C_2 and the ORR activity in 0.1 M $HClO_4$ of the resulting catalyst material.[106] To do so, they prepared MXenes using different etching protocols to obtain Ti_3C_2-22L, Ti_3C_2-4L and Ti_3C_2-1L containing in average 22, 4 and 1 layers MXenes respectively, and Pt was then deposited on the MXene supports. The amount of edge Pt nanoparticles throughout the different samples were as follow: Ti_3C_2-22L > Ti_3C_2-4L > Ti_3C_2-1L. Structural characterization of the different Pt-deposited samples has shown that there is a stronger metal-support interaction for Pt/22L and was explained by a greater number of Pt-edge particles for this sample due to the defective nature of the edge structure allowing for stronger interactions compared to basal plane Pt deposition. Pt was found to be more electron-rich when it was placed on edge planes compared to basal planes and was supported by the negative shift of the Pt 4f XPS peak with increasing number of Ti_3C_2 layers. Based on DFT calculation, they have anticipated that the *OH desorption energy for edge Pt was lower than for basal Pt, which would lead to better ORR properties. This was confirmed from

experimental ORR characterization, where the activity of the samples was increasing with the amount of edge Pt, while the overpotential decreased.

Non-platinum:

In the case of alkaline media, for AFC and metal-air batteries, a broader range of metallic catalysts is available for ORR. Some other precious metals have been investigated as electrocatalysts supported by Ti_3C_2 in KOH electrolyte. Zhang et al. have investigated the properties of Pd supported on a $Ti_3C_2T_x$-CNT hybrid.[107] The CNT allowed for a better charge transfer and was used to sterically impede the restacking of MXene layers. They found that the Pd/$Ti_3C_2T_x$-CNT mass and specific activities were 4.4 and 3.3 times higher than for Pd/C towards ORR. Similar to Pt-decorated MXenes, they found that the XPS spectra of the metal catalysts nanoparticles (Pd 3d) had shifted to higher binding energy by 0.1 eV compared to carbon support, showing a stronger metal-support interaction between Pd and $Ti_3C_2T_x$. The Pd on MXene-CNT hybrid displayed overall better ORR performance.

A summary of the different materials using MXenes as support materials for precious metal catalysts has been gathered in Table 2.4 and their main ORR electrochemical properties have been listed as well.

Table 2.4: Reported ORR noble metals electrocatalysts using $Ti_3C_2T_x$ as support

Catalysts	Electrolyte	E_{onset} (V vs RHE)	$E_{1/2}$ (V vs RHE)	Performance	Ref
Pt/$Ti_3C_2T_x$	0.1 M $HClO_4$	-	0.847	-	[102]
Pt/$Ti_3C_2T_x$	0.5 M H_2SO_4 0.1 M KOH	- 0.95	0.772 0.853	-	[103]
PtNWs/$Ti_3C_2T_x$-CNT	0.1 M $HClO_4$	1.02	0.896	-	[105]
Pt/CNT-$Ti_3C_2T_x$	0.1 M $HClO_4$	-	0.876	ECSA drop of 6% after 2000 ADT cycles compared to 27% for Pt/C	[104]
Pt/$Ti_3C_2T_x$ 1L Pt/$Ti_3C_2T_x$ 4L Pt/$Ti_3C_2T_x$ 22L	0.1 M $HClO_4$	-	-	i_k (0.9 V vs RHE): 18 $\mu A.cm_{Pt}^{-2}$ 75 $\mu A.cm_{Pt}^{-2}$ 99 $\mu A.cm_{Pt}^{-2}$	[106]
Pd/$Ti_3C_2T_x$-CNT	0.1 M KOH	1.085	0.925	-	[107]
Ru-SA/$Ti_3C_2T_x$	0.1 M $HClO_4$	0.92	0.80	-	[108]
$Ti_3C_2T_x$ /NW-$Ag_{0.9}Ti_{0.1}$	0.1 M KOH	0.921	0.782	-	[109]

2.4.3.3. MXenes with non-(noble metals) as catalysts towards ORR

MXenes have shown good prospects as support for precious metal based electrocatalysts particles or single atoms towards ORR, as well as for other electrochemical processes as mentioned earlier. But precious metal based electrocatalysts, and especially Pt, are expensive and are an impediment to the further development of fuel cells in the industry. In the case of AFCs, AEMFCs and metal-air batteries, operating in alkaline environment, other electrocatalysts are available to be used due to greater chemical and electrochemical stabilities, as well as improved ORR mechanisms, in alkaline medium compared to acidic medium.

When it comes to non-PGM catalysts for ORR, M-N-C (M = Fe, Co) materials are very good candidates, which in certain cases have shown to have activity towards ORR close to that of platinum catalysts. The performance of M-N-C catalysts is directly linked to the quantity of nitrogen atoms that form coordination bonds with the transition metal centre. It has been observed that the M-N_4 configuration represents the most favourable arrangement, resulting in optimal ORR activity. It is therefore not surprising to see several studies attempting to couple MXene materials with M-N-C structures. Li et al. have specifically designed a catalyst to study the interaction between Fe-N_4 moieties and $Ti_3C_2T_x$ MXene.[110] FePc (iron phtalocyanine) was mixed with the MXene in a solution of dimethylformamide, followed by ultrasonication, centrifugation and drying. The resulting composite, known as the FePc/$Ti_3C_2T_x$, was then evaluated for its ORR activity. The incorporation of Fe-N_4 into $Ti_3C_2T_x$ resulted in a reduction of the work function of the Fe centres, which, in turn, contributed to an enhanced ORR activity. This improvement was confirmed through the observed shift in the Fe 2p X-ray Photoelectron Spectroscopy (XPS) peak toward higher binding energies.

Other studies have looked into coupling MXenes with Co MOF-based compounds, followed by pyrolysis to form Co-CNT forming on top of MXene particles.[111] Wang et al. produced a catalyst, Fe-N-C@$Ti_3C_2T_x$, which was synthesized as follow. In this synthesis, the Fe-N-C catalyst was first pre-synthesized from ZIF-8 and then subjected to pyrolysis at 1100°C. This resulting material was then combined with $Ti_3C_2T_x$ and further treated at a lower temperature (350°C). The layered structure of $Ti_3C_2T_x$ served as a substrate, effectively preventing the aggregation of Fe-N-C and enhancing the overall stability of the catalyst. XRD analysis of the Fe-N-C@$Ti_3C_2T_x$ catalyst revealed no indications of structural changes, confirming the well-preserved layered structure of MXene.[112]

Overall, the presence of the MXene improved the electrocatalytic performance of the catalyst. This was explained in most cases, by a strong MXene support interaction, which modified the electronic structure of the deposited catalyst, and lead to an increased activity towards ORR. Other factors included a better dispersion of the deposited catalysts over the MXene and a greater stability.

The different MXenes-based electrocatalysts investigated towards ORR from the literature have been summarized in Table 2.5, as well as their principal electrochemical properties.

Table 2.5: Reported ORR non precious-metal electrocatalysts using $Ti_3C_2T_x$ as support

Catalysts	Electrolyte	E_{onset} (V vs RHE)	$E_{1/2}$ (V vs RHE)	Ref
Co-CNT/ $Ti_3C_2T_x$	0.1 M KOH	-	0.82	[113]
Co/CNTs@ $Ti_3C_2T_x$	0.1M KOH	0.936	0.815	[111]
FePc/$Ti_3C_2T_x$	0.1 M KOH	0.97	0.89	[110]
FeNC/$Ti_3C_2T_x$	0.1 M KOH	1.00	0.814	[114]
Fe-N-C/$Ti_3C_2T_x$	0.1 M KOH	0.92	0.84	[115]
Fe-N-C/$Ti_3C_2T_x$	0.1 M KOH / 0.1 M $HClO_4$	- / -	0.887 / 0.777	[112]
FeCo-N-$Ti_3C_2T_x$	0.1 M KOH	0.96	0.80	[116]
Co_3O_4/NCNTs/$Ti_3C_2T_x$	0.1 M KOH	-	0.79	[117]
Mn_3O_4/$Ti_3C_2T_x$	0.1 M KOH	0.89	-	[118]
$NiCo_2O_4$/$Ti_3C_2T_x$	1 M KOH	-	0.7	[119]
MoS_2QDs @Ti_3C_2QDs @MWCNTs	1 M KOH	0.87	0.75	[120]
CoS_2@$Ti_3C_2T_x$	0.1 M KOH	0.87	0.80	[121]
$Ti_3C_2T_x$@PPy	0.1 M KOH	0.85	0.71	[122]
g-C_3N_4/$Ti_3C_2T_x$	0.1 M KOH	0.92	0.79	[123]

2.5. Aims and objectives

As discussed earlier, one of the main issues slowing down the commercialisation of fuel cells is their price. Indeed, the catalysts used in commercial fuel cells are platinum-based materials and other noble metals. It is therefore interesting to work with AFCs, which run in KOH electrolytes. Alkaline media provides better ORR kinetics and allows the use of a wider range of cheaper catalysts. A new family of materials, MXene, which are a family of two-dimensional transition metal carbides and nitrides, has shown some interesting electrochemical properties. They have shown to be good supports for platinum catalysts for oxygen reduction reaction applications, with greater stability than commercial Pt/C. This has pushed researchers to study MXenes for ORR applications, using different catalysts and methods. However, one of MXenes' main drawback are their small specific surface areas compared to usual catalysts supports. Moreover, the majority

of work done so far on non-PGM MXene compounds for ORR are basing their synthesis on usual non-PGM synthesis processes, such as MOF, in which they add a small amount of MXenes. No specific focus is given to intercalate the MXenes to avoid the restacking of the MXene flakes during the synthesis of the final catalyst. Thus, it would be interesting to focus on avoiding the restacking of MXenes, by intercalating compounds which would act both as "pillars" and as ORR co-catalysts. With this method, the objective is to increase the surface area, as well as the intrinsic ORR activity, of the MXene-based materials, which would lead to an overall increase in catalytic performance of the synthesized materials.

Therefore, the aim of this thesis is:

To synthesis an MXene-based structure, while focusing on intercalating the MXene to avoid the retacking of the MXene layers, while increasing the overall specific surface area and the activity towards ORR of the materials.

Therefore, the following objectives have been set:

- Designing a synthesis method for MXene-based materials using intercalated precursors to create a porous and stable structure.
- Characterizing the physico-chemical properties of these MXene-based materials and understanding the influence of different synthesis conditions on the materials properties.
- Characterizing the electrochemical properties of the synthesized materials, and their performance toward ORR and their electrochemical stability.

CHAPTER 3: Materials and methods

This chapter describes the materials and the methods used to carry out the synthesis and characterization reported in this thesis. The materials synthesis protocols to make the MXenes and the different composite materials are detailed. Additionally, the basics of the different physicochemical characterization techniques used, such as x-ray diffraction (XRD), scanning electron microscopy (SEM), energy dispersive x-ray spectroscopy (EDS), Raman spectroscopy, X-ray photoelectron spectroscopy (XPS), BET analysis and ^{57}Fe Mössbauer spectroscopy, are introduced. Finally, the equipment and methods used to carry the electrochemical characterization of the synthesized materials are going to be described for the rotating ring disk electrode (RRDE) 3-electrode setup, such as cyclic voltammetry (CV), linear sweep voltammetry (LSV) and the different analysis methods related to these measurements.

3.1. Materials synthesis
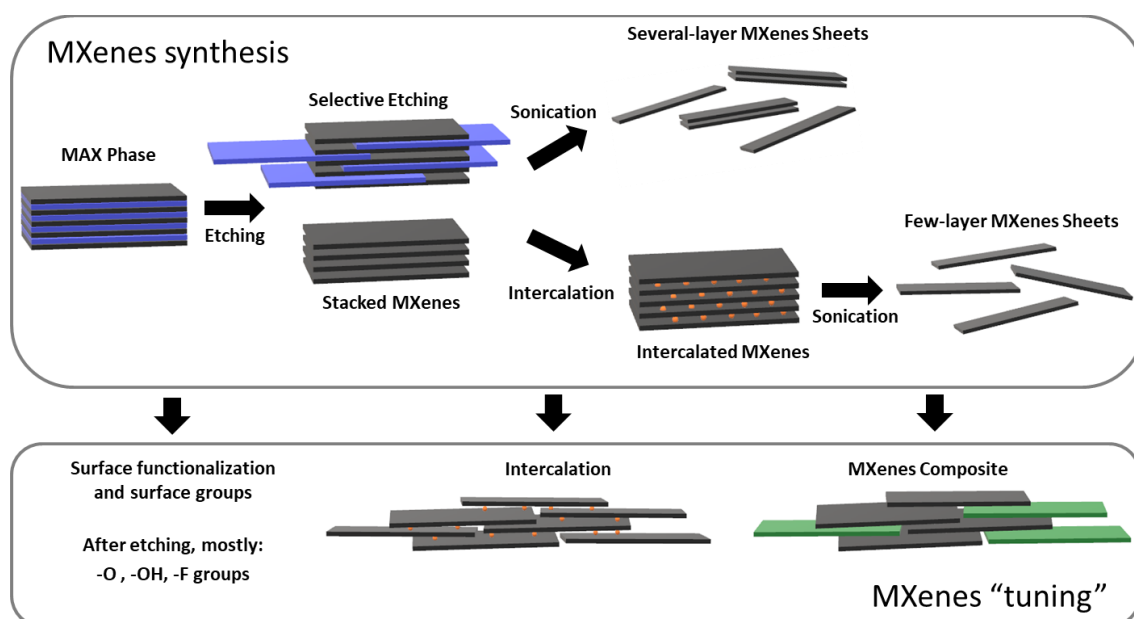
Figure 3.1: Schematic of the different steps usually involved in the synthesis and tuning of MXenes materials

Figure 3.1 presents a quick overview of the different steps that are usually involved during the synthesis of the MXenes, as well as the tuning and functionalisation of the synthesized MXenes. As described previously in the background chapter, MXenes are a family of layered materials with a wide range of chemistries, which can be intercalated more or less easily with other compounds, mostly cations, within its layer structure. In this thesis, due to the etching

requirements and conditions for the different MAX phases (see 2.4.2 MXenes synthesis and processing) and safety considerations, Ti_3AlC_2 MAX phase and its corresponding MXene, $Ti_3C_2T_x$, have been chosen to be the starting materials for this research.

The synthesis of the samples started with the etching of Ti_3AlC_2 into $Ti_3C_2T_x$, which will be described in the next part. Unless stated otherwise, the MXene synthesis do not include the sonication steps, and were kept as multi-layer "accordion-like" MXenes prior to their functionalization. Once synthesized, the MXenes underwent further treatments, which will also be described in this chapter.

3.1.1. Synthesis of $Ti_3C_2T_x$

The etching procedure used in this thesis to produce $Ti_3C_2T_x$ is the LiF-HCl etching method, adapted from the one first reported by Ghidiu et al.,[77] due to this method being significantly less hazardous than the conventional HF method (refer to the Background chapter for more details on etching methods).
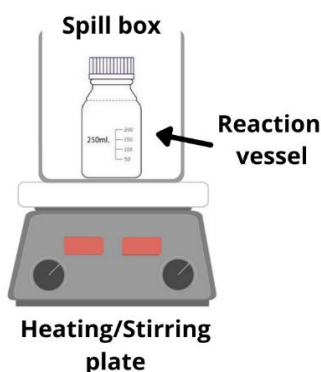
Figure 3.2: Schematic representation of the set-up for MXene synthesis

The Ti_3AlC_2 MAX phase (>85% purity) was bought from Carbon-Ukraine Ltd. (Kyiv, Ukraine), was ground, and sieved through a -400 mesh sieve to obtain particle sizes below 38 µm. Sieving the MAX phase has shown to provide more homogenous etching conditions with less left-over Ti_3AlC_2 or over-etched species. Once ground, the Ti_3AlC_2 powder was etched using the HCl + LiF method. Typically, 3 g of LiF (99%, Alfa Aesar) was added to 30 mL of 6 M HCl (37.5% wt., Sigma Aldrich) in a HF resistance reaction vessel, then, once the salt was dissolved, 3 g of Ti_3AlC_2 was slowly added to the solution to avoid overheating due to the exothermic nature of the reaction. The reaction vessel was then securely closed with a lid. It has to be noted that the lid had a small hole to allow venting of the H_2 forming during the etching of the MXene. The mixture was then left to stir at 40 °C for 48 h using the set-up shown in Figure 3.2. After the etching, the

sample was rinsed several times using DI water with a centrifugation step at 2000 rpm and at room temperature for 5 min between rinses. This rinsing procedure was repeated until the pH of the supernatant was above pH 6. The sample was then left to dry overnight at around 70 °C in a drying oven.

3.1.2. Synthesis of Ti₃C₂-U-x samples

As synthesized Ti_3C_2 was dispersed in DI water. Urea (>99%, Alfa Aesar) was then added to the solution at a Ti_3C_2 to urea weight ratio of 1:1, 1:10 and 1:50 for Ti_3C_2-U1, Ti_3C_2-U10 and Ti_3C_2-U50, respectively. The solution was left to stir for 15 h at 55 °C. After evaporation of the solution, the materials were then ground with a pestle and mortar and then transferred into an alumina crucible. The samples were then heated up to 550 °C at a rate of 5 °C/min for 3 h in a tube furnace under argon atmosphere to obtain Ti_3C_2-U-550 samples. The crucible was covered with an alumina cover to reduce material losses during the decomposition of the urea while still being able to purge the air out of the working tube before the thermal treatment using the argon flow. As a reference, a Ti_3C_2 sample was treated following the same thermal treatment without urea.

To obtain the Ti_3C_2-U-800 samples, the same procedure was followed except for the last thermal treatment, which consisted in this case of a two steps thermal treatment. The tube was first heated up to 550 °C at 5 °C/min for 3 h, then heated up to 800 °C still under argon at 5 °C/min for 1 h before being cooled down to room temperature. A schematic of thermal treatment for the different samples is given in Figure 3.3 for clarity.
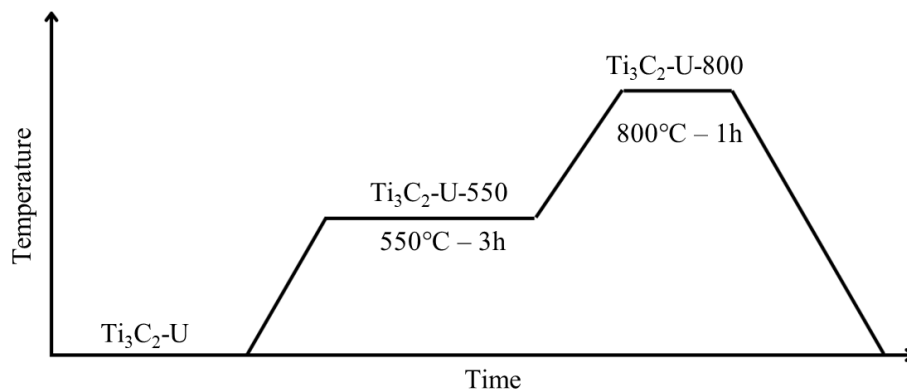
Figure 3.3: Schematic describing the thermal treatment procedure used to synthesize the different urea-treated samples

3.1.3. Synthesis of g-C₃N₄

g-C$_3$N$_4$ was synthesized as a reference sample following a known synthesis route from the literature.[124,125] Typically, 10 g of urea was loaded in a covered alumina crucible and heated up to 550 °C at a rate of 5 °C/min for 3 h in a tube furnace under argon atmosphere. The powder obtained was yellowish in colour.

3.1.4. Synthesis of Ti₃C₂-U-Fe-800 and C-U-Fe-800 samples

The synthesis of Ti$_3$C$_2$-U-Fe-800 samples was done following a similar procedure compared to the previous ones. The MXene is first mixed with urea in DI water at different weight ratios (1:10 and 1:50). FeCl$_3$.6H$_2$O (>99%, Sigma Aaldrich) was then added to the solution at a 1:1 weight ratio compared to MXene. The solution is then stirred at 55 °C for 15 h, and dried. Afterwards the mixture was ground and transferred into an alumina crucible and thermally treated using the same two-step treatment as described for Ti$_3$C$_2$-U-800 samples. Figure 3.3 shows the schematic of the procedures for the different samples.

3.2. Characterization methods

3.2.1. Physicochemical characterization

3.2.1.1. X-ray powder diffraction (XRD)

XRD is a widely used non-destructive technique, allowing to characterize the structure of solid crystalline materials. It is primarily used for phase identification and provide information on unit cell dimensions. XRD takes advantage of the fact that the ordered structure of a crystal lattice has inter-planes spacing which is of a similar magnitude than X-ray wavelength (~1Å) and can therefore diffract incident X-rays. When X-rays reach crystal planes, they either interact with electrons of atoms constituting that plane or continue to the next plane. These planes are separated from each other by a distance characteristic of the orientation and the studied materials. The interferences between the different scattered X-rays are alternatively constructive or destructive. The orientations for which the interferences are constructive, corresponding to diffraction peaks, are represented by Bragg's law:

$$n\lambda = 2dsin\theta$$

n, order of diffracted X-ray

λ, wavelength of the X-ray

d, interplanar distance

θ, angle of incidence

X-ray diffraction principle is illustrated in Figure 3.4, where the incident x-rays, with a fixed wavelength using a monochromatic x-ray source, are scattered by the crystal and then measured by a detector. Whenever the Bragg's law is satisfied at a specific incidence angle, the constructive interferences lead to an observable peak in the diffraction pattern. X-ray diffraction patterns are usually plotted as the intensity of the detected X-rays against the angle 2θ and are measured over a wide 2 X-ray diffraction pattern are usually plotted as the intensity of the detected X-rays against the angle 2θ window. This allows the possibility to determine the distance *d* between two planes, and therefore, to characterize the crystal structure (and phase composition in case of heterogenous samples) of the solid being tested. Each diffraction peak corresponds to a different set of (hkl) planes and can also be identified. Another information, which can be inferred from XRD measurements, is the crystallinity of a sample and the size of the crystallite based on the broadening of the peaks in the diffraction pattern, using the Scherer equation:

$$B = \frac{K\lambda}{\beta cos\theta}$$

B, mean crystallite size

K, shape factor constant

λ, wavelength of the X-ray

β, peak broadening at half the maximum intensity

(FWHM)

θ, angle of incidence
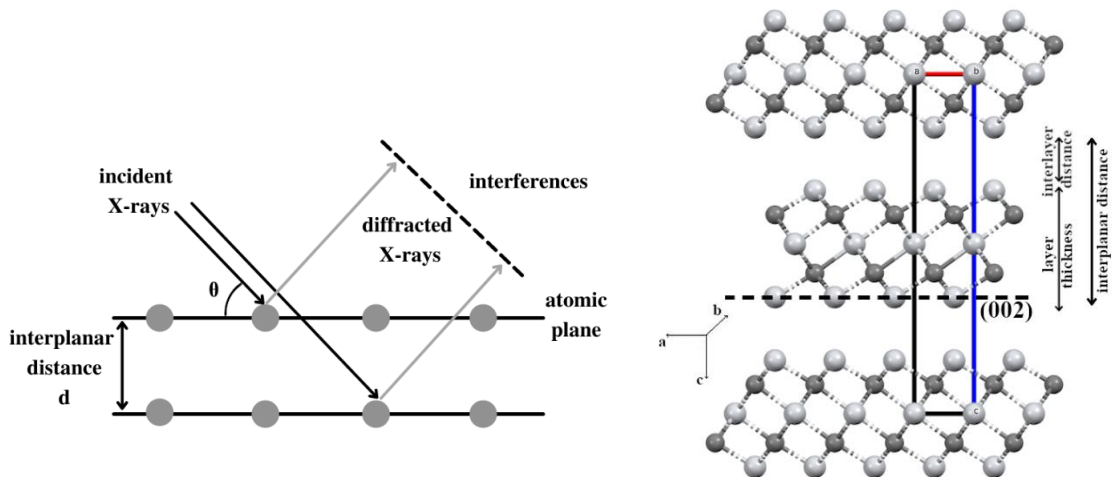
Figure 3.4: Schematic illustrating Bragg's law showing the orientation for which constructive interference happens for two in-phase X-rays scattered at different planes (left). Schematic of M_3X_2 MXenes, showing the relation between d-spacing of the (002) plane and the interlayer distance (right)

In this thesis, powder XRD was employed to characterize the samples and identify the phases of the materials synthesized by comparing with XRD patterns reported in the literature for the materials synthesized, as well as to monitor the interlayer spacing of the MXenes after intercalation with different precursors to evaluate the capacity of the MXene to be intercalated with said precursors. The powders were ground and pressed flat using a glass slide on a silica sample holder, unless stated otherwise. XRD measurements were done using a Rigaku SmartLab diffractometer (Rigaku, Tokyo, Japan) using a Cu Kα radiation as X-ray source, corresponding to λ = 1.54 Å, operating in reflection mode with Bragg-Brentano geometry. The measurements were done at a scan rate of $3°.min^{-1}$ and within a diffraction range between [4-50]°, unless stated otherwise, as the most characteristic peaks of Ti_3AlC_2 and Ti_3C_2 are within this diffraction window.

3.2.1.2. Scanning electron microscopy (SEM)

Scanning electron microscopy (SEM) is a microscopy technique which, unlike conventional optical microscopy, uses an electron beam to collect images instead of visible light beams. The electron beam is through a series of lenses before interacting with the sample. Where optical microscopes have a resolution limit of around 200 nm, SEM is an interesting technique to study nanomaterials, as its resolution can go even lower. Indeed, a typical SEM provides a resolution around 1-20 nm.[126] The resolution of a microscope can be given by the following equation:

$$\delta = \frac{0.61\, \lambda}{n\, sin\alpha}$$

where, λ is the wavelength of the beam,

n is the refractive index of the medium between

the lenses and the sample,

α is the angle of collection.

Based on this equation, it is possible to understand why SEM is a good technique to study nanomaterials compared to optical microscopy, as the resolution is directly proportional to the wavelength of the probing beam. An optical microscope uses visible light beam, which is greater than 390 nm, while the electron beam used in SEM can reach lower wavelength. For instance, a 10 kV electron beam have a wavelength of 0.0122 nm.

One of the particularities of SEM is that, except for very specific piece of equipment, it has to be performed under vacuum. It means that wet or hydrated samples cannot be analysed. Another characteristic of this technique is that the sample being imaged needs to be electrically conductive enough to allow the electrons to interact with the sample without getting trapped, which leads to

surface charging and a loss of resolution of the image. The electrons must be able to reach the sample, interact with it and leave the sample to achieve a good image resolution. The electrons can interact in different ways once they have reached the sample, and it can lead to the emission of electrons and X-rays: such as Auger electrons, secondary electrons, back-scattered electrons, characteristic X-rays, continuum X-rays and fluorescent X-rays.[126,127] These signals come from the interaction of the incident electron beam with the sample at varying depth below the sample surface. A schematic of the different types of signals which are emitted when an electron beam interacts with matter is shown in Figure 3.5. The SEM technique detects either secondary electrons or back-scattered electrons to form images of the sample. The secondary electrons are electrons that have been ejected from the conduction or valence bands of the atoms and have energies below 50 eV. Due to their low energy, they come from very superficial interactions with the sample, usually a few nanometres below the sample surface. Therefore, imaging done using secondary electrons gives a good topological representation of the sample under observation.[127] In the case of back-scattered electrons imaging, the electrons which are detected are high-energy electrons from the incident electron beam which have been back-scattered out of the specimen, after elastic scattering interactions with atoms of the sample. Due to the fact that high atomic number (Z) elements back-scatters electrons more strongly than low atomic number elements, the image obtained using back-scattered electrons displays a contrast based on variation in the elemental composition of the measured areas.[127] The SEM images shown in this thesis have been created using back-scattered electrons detection method.
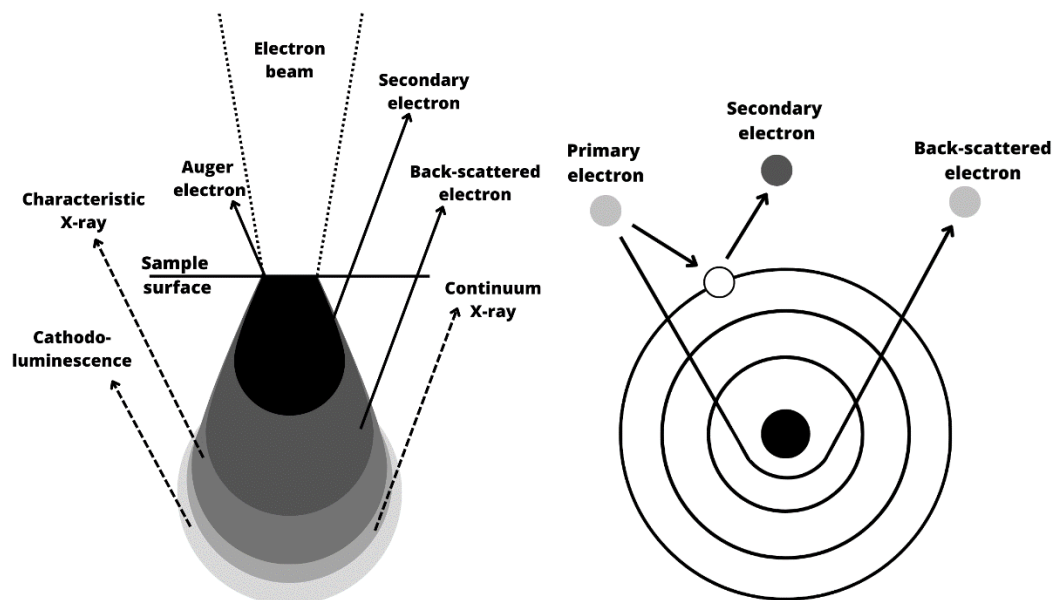
Figure 3.5: Schematic of the types of interaction possible between the incident electron beam and the sample (left) and schematic of the electron types detected by SEM microscopy for the imaging of a sample (right)

In this thesis, SEM was performed using a JEOL JSM-7800F (JEOL, Tokyo, Japan). An acceleration voltage of 5 or 10kV and a working distance of 10mm were used to study the morphology of the samples. The powders were dry cast onto carbon tape support, which was placed on top of a copper stub, before the SEM analysis.

3.2.1.3. Energy dispersive X-ray spectroscopy (EDS)

Energy dispersive X-ray spectroscopy is a very common technique to perform alongside SEM measurements. It is a technique which determines the elemental composition of the specimen being imaged. It can also return the elemental mapping of the image captured by SEM. EDS is useful for both qualitative and quantitative analysis, meaning that it permits the identification of both the type of elements which are present within the sample, as well as their proportions (%at or %w).

Figure 3.6 illustrates the basic principle of how EDS works. Essentially, in the case of an SEM-EDS, an atom of the sample can get into an excited state after interacting with an electron form the probing electron beam. An electron of the inner shell atom (e.g. K shell, which is the closest of the orbitals from the nucleus) is ejected and leaves a positively charged electron hole. Electrons from the outer shell (e.g. L shell) can now fill the vacancy. Based on the thermodynamics principle of conservation of mass and energy, the electron moving from the higher-energy outer orbital to the lower-energy inner orbital, releases the energy difference in the form of a radiation. The energy of the radiation produced is in the X-ray range of the electromagnetic spectrum, and its exact value is specific to an element and transition, which makes the elemental composition determination of the sample possible.[127]
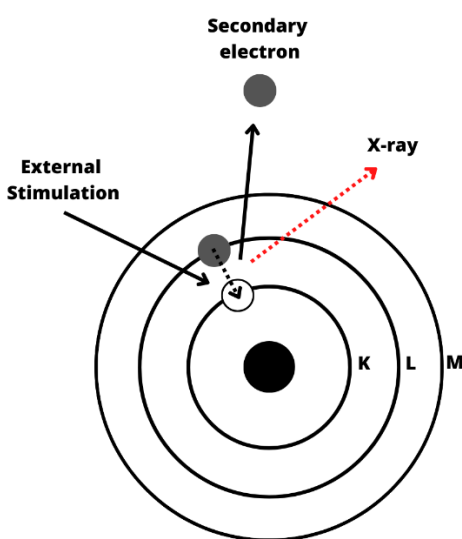
Figure 3.6: Schematic of the generation of an X-ray for EDS analysis

Some considerations concerning EDS should be highlighted:[127]

- some elements cannot be detected by EDS, such as H and He, which are elements with non-occupied higher-energy electron orbitals. Li and Be cannot be detected either, due to having too few electrons to be able to generate enough X-rays for detection.
- A shadow phenomenon can be present when characterizing samples with rough surfaces, which may lead to slight variations in results. A particular care concerning this phenomenon should be taken when characterizing powdered samples.

In this thesis, SEM-EDS was performed in a X-Max50 (Oxford Instruments, Abingdon, UK) using an accelerating voltage of 10 kV and a working distance of 10 mm, which was used to study the elemental composition.

3.2.1.4. Gas Sorption using Brunauer, Emmett and Teller characterization (BET)

Gas adsorption characterization using the Brunauer-Emmett-Teller (BET) technique has become the standard method to calculate the specific surface areas (SSA) of materials. BET is an extension to multilayer adsorption of the Langmuir theory, which deals with monolayer molecular adsorption.

Typically, a known amount of test sample is loaded into a physisorption tube, a vacuum is then set into that chamber, and a gas, usually nitrogen, is allowed into the chamber in a controller way, to be adsorbed onto the surface of the sample. In this process, a precise quantity of pure gas is introduced the test tube containing the materials, all while maintaining a constant temperature, which is 77K when using nitrogen. As the adsorption process unfolds, the pressure within this enclosed chamber decreases until it reaches a state of equilibrium. The quantity of gas adsorbed at this equilibrium pressure is determined by calculating the difference between the initially introduced gas amount and the gas needed to occupy the space surrounding the sample (the free space). Therefore, knowing accurately the free space around the sample is critical for precise and reproducible measurements. It is usually done using helium under experimental conditions before or after the sorption measurements. The sorption isotherm is constructed point-by-point by introducing more gas and repeating the previous procedure. From the isotherm, the SSA of the sample can be calculated using the BET formula based on the amount of gas adsorbed at multiple pressure points.[128,129]

Several types of physisorption isotherms can be obtained from gas sorption techniques (see Figure 3.7). Information about the type of porosity of the sample tested can already be extracted from the shape of the isotherm. The isotherms are classified in different types:

- Type I isotherms display a pronounced increase at low pressures, followed by a plateau at higher pressures. This initial increase suggests strong interactions between the adsorbate and adsorbent, while the plateau indicates saturation of the surface, with no further adsorption occurring at higher pressures. Type I isotherms are typically observed in microporous materials with small pores that limit gas uptake. I(a) isotherms are characteristic of (ultra)microporous materials, where pore sizes are less than 0.7 nm, while I(b) isotherms are associated with materials featuring larger micropores (pore sizes below 2 nm).

- Type II isotherms exhibit an increase at low relative pressures, followed by a knee and a "second increase" at higher pressures. This behaviour is indicative of more open materials, including non-porous or macroporous adsorbents, where the formation of substantial multilayers becomes possible. These isotherms tend towards "infinity" at higher relative pressures as the thickness of the adsorbed multilayer seems to increase without limit. The isotherm-knee, marked as Point B, denotes the transition from monolayer to multilayer adsorption.

- Type III isotherms do not show distinct monolayer formation due to weak adsorbate-adsorbent interactions. Instead, the adsorbed molecules are forming clusters around the most favourable sites of a non-porous or macroporous surface.

- Type IV isotherms resemble Type II isotherms in the sense that they involve both monolayer and multilayer formation. However, unlike Type II, in this case, the initial monolayer-multilayer adsorption in the mesopores is followed by pore condensation, which leads to the presence of a saturation plateau at higher relative pressure (p/p_0), which in certain cases, can merely be an inflexion point. These isotherms are typical for mesoporous materials, where pore sizes range from 2 to 50 nm. Hysteresis loops in the desorption branch, as seen in Type IV(a) isotherms, occur when capillary forces from condensed gases within mesopores hinder evaporation.

- Type V isotherms indicate weak adsorbate-adsorbent interactions, resulting in limited adsorption at low relative pressures. This is followed by rapid pore-filling due to condensation within the pores at higher pressures. Type V isotherms are commonly observed in situations such as water vapor condensation on hydrophobic surfaces.

- Type VI isotherms are characterized by step-like features, indicating layer-by-layer adsorption on irregular, non-porous surfaces.
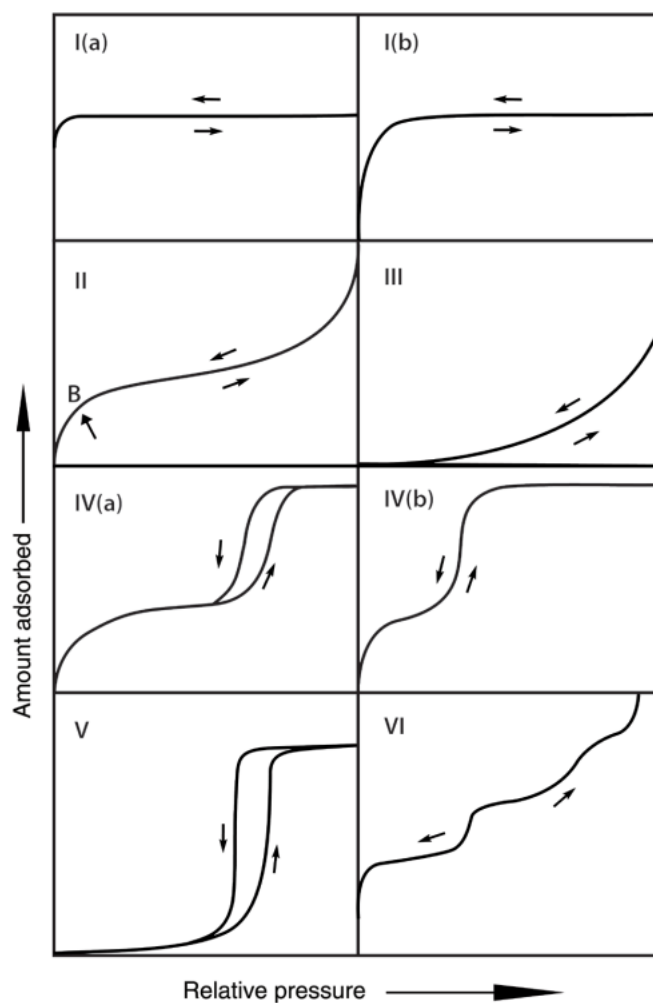
Figure 3.7: IUPAC Classification of physisorption isotherms [130]

The pore size distribution of the sample can also be determined from the adsorption isotherm using a variety of method. One of these methods is the non-local density functional theory (NLDFT), which is a common method for the determination of the pore size distribution of nanomaterials. The NLDFT method is based on a classical fluid density functional theory to calculate the adsorption isotherms in ideal pore geometries (e.g. N_2 adsorption in the split-pore model at 77 K).[131] A complex mathematical fitting is then performed between the experimental isotherms with the various isotherms calculated to determine the pore size of the sample.

Gas sorption measurements were done on a Micromeritics 3Flex gas sorption analyser (Micromeritics Instrument Corporation, Georgia, USA) using high purity nitrogen gas at 77K. SSAs were calculated from the measured gas sorption isotherms using the BET method over a relative pressure P/P_0 window of 0.05-0.15. The pore size distributions were calculated by employing the NLDFT method with a slit pore model.

3.2.1.5. X-ray photoelectron spectroscopy (XPS)

The surface chemistry of materials is undoubtedly a critical factor for various applications, especially for catalysis, as it is through their surfaces that materials interact with their environment. The surface chemistry will influence several materials properties, such as catalytic activity, wettability, corrosion mechanisms and so on.

The X-ray photoelectron spectroscopy technique is used to investigate the surface chemistry of materials or samples and help to understand how the different elements interact with each other. An incident X-ray ejects an electron from an atom of the studied sample. The ejected electron is then detected by the spectrometer, which measures the kinetic energy (KE) of the electron.[132] The process is described on Figure 3.8. The kinetic energy measured can then be converted to binding energy (BE) using the following equation:[132]

$$BE = h\nu - (KE + \varphi)$$

where, $h\nu$ is the energy of the X-ray photon

φ is a work function correction for the sample studied
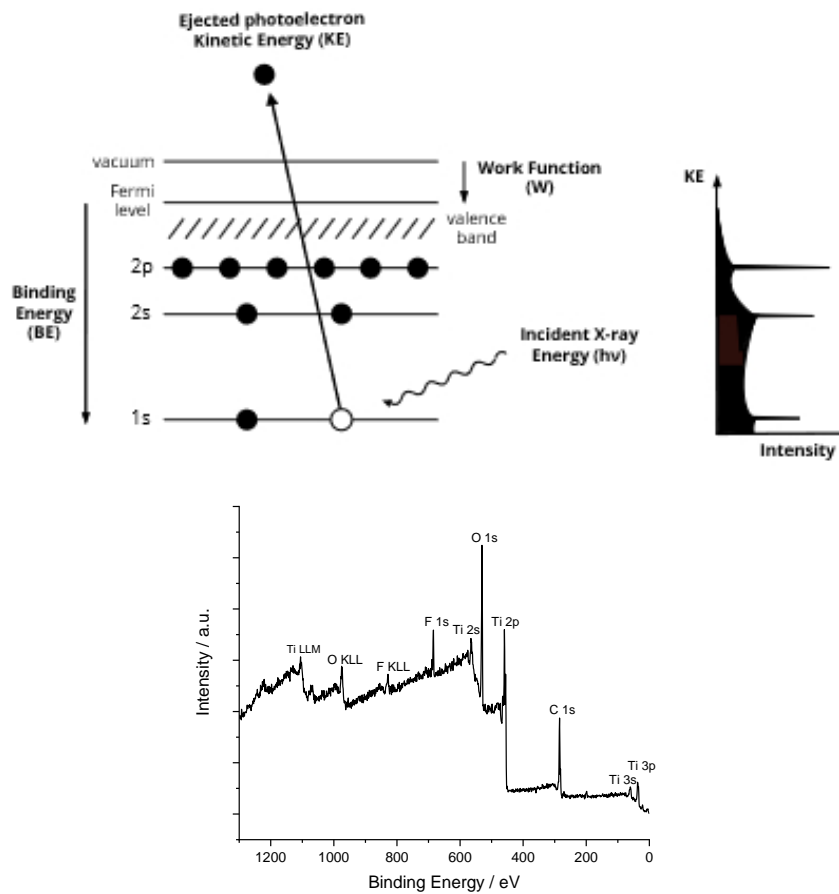
Figure 3.8: Schematic diagram of the XPS process (top) and example of the XPS spectrum for Ti₃C₂Tₓ MXene (bottom)

The binding energy calculated depends on several factors:

- the element from which the electron was ejected,
- the orbital of the ejected electron,
- the chemical environment of the atom from which the electron was ejected.

This makes XPS analysis a very good method to identify the elemental composition in a sample, the oxidation states of the elements and their chemical environment. Moreover, the electrons ejected during the XPS measurements have a very small escape depth within the sample, usually around 0.3-4 nm depending on the energy of the incident X-ray beam and the kinetic energy of the electron.[132] Therefore, XPS is a very superficial characterization technique, which allows for the chemical characterization of a sample's surface, which is ideal for several types of studies, such as the study of electrochemical materials. Indeed, the surface chemistry of a electrochemical materials or catalysts is key when it comes to their electrochemical properties, as the interface between the surface of the sample and the electrolyte is where the electrochemical reactions happen.

In this thesis, XPS was performed using a Thermo Fisher Scientific NEXSA spectrometer. The analysis was done using a micro-focused monochromatic Al X-ray source (19.2 W) over an area of approximately 100 µm. Data were recorded at pass energies of 150 eV for survey scans and 40eV for high-resolution scan with 1 eV and 0.1 eV step sizes, respectively. Charge neutralization of the sample was achieved using a combination of both low energy electrons and argon ions. Cluster cleaning was performed with 2 keV energy at 0.5 x 0.5 mm area for 60 s to remove possible surface contaminants.

To get a more precise deconvolution of the different peaks in the XPS spectra, several constraints were applied during the peak-fitting of the samples. The constraints are as follow and were met for most of the components during the fitting:

- Despite the fact that higher binding energy tails have been reported for MXenes in other studies[133], which would require a peak-fitting with asymmetric Gaussian-Lorentzian peaks, a gaussian-type distribution was chosen to make the deconvolution easier. It was assumed that a deconvolution of the XPS spectra with Gaussian components would not prejudice the analysis of the surface chemistry of the samples.
- The different component and their initial binding energy values were taken and based on studies focusing on the chemistry of MXenes, especially Ti_3C_2, carbides, nitrides, carbons, and N-doped carbons materials.
- The binding energy shift for a given component was constrained within a $\pm$ 0.5 eV window around the initial value.

- The full width at half maximum (FWHM) of a specific component was set, so that its value for a specific component would be similar in the different samples which would contain it.

In addition to these restrictions, another parameter specific to the Ti 2p spectra peak-fitting has been considered due to the $2p_{1/2}$ and $2p_{3/2}$ components:

- The peak splitting was kept within a window of 5 to 6 eV, as it englobes the values which have generally been reported for the peak splitting between Ti $2p_{1/2}$ and Ti $2p_{3/2}$ for different Ti oxidation states.[134]
- The intensity ratio between the Ti $2p_{1/2}$ and Ti $2p_{3/2}$ has also been restricted:

$$I_{2p_{3/2}} = {I_{2p_{1/2}}}/{2}$$

3.2.1.6. Raman spectroscopy

Raman spectroscopy is a characterization technique which uses energy changes in inelastic scattered photons to study bonds in a sample, either solid, liquid or gas. Visible light of a fixed wavelength is focused onto the sample using a microscope. The light excites the vibrational mode of the atoms (phonons) in the sample, causing them to move to a higher energy state through "virtual states". Three types of scattering can occur: Rayleigh scattering, Stokes Raman scattering and Anti-Stokes Raman scattering. In the case of Stokes Raman scattering phenomenon, , some of the energy of the radiation is absorbed, which changes the energy of the photons by the amount absorbed. This change in energy is the so-called Raman shift and corresponds to a peak on the Raman spectrum. The Raman shift differs depending on the materials and the vibrational modes, which means that a Raman spectrum can be used to identify the material and the vibration modes and corresponding bonds in a sample. The other two modes, anti-Stokes scattering and Rayleigh scattering, corresponds to scattered photons which gained energy, or which did not undergo any energy change respectively. The anti-Stokes scattered photons signal is pretty weak and does not influence measurements, while the Rayleigh scattered photons make most of the signal and need to be filtered out before detection.[135]

Raman spectroscopy was done using a Horiba Lab Raman Spectrometer (Horiba, Minami-ku Kyoto, Japan) with an EM-cooled Synapse camera. The powder to analyse was pressed between two glass microscope slides to give a flat MXene particles for measurements. One of the slides was removes and the slide with the MXene powder is laid flat under the diode laser (532 nm, 200 µW) for analysis. A 100x, 0.9 NA microscope objective was used for taking spectra.

3.2.1.7. ^{57}Fe Mössbauer spectroscopy

In Mössbauer spectroscopy, three types of nuclear interactions can typically be observed: the isomer shift, which is caused by differences in the electron densities near the nucleus; quadrupole splitting, which is caused by atomic-scale electric field gradients; and magnetic Zeeman splitting, which is caused by non-nuclear magnetic fields. The high energy and narrow line widths of nuclear gamma rays make Mössbauer spectroscopy a very sensitive technique for measuring energy (and therefore frequency) with high resolution.[136,137]

^{57}Fe Mössbauer spectroscopy was done with a ^{57}Co in Rh source in motion at constant acceleration. It was carried out on the Ti_3C_2-U10-Fe-800, Ti_3C_2-U50-Fe-800 and C-U50-Fe-800 at 296 K over a velocity range of $\pm$ 12 mm.s^{-1} using a See Co W304 and W202 drive unit and 1024 channel spectrometer. Natural alpha iron coil was used to calibrate the velocity scale. The samples were prepared by loading the powders into Perspex sample holder (adsorber discs), which is gamma transparent.

3.2.2. Electrochemical characterization

The catalyst prepared, once characterized, were electrochemically tested to determine their different properties and to evaluate their activity towards ORR. Several methods are available and complement each other to obtain electrochemical properties, such as electrochemical surface area (ECSA), n, limiting current j_L, kinetic current j_k, stability…

3.2.2.1. Rotating ring electrode (RDE) and rotating ring-disk electrode (RRDE) setup

The rotating disk electrode method (RDE) is one of the simplest and most powerful techniques to evaluate the electrocatalytic performance of electrocatalysts towards ORR. Key performance indicators can be extracted from the RDE data, through different set of measurements. A typical RDE setup is presented on Figure 3.9 and consists of an electrochemical cell filled with the electrolyte and three electrodes to perform the measurements: a reference electrode, a counter electrode (usually graphite or Pt), and a working electrode which is connected to a rotating shaft, on which the electrocatalyst is going to be deposited prior to the measurements.

Rotating ring-disk electrode method (RRDE) has been recognized to be an essential tool to characterize the fundamental properties of electrocatalysts towards ORR. As described earlier, the ORR process can go through a 4-electron pathway or a 2-electron pathway, in which peroxide intermediate product are formed. The RRDE, with its ring set at a specific potential to react with the peroxide by-products, allows to determine how much intermediate product is formed relative

to the amount of oxygen being reduced at the disk by comparing the current drawn at the ring and the disk throughout the electrochemical measurements.
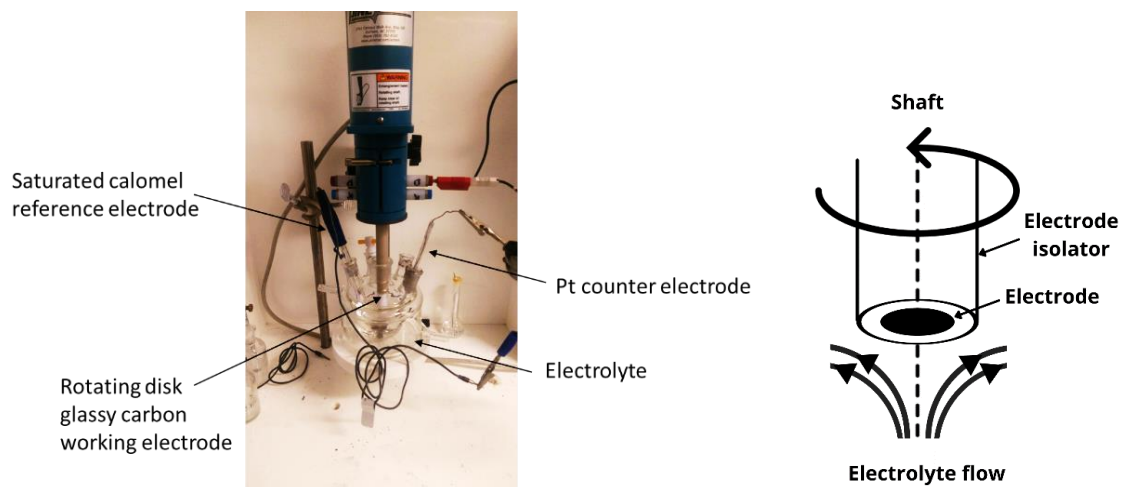
Figure 3.9: RRDE setup (left) and rotating disk schematic (right)

Electrochemical characterization of the samples was performed at room temperature in Pine Instruments RDE/RRDE electrochemical cell with a modulated speed rotator (Pine Research Instrumentation, Durham, USA), using a saturated calomel electrode (SLS, Nottingham, UK) as the reference electrode, a coiled Pt wire as the counter electrode and a glassy carbon (GCE) disk RRDE tip (disk diameter: 5.61 mm) and a platinum ring (ring diameter:) as the working electrode. The catalysts inks were prepared as follow. Around 5 mg of catalysts powder were added to 480 µL absolute ethanol and 20 µL of Nafion solution (5%wt). It was then ultrasonically dispersed for 30 min to form a homogenous ink. Breaks were taken during the ultrasonication to change the water of the ultrasonic bath to keep the temperature below 35 °C. Before casting the ink, the working electrode was polished using an alumina slurry (Ø 0.3 µm) and subsequently bath sonicated for 5 min, rinsed with DI water, and left to dry. 10 µL of the catalysts ink were spin-casted on the GCE while rotating at 500 rpm to give a homogenous coating on the electrode to obtain the desired mass loading of catalyst ($\sim$0.40 mg.cm^{-2}). It was then left to dry for 30 minutes in air before running the electrochemical experiment.

Before doing the electrochemical tests, cyclic voltammetry (CV) was performed at a scan rate of 50 mV.s^{-1} for 50 cycles within [0.1;1] V (vs RHE) potential window to activate the catalyst under N_2 flow. Moreover a few CVs were run before the measurements in N_2 and air until stable.

The RDE tests were performed by Linear Sweep Voltammetry (LSV) running an anodic sweep between [0.1;1.1] V (vs RHE) at varying electrode rotation speed ranging from 400 to 1600 rpm at a scan rate of 5 mV.s^{-1} in N_2 and air. The LSVs of the different samples in air obtained were then iR corrected and the N_2 component was subtracted. To determine the iR correction, EIS was performed prior to the measurements and the value for the real part of the impedance at high

frequency of the Nyquist plot (see Figure 3.10) was used for iR correction of the following measurements.
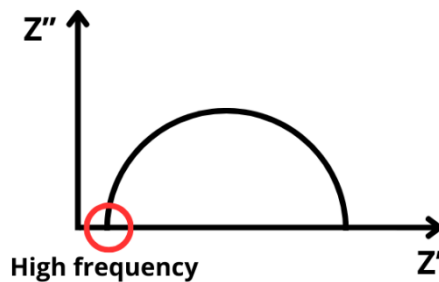
Figure 3.10: Nyquist plot

For the conversion of the potential measured vs SCE against RHE, the following equation was used:

$$E_{RHE} = E_{SCE} + 0.059 \times pH + 0.2445$$

3.2.2.2. RRDE measurement analysis

RRDE measurements are useful to analyse the extent of each reaction pathways involved during the ORR on a specific electrocatalyst. RRDE allows for the monitoring of oxygen reduction current from the electrocatalyst on the disk, while simultaneously detecting products generated during the ORR on the disk through a coaxial ring set at a fixed potential. The potential at which the ring electrode is set must be between the potential at which the diffusion limit is reached for the oxidation of the generated intermediates, which are H_2O_2 in acidic media and HO_2^- in alkaline media for ORR, and the onset potential for the oxidation of OH^- to O_2.[26] RRDE measurements were performed by LSV running an anodic sweep between [0.1;1.1] V (vs RHE) (disk) at 1600 rpm at a scan rate of 5 mV.s^{-1}, while the ring was held at 1.3 V vs RHE. The electron-transfer number (n) and the yield of hydrogen peroxide (HO_2^-) released during the ORR were calculated using the following formulas:

$$n = \frac{4I_dN}{I_dN + I_r}$$

$$\%H_2O_2 = 100\frac{2I_rN}{I_dN + I_r}$$

I_d, disk current

I_r, ring current

N, current collection of the ring

3.2.2.3. Stability testing: Accelerated Durability Test (ADT)

To test the electrochemical stability of the different samples, an accelerated durability test was performed. The ADT was done by cycling the different samples between [0.5;1] V (vs RHE) for 2000 cycles sweeping at 50 mV.s^{-1} rate. To evaluate the stability, LSVs of the samples was performed post-cycling and compared to the LSVs pre-cycling. Any shift from the pre-cycling LSV would show a change in activity of the samples, coming from degradation of the materials.

CHAPTER 4: Physicochemical characterization of N-Carbon on N-Ti$_3$C$_2$

4.1. Introduction

As mentioned earlier, MXenes are very versatile materials with tuneable properties, due to their various chemistries and surface groups (-F, -O, -OH, -Cl, etc.), as well as the possibility to be intercalated and/or delaminated and then decorated/functionalized to tune their properties for specific applications. MXenes have both been used as catalysts and as supports for catalysts materials. The MXene support can also play a role during the catalysis as catalyst themselves, for instance Mo$_2$C MXene for HER, which has shown some good activity.[138] Concerning ORR, Ti$_3$C$_2$ has been tested and the activity of its multi-layer form and its single-layer form have been compared.[101] Although an improvement in terms of activity has been reported when Ti$_3$C$_2$ has been completely delaminated into single layers, the overall activity of the materials is far from benchmark catalysts. A theoretical study from Zhou et al. has found that there was an ORR activity improvement when MXenes have been combined with N-doped graphitic carbon, as heterostructures.[139]

Moreover, concerning MXene synthesis and processing, a common obstacle comes whilst trying to create and maintain a stable architecture without layer restacking. Indeed, MXenes have a tendency towards layer restacking, which would hinder the properties and the overall performance of the materials.[140] As-synthesized Ti$_3$C$_2$ SSA usually ranges between 4-15 m^2.g^{-1},[141,142] while carbon black, which are supports used to deposit catalysts, have a SSA around the hundreds of m^2.g^{-1}.[143,144] It means that overall, there is a lot less surface available for electrochemical reactions to happen on the MXene layers compared to conventional catalysts.

In this chapter, the focus is given in trying to develop a way to deposit nitrogen-containing carbon structures on top of Ti$_3$C$_2$ MXene, while preventing MXene layer restacking phenomenon, to allow for more of the materials' surface to be available for electrochemical reactions. The strategy selected to meet these objectives is to find a precursor containing nitrogen and carbon to intercalate between the MXene layers, and to perform a thermal treatment for N-containing decomposition products to form on the surface of the MXenes, which would also serve as pillars to avoid restacking of the structure. The physico-chemical properties of the materials are presented, analysed, and compared between each other to understand the influence of parameters

such as urea content and thermal treatment temperature. Moreover, the analysis of these properties is going to be useful to compare ORR properties of the samples in CHAPTER 5:

4.2. Results and discussion

4.2.1. Ti₃C₂ MXene synthesis and intercalation with various Nitrogen precursors

4.2.1.1. Initial MXene synthesis and characterization

The Ti_3AlC_2 MAX phase (>85% purity, Carbon Ukraine Ltd.) was etched using the HCl + LiF method, first reported by Ghidiu et al.,[77] to produce the as-synthesized $Ti_3C_2T_x$ MXene. The MXene samples were then washed and centrifuged several times before being processed further. Refer to the experimental chapter (CHAPTER 3: Materials and methods) for the detailed MXene $Ti_3C_2T_x$ synthesis protocol.
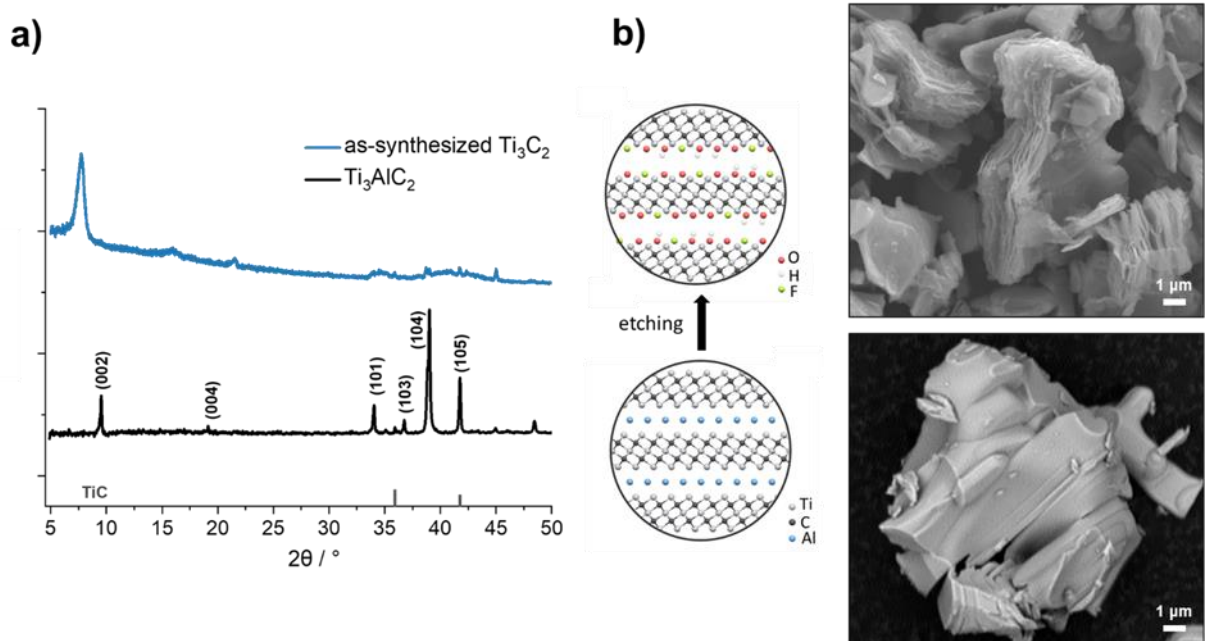
Figure 4.1: (a) XRD pattern and (b) Schematics and SEM pictures of Ti₃AlC₂ MAX phase and as-synthesized Ti₃C₂ MXene

An initial XRD measurement has been performed to evaluate the successful etching of the MAX phase precursor into its MXene counterpart. The XRD patterns are given in Figure 4.1.a and the pattern for $Ti_3C_2T_x$ is characteristic of what would be expected from this MXene compared to its starting Ti_3AlC_2 MAX phase.[58,75,77,99] The low angle peak corresponding to the (002) basal crystallographic plane of Ti_3AlC_2 shifted to lower 2Θ (~ 7.8°), proving successful etching and exfoliation of the materials. Based on Bragg's equation, the d-spacing of the (002) plane for the MAX phase d-spacing which is at around 0.93 nm for a measured 2θ of 9.5°; which is close to what some literature have reported for the thickness of a single Ti_3C_2 layer, which is 0.95nm.[145]

On the other hand, the *d*-spacing for the synthesized MXene calculated from its XRD pattern is around 1.13 nm for a measured 2θ of 7.8°, which gives us a Ti_3C_2 interlayer spacing of 0.20 nm. Moreover, non-basal planes peaks of the parent MAX phase have been greatly attenuated or have disappeared from the XRD pattern, suggesting the successful removal of the Al layer and exfoliation of the MXene layers, which is also supported by the SEM pictures taken of both Ti_3AlC_2 and $Ti_3C_2T_x$ (Figure 4.1.b) showing the exfoliated, but not completely delaminated, accordion-like MXene layer stack, compared to the parent MAX phase. To confirm the etching of the Al layer of the MAX phase, EDS measurements on the etched sample has been performed and the EDS spectra of the as-etched MXene is shown in Figure 4.2. First, the EDS shows a low amount of Al, confirming the successful etching of the Al layer of Ti_3AlC_2. The Al detected in the samples are mostly due to some unwashed fluoride salts left in the sample. The slightly higher C composition of the MXene relatively to the MXene stoichiometry can be attributed to carbonaceous impurities (support) or a slight over-etching. Moreover, as the powders were immobilized on carbon tapes, the EDS measurements were done on bigger particles, as close as possible, and preferably on the top of the flakes. Even so, the carbon content using EDS is most likely overestimated.
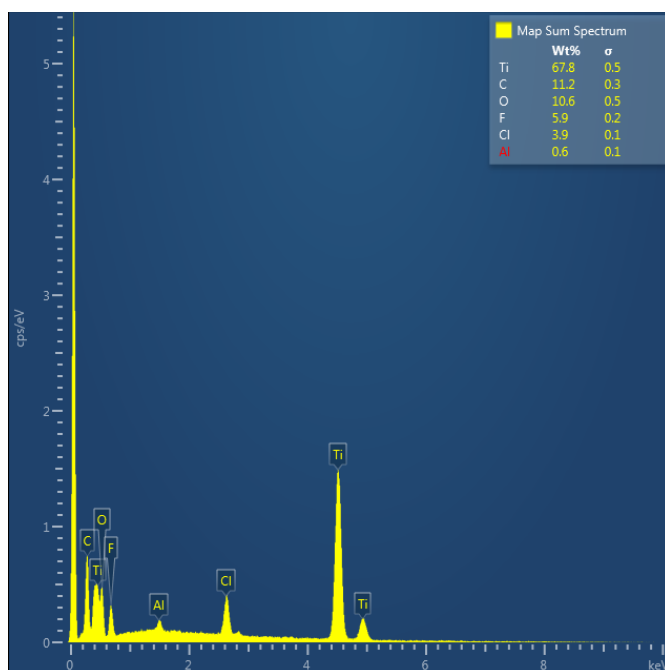
Figure 4.2: EDS spectra of the as-synthesized Ti3C2

4.2.1.2. Intercalation of the MXene with different Nitrogen precursors

The approach that has been selected in this work to get N-Carbon on N-doped Ti_3C_2 is through a two-step process. First, the synthesized MXene and a nitrogen precursor are mixed together using the procedure described in the Materials and methods section. The MXene/precursor mix is then

annealed in a tube furnace under Ar atmosphere to prevent the MXene from been oxidized by oxygen during the thermal treatment if the tube furnace had not been purged.
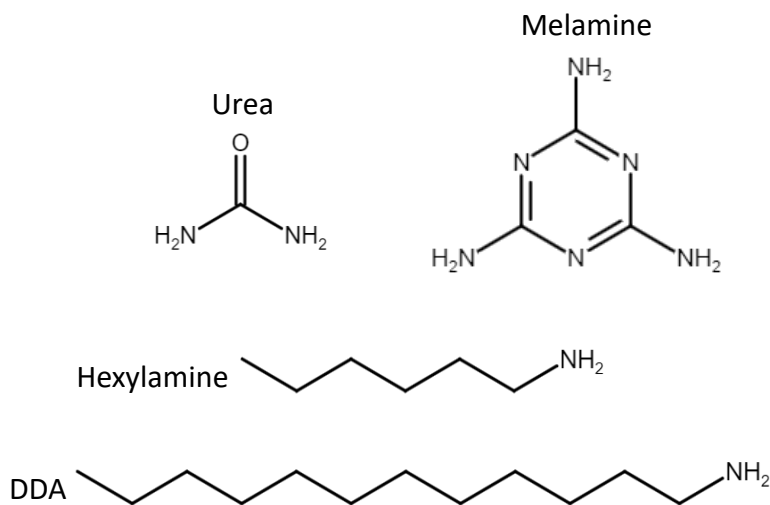
Figure 4.3: Chemical structure of the nitrogen precursors

Before proceeding to the thermal treatment aiming getting our heterostructure, a preliminary experiment has been designed to determine which nitrogen precursor is the most suited for synthesis. During this experiment, the MXene were mixed with four different nitrogen containing precursors, namely urea, melamine, hexylamine and dodecylamine in a 1:1 mass ratio and ground together with a pestle and mortar to evaluate which precursor intercalates better between layers within the MXene structure. The chemical structures of the different precursors are given in Figure 4.3. Another aspect that has been studied for this experiment is the influence of a pre-treatment of the MXenes in 0.1 M NaOH solution for 30 min before being filtered and dried, to change the chemistry of the MXene surface.

The idea behind that experiment is that it would be expected that the precursor which can easily be intercalated between the MXene layers, would allow for a more homogenous synthesis later on during the thermal treatment, and would as well be better at stopping the restacking of the MXene layers.

The different Ti_3C_2 / nitrogen precursor mixes have been run through XRD measurements to evaluate if the MXene has been intercalated and the different XRD patterns are presented in Figure 4.4 for the as-synthesized Ti_3C_2 and in Figure 4.5 for the Ti_3C_2 which was treated with NaOH, denoted Ti_3C_2-alk. The inset shows the [4-10]° 2θ portion of the XRD pattern, which is where it can be determined if the intercalation have been successful, and the degree of intercalation.
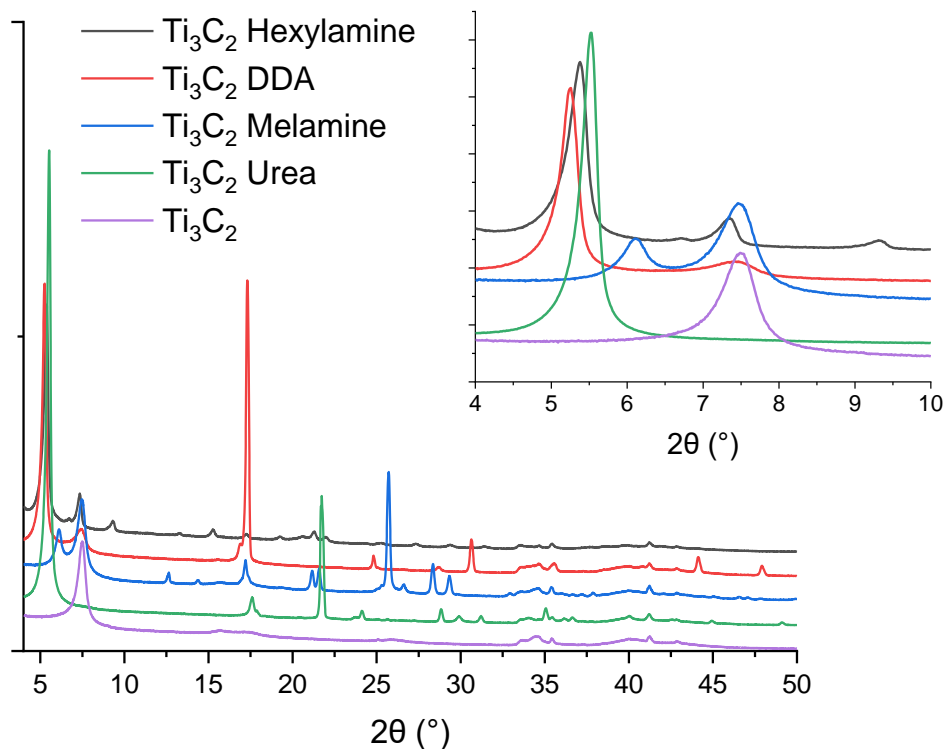
Figure 4.4: XRD pattern of as-synthesized Ti₃C₂ intercalated with different precursors: no precursor, urea, melamine, hexylamine, DDA (inlet: low angle (4-10°) pattern)
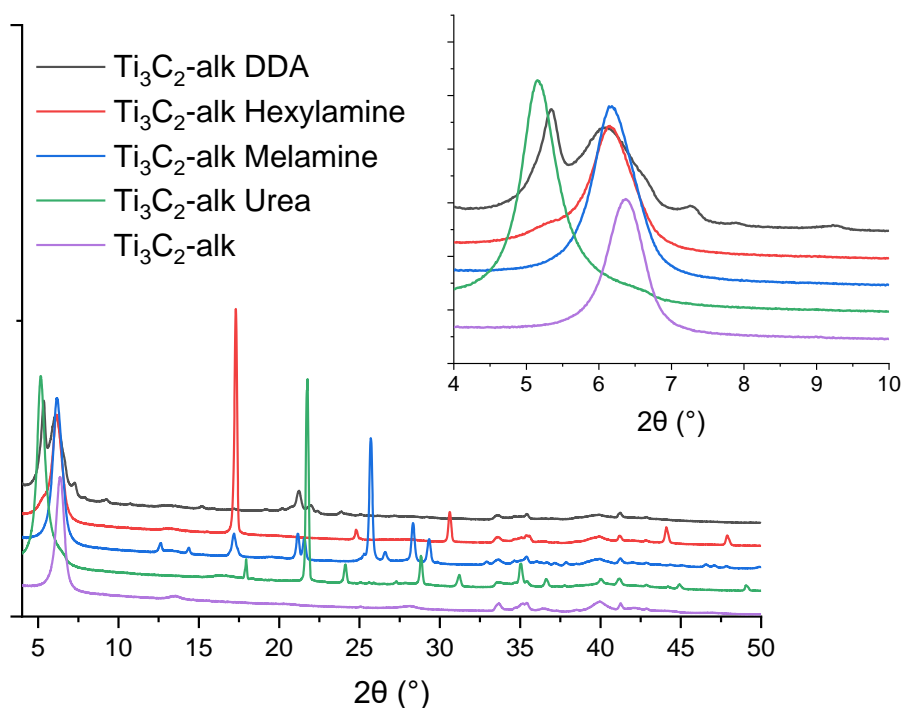
Figure 4.5: XRD pattern of NaOH treated Ti₃C₂ intercalated with different precursors: no precursor, urea, melamine, hexylamine, DDA (inlet: low angle (4-10°) pattern)

Based on XRD pattern of Ti_3C_2 and Ti_3C_2-alk, it seems like the NaOH treatment did modify the surface composition of the MXene layers, as the intercalation of the different nitrogen precursors differs if a pre-treatment has been performed or not. To better understand the surface composition of the Ti_3C_2 layer surface with or without NaOH treatment, Raman spectroscopy was performed on both Ti_3C_2 and Ti_3C_2-alk, and the results are presented in Figure 4.6. Raman spectroscopy has been a technique that has been used to study MXene surface groups successfully,[146,147] especially for Ti_3C_2-OH and Ti_3C_2-O terminations, which are hard to distinguish using other techniques. The as-synthesized Ti_3C_2 sample displays several peaks. Based on theoretical studies, the peak at 206 cm^{-1} can be assigned to Ti-O (E_g) surface groups, while the peak seen at around 275 cm^{-1} corresponds to Ti-OH (E_g) terminations. Moreover the wide peaks at around 400 cm^{-1} and 600 cm^{-1} are convoluted peaks corresponding to vibrational modes of Ti-O/H/OH surface groups.[146] The peak detected at around 1600 cm^{-1} is attributed to carbon, which could be from impurities or slight over etching of the MXene. After the NaOH treatment, Ti_3C_2-alk still shows the peak at 206 cm^{-1} but the peak now displays a shoulder towards increasing cm^{-1} which could be attributed to sodium ions interacting with MXene surface groups. Previous studies have reported the interaction of Na ions after NaOH treatment, forming Ti-O-Na on the surface of Ti_3C_2.[148,149] The shoulder covers the position where the Ti-OH (E_g) peak should be. It is therefore challenging to make any conclusions about Ti-OH terminations. The other peaks, consisting of the overlap of Ti-O, Ti-OH and Ti-F terminations, are still present at around 400 cm^{-1} and 600 cm^{-1}, as well as the carbon peak at 1600 cm^{-1}. In conclusion, the NaOH treatment seems to have slightly modified the MXene surface chemistry, by forming some Ti-O-Na terminations.

For the as-synthesized MXene, it seems like all nitrogen precursors have managed to be intercalated between the MXene layers, at least to some extent. Indeed, only the Ti_3C_2 / urea mix displays a single (002) peak that has been shifted to lower 2θ value, at around 5.5° compared to a value of 7.5 for the bare MXene, which demonstrates an increase of the interlayer distance compared to the bare MXene. The other compounds have only managed to partially intercalate and display two (002) peaks. The first one corresponding to intercalated MXene layers, which are at around 5.3°, 5.4° and 6.1° for DDA, hexylamine and melamine respectively. And the other one close to the original MXene (002) peak, meaning that the MXene intercalation is not homogenous throughout the sample. It seems that for the untreated MXene, although the DDA and hexylamine seem to allow for slightly bigger interlayer spacing, urea is the most straightforward compound to intercalate, as it readily intercalates without the help of specific experimental conditions.

The NaOH treated Ti_3C_2 displays a (002) peak at 6.5° 2θ. It seems that the treated MXene has some trouble intercalating the different intercalants except for urea, which almost completely intercalates. Indeed the (002) peak is visible for melamine, hexylamine and DDA, showing the failed intercalation of the different compounds, although the hexylamine and the DDA managed

70

to intercalate partially into the layers, as shown by the presence of an extra XRD peak at lower 2θ value. Moreover, the urea displays a small shoulder at 6.5°, which shows that Ti_3C_2-alk was not completely intercalated.
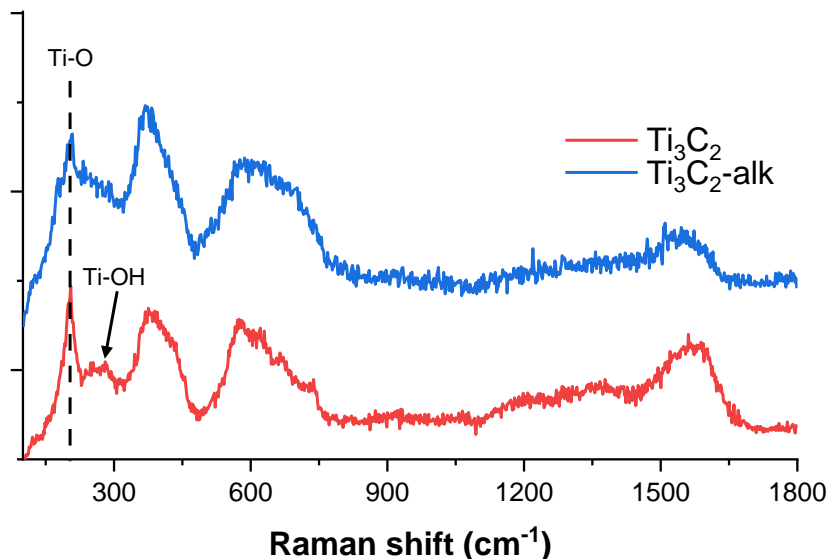
Figure 4.6: Raman spectra of the as-synthesized Ti₃C₂ and the NaOH treated Ti₃C₂-alk with surface group peaks highlighted

Based on both XRD and Raman measurements, it seems that the NaOH treatment has hindered the intercalation of the different compounds to a lesser or greater extend depending on the chemical used for the intercalation. This could be due to the formation of Ti-O-Na terminations during the NaOH treatment, or a variation in Ti-O / Ti-OH surface groups proportions. Further study would be necessary to understand the mechanisms in play but is out of scope for this work. Out of all the nitrogen precursors tested for the intercalation, urea was the one that managed to intercalate the best. Therefore, it was decided to use urea for the following experiments.

4.2.2. Preparation and characterization of N-Ti₃C₂ MXene using urea

Once the nitrogen precursor selected, the $Ti_3C_2T_x$ MXenes were intercalated with different amount of urea, namely 1:1, 1:10 and 1:50, MXene to urea mass ratio in a solution of DI water at 55°C for 15 hours. The mixture was then dried under a nitrogen flow before being thermally treated as described in the experimental section.

4.2.2.1. Crystal and chemical structure

A preliminary XRD measurement of the Ti_3C_2-urea mix before the pyrolysis has been done to show that the MXene has indeed been intercalated with urea. The XRD pattern is given in Figure

4.7, as well as the XRD measurements of the initial Ti_3AlC_2 MAX phase and the as-synthesized $Ti_3C_2T_x$. The $Ti_3C_2T_x$ XRD pattern for the 1:1 Ti_3C_2 to urea mass ratio powder before pyrolysis is shown for visibility purposes (the XRD patterns for 1:10 and 1:50 mix are similar but not as practical to read due to the amount of urea in the samples). The pattern clearly shows a shift of the low angle peak corresponding to the (002) crystal plane, without (002) peak at the original 7.8° position. Given Bragg's law, this decrease of the peak position of the (002) planes indicates an increase of the lattice parameter along the [00l] direction and therefore a larger interlayer distance for the Ti_3C_2-urea sample compared to the as-synthesized MXene. It shows successful and complete intercalation of urea between the MXene layers. The ease of intercalation of urea into the MXene layer can be attributed to its small size as well as its ability to interact with MXene surface groups through hydrogen bonding with -O and -OH MXene surface groups.[150,151] Moreover the principal XRD peaks of urea are present in the Ti_3C_2-urea XRD pattern. It could be noted that the intercalated species are not only urea, but most likely also contain ammonium ions due to partial urea decomposition, as previously reported in another study.[150] In addition to that, no TiO_2 peaks, either anatase or rutile are visible on the as-etched Ti_3C_2 or urea-intercalated Ti_3C_2, showing that no MXene oxidation took place during the intercalation step. It must be noted that all samples contain some TiC impurities coming from the MAX phase synthesis and can be observed from the small TiC XRD peaks appearing in the measurements.
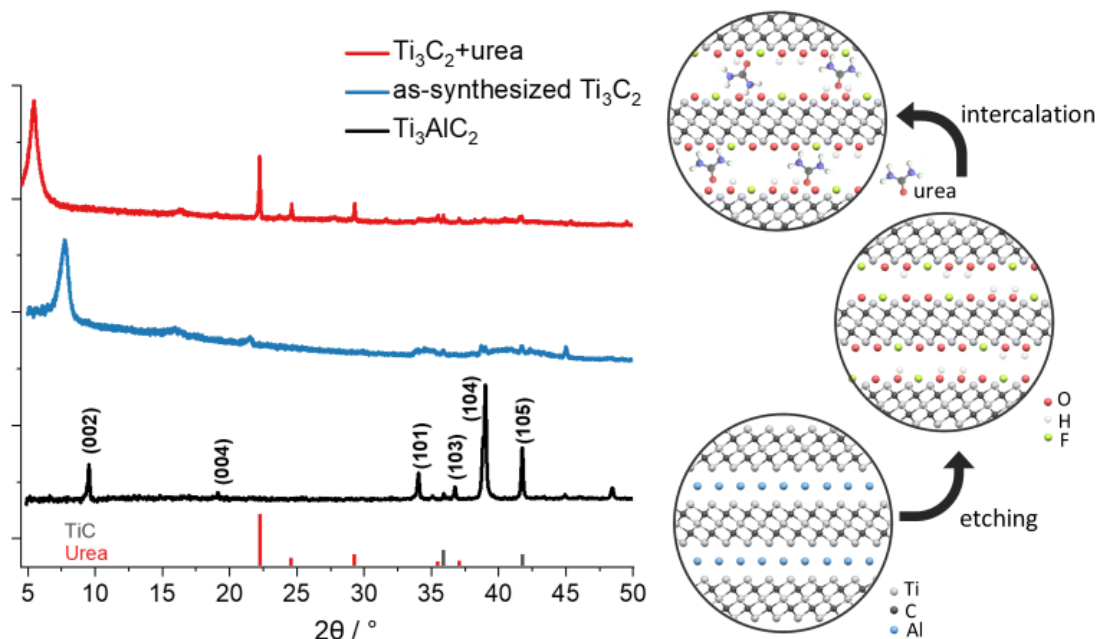
Figure 4.7:XRD pattern of Ti_3AlC_2 MAX phase, as-synthesized $Ti_3C_2T_x$ MXene and urea-intercalated Ti_3C_2 (1:1 MXene:urea) before thermal treatment (insets: schematics showing the changes in interlayer spacing after etching and intercalation)

After controlling the proper intercalation of urea within the MXene layers and the non-oxidation of MXene during the intercalation process, MXenes samples with different amount of urea were prepared and thermally treated at 550°C under argon following the protocol given in the method section 3.1.2: 1:1, 1:10 and 1:50 MXene to urea by mass, namely Ti_3C_2-U1-550, Ti_3C_2-U10-550 and Ti_3C_2-U50-550 respectively. The objective of this step is the degradation of urea and reaction with the MXenes to modify its surface chemistry, as well as allowing to form some decomposition products, which would act as pillars to avoid a close restacking of the MXene layers, as well as increase the surface area and the amount of electrochemically active sites available for ORR. The morphology and surface chemistry of the samples will be discussed in section 4.2.2.2. The chosen temperature was 550°C, as it is the temperature at which it has been widely reported that urea decomposition process in a covered crucible yields g-C3N4 as a product.[124,125] A reference sample with only urea has gone through the same thermal treatment and the XRD pattern is shown in Figure 4.8 (top) at the very top of the graph and is characteristic of the XRD pattern found in the literature for g-C_3N_4.
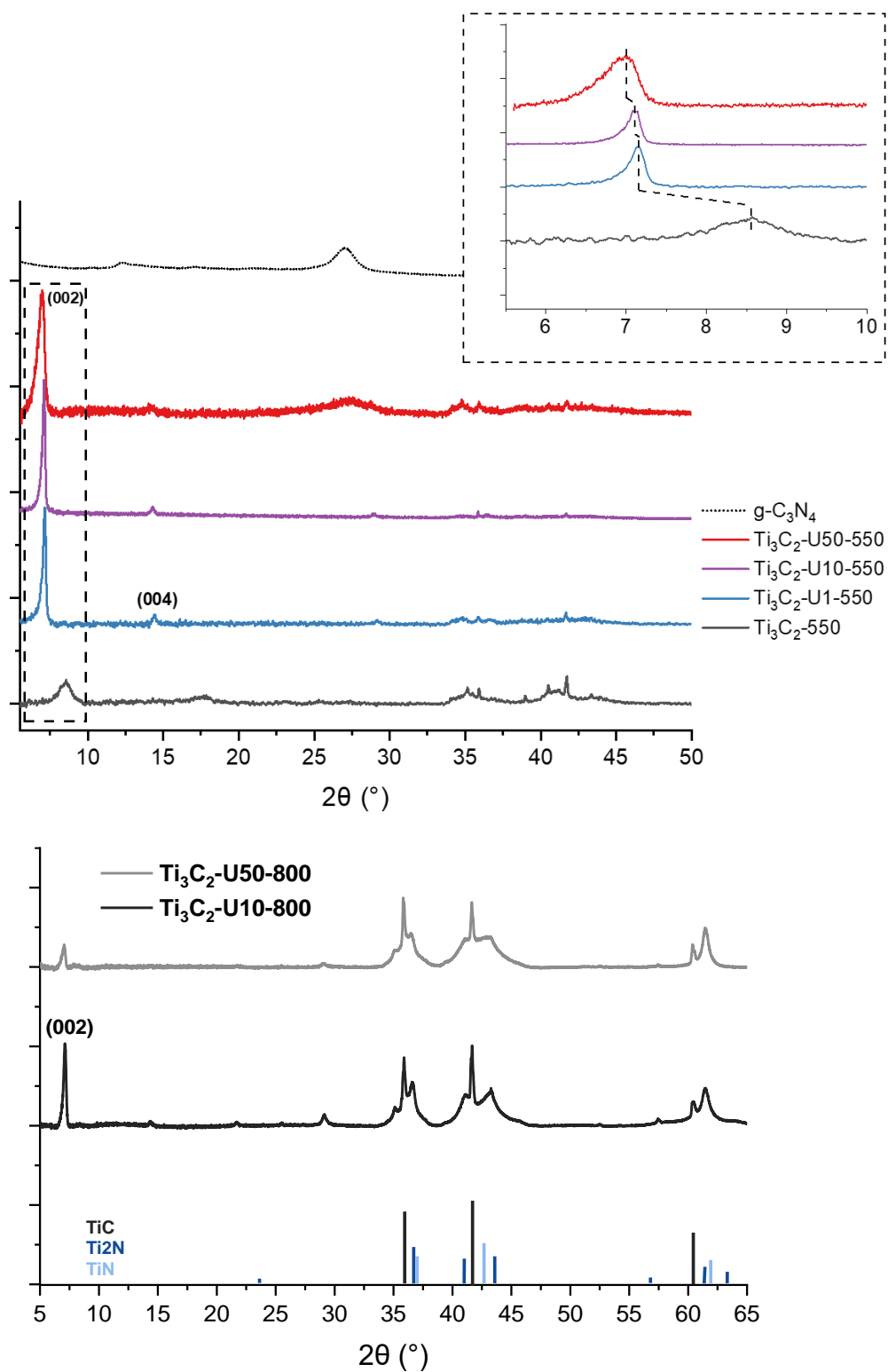
Figure 4.8: XRD pattern of g-C₃N₄, Ti₃C₂-550, Ti₃C₂-U1-550, Ti₃C₂-U10-550 and Ti₃C₂-U50-550 (top) (inset: low angle measurements) and of Ti₃C₂-U10-800 and Ti₃C₂-U50-800 (bottom)

Additional XRD measurements were done to determine the crystalline structure of the samples and if the Ti_3C_2 MXene structure was kept throughout the synthesis steps. The XRD patterns of the different samples are given on Figure 4.8. In addition to the urea-treated samples, an as-synthesized $Ti_3C_2T_x$ sample was also heat treated at 550°C for comparison. The XRD pattern of Ti_3C_2-550 from Figure 4.8 displays the same diffraction peaks than the as-synthesized Ti_3C_2 sample from Figure 4.7 except for a slightly lower intensity of the low angle peak, which shows that no obvious oxidation of the MXene layers into anatase or rutile TiO_2 has taken place during the 550 °C thermal treatment. Indeed, TiO_2 anatase and rutile displays strong diffraction peaks at 25° and 27° respectively, which are not present in the previously mentioned XRD patterns. After thermal treatment at 550°C under argon, all samples still showed the characteristic peaks of Ti_3C_2 showing the MXene structure was maintained. For urea-treated samples, the (00l) peaks were still shifted to lower angles compared to Ti_3C_2. Indeed, the XRD pattern of urea-treated MXenes showed a (002) peak at around 7°, compared to Ti_3C_2-550 which had a (002) peak at 8.56°, while not presenting any XRD peaks related to urea. It shows that a close restacking of the MXene was avoided even after the degradation of urea, most likely due to modification of the surface chemistry and/or decomposition products. From the low-angle XRD measurements (inset in Figure 4.8), it can be seen that the position of the (002) peak also varied depending on the urea content used during the experiments. The peak was positioned at 7.16° 2Θ, 7.11° and 7.0° for Ti_3C_2-U1-550, Ti_3C_2-U10-550 and Ti_3C_2-U50-550 respectively, showing that the interlayer spacing increased with the amount of urea added. In the case of Ti_3C_2-U50-550, the amount of urea added was high enough that a new broad peak appeared in the XRD pattern at around 27.5°, which is a characteristic peak for g-C_3N_4.[125,152] Moreover, no TiO_2 peaks are visible in the XRD pattern, revealing that no Ti oxidation occurred during the 550°C thermal treatment. A peak at around 29° is present for the Ti_3C_2-U1-550, Ti_3C_2-U10-550 and Ti_3C_2-U50-550 samples and are attributed to the (006) peak of Ti_3C_2 MXenes.[153] This peak is not visible for the samples Ti_3C_2-550 due to the lower signal intensity of the XRD pattern and the peak is most likely hidden in the background noise of the measurement.

Another thermal step at 800°C was performed for the samples Ti_3C_2-U10-550 and Ti_3C_2-U50-550 to evaluate the influence of the temperature on the obtained materials, Ti_3C_2-U10-800 and Ti_3C_2-U50-800 respectively. Their XRD patterns displayed the characteristic (002) plane peak at 7.27° for Ti_3C_2-U10-800 and 7.03° for Ti_3C_2-U50-800. However, the relative intensity of the (002) peak is reduced, probably owing to some disorganisation of the MXene structure along the [00l] direction. In addition to this, other peaks can be attributed to TiC, already present in the starting materials as impurities, and titanium nitrides or carbonitrides.[154] The latter peaks are quite broad and are thought to be coming from some titanium which reacted with urea to form nitrides/carbonitrides on the surface of the MXenes. Further discussion concerning the surface

chemistry will be carried out in the next section. The peak at 29° is also present on these two samples.

An EDS analysis was carried out to determine the elemental composition of the different samples. The elemental composition is given in Table 4.1. First, the EDS shows a low amount of Al, confirming the successful etching of the Al layer of Ti_3AlC_2. The Al detected in the samples are mostly due to some unwashed fluoride salts left in the sample or some Al oxides forming, as shown in the SEM picture and EDS of Ti_3C_2-U10-800 in Figure 4.9, where the elemental mapping shows some Al and O aggregations. The slightly higher C composition of the MXene relatively to the MXene stoichiometry can be attributed to carbonaceous impurities (support) or a slight over-etching. For Ti_3C_2-U-550 samples, relatively to Ti, the atomic ratios of O over all the samples increases lightly but does not vary drastically. The C and N proportions in the samples increases with the amount of urea with a substantial jump for Ti_3C_2-U50-550, while the ratios of F and Cl have a decreasing trend overall. Even after the 800°C treatment, there is a slight increase in N proportion relatively to Ti with increasing urea content used during the synthesis, while the increase in C is more noticeable. Moreover, the overall decrease of fluorine ratio with increasing temperature during the thermal treatment is in line with what has been previously reported.[155-157]
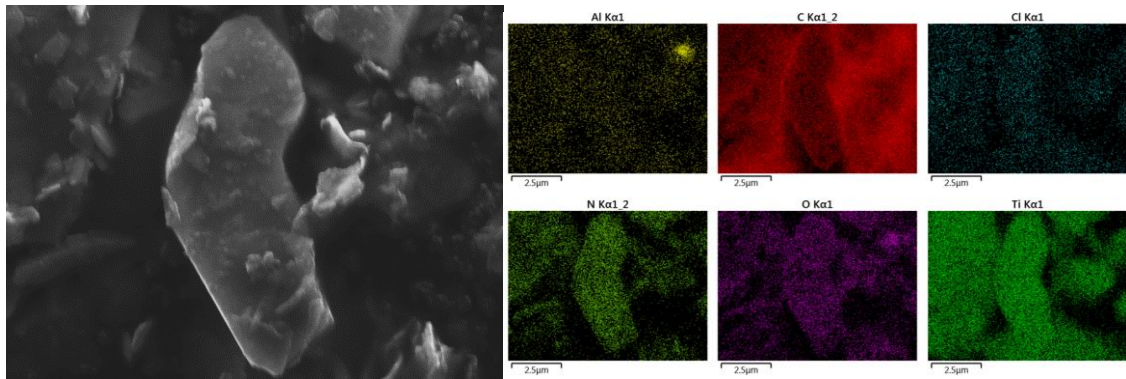
Figure 4.9: SEM picture and EDS illustrating Al impurities in MXene samples (Ti₃C₂-U10-800 sample)

Table 4.1: EDS elemental composition of Ti₃C₂-U and Ti₃C₂-Up samples
[a] averaged over 5 measurements

(at%) [a]	Ti	C	O	N	F	Cl	Al
Ti_3AlC_2	43.9 ± 1.2	35.9 ± 2.3	4.6 ± 0.5	-	-	-	15.6 ± 0.4
Ti_3C_2-550	32.2 ± 1.5	34.8 ± 2.5	23.0 ± 0.8	-	7.2 ± 0.4	2.1 ± 0.1	0.7 ± 0.1
Ti_3C_2-U1-550	29.7 ± 0.9	34.6 ± 1.9	21.3 ± 0.6	6.9 ± 0.3	4.8 ± 0.3	1.2 ± 0.1	1.5 ± 0.5
Ti_3C_2-U10-550	26.5 ± 1.0	35.6 ± 2.1	25.1 ± 1.0	8.0 ± 0.4	2.2 ± 0.1	0.7 ± 0.1	1.9 ± 0.8
Ti_3C_2-U10-800	23.0 ± 0.9	50.3 ± 2.8	19.2 ± 1.0	5.5 ± 0.2	0.6 ± 0.0	1.1 ± 0.2	0.3 ± 0.1
Ti_3C_2-U50-550	5.5 ± 0.7	47.1 ± 2.0	7.4 ± 0.6	40 ± 0.9	-	-	-
Ti_3C_2-U50-800	17.2 ± 0.8	61.1 ± 2.4	13.9 ± 0.7	5.7 ± 0.3	1.2 ± 0.2	0.5 ± 0.0	0.4 ± 0.2

The SEM-EDS elemental mappings of Ti and N for samples Ti_3C_2-U10-550, Ti_3C_2-U10-800, Ti_3C_2-U50-550 and Ti_3C_2-U50-800 are given in Figure 4.10. EDS shows a good dispersion of the nitrogen content throughout the MXene flakes, supporting the successful interaction and intercalation of urea between MXene layers, and the reaction of urea decomposition products with the MXenes during the thermal treatments. It must be noted that the Ti_3C_2-U50-550 EDS nitrogen mapping shows a significant amount of nitrogen species, corresponding to g-C_3N_4 as deduced from the XRD data, which does not interact with MXene flakes. The additional pyrolysis at 800°C has managed to decompose these excess g-C_3N_4 in Ti_3C_2-U50-800, which is also backed up by the previous XRD results.
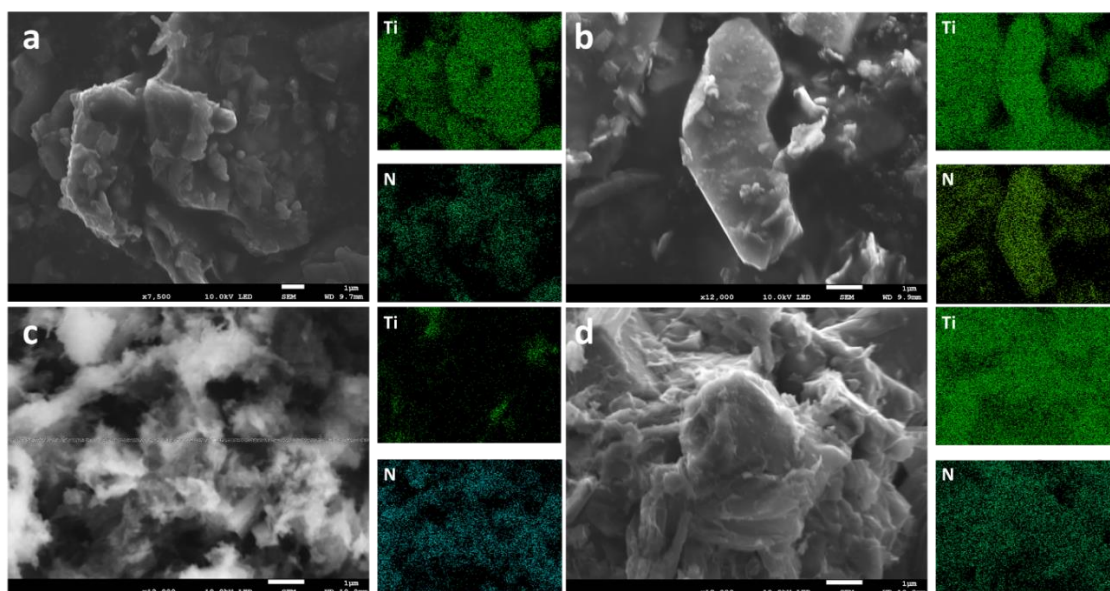
Figure 4.10: SEM-EDS mapping of Ti and N for (a) Ti_3C_2-U10-550, (b) Ti_3C_2-U10-800, (c) Ti_3C_2-U50-550 and (d) Ti_3C_2-U50-800 samples

4.2.2.2. Morphology and surface characterization

As mentioned previously, the surface morphology and chemistry, as well as the porosity and overall surface area of a material is going to be a key to its electrochemical and catalytic properties, as it is going to influence the number of active sites available to participate in an electrochemical reaction. It is therefore important to analyse and understand the chemical environment on the surface of the materials, as well as their morphology.
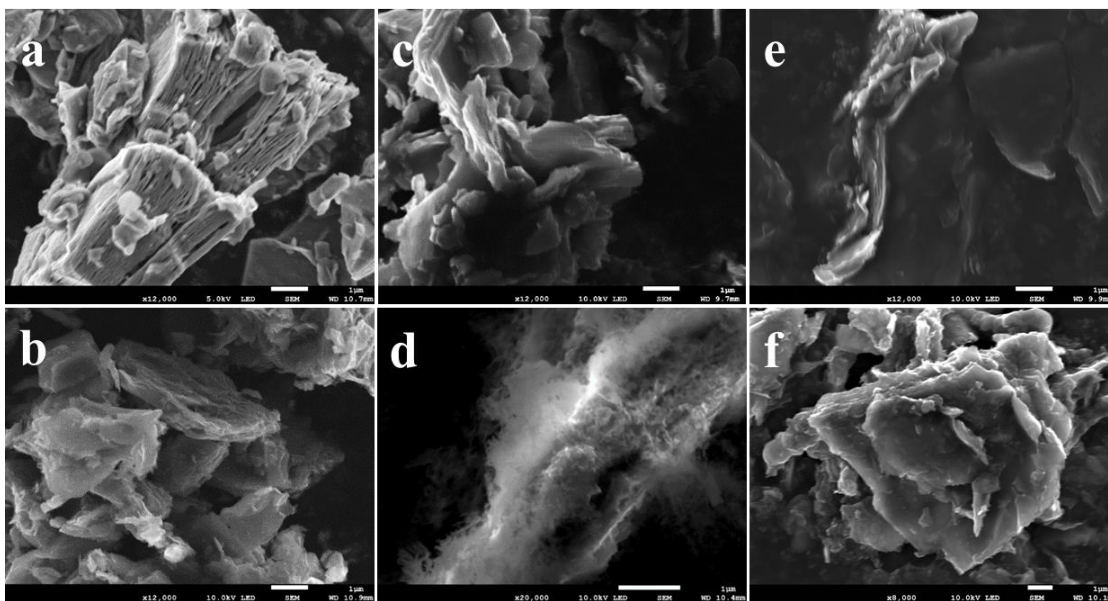
Figure 4.11: SEM pictures of (a) Ti_3C_2-550, (b) Ti_3C_2-U1-550, (c) Ti_3C_2-U10-550, (d) Ti_3C_2-U50-550, (e) Ti_3C_2-U10-800 and (f) Ti_3C_2-U50-800 (scale bar = 1μm)

The morphology of the different samples was determined using scanning electron microscopy (SEM). As discussed earlier, the accordion-like layered structure of Ti_3C_2 is visible for the bare MXene, as shown on Figure 4.11.a. The particles were of sizes ranging from 1 to 10 µm overall and consisted of several exfoliated $Ti_3C_2T_x$ ordered layers with clearly defined gaps. The SEM pictures of urea-treated samples, given on Figure 4.11, all showed a less ordered morphology, while still displaying a two-dimensional, layered structure. It can also be noted that the particles thickness for urea-treated samples is lower than for bare MXene. It shows that a partial delamination of the Ti_3C_2 flakes has occurred during the experimental process, which could have happened during the urea intercalation or during the thermal treatment afterwards from the decomposition of urea trapped between the MXene layers. The fact that the different MXene sheets were not as easily distinguishable for urea-treated samples while having a bigger interlayer spacing (refer to XRD analysis in section 5.2.1.1) compared to bare MXene could be explained by the presence of the urea-decomposition compounds present between the layers and on the surface of the MXene sheets. Moreover, the difference in the surface morphology of the Ti_3C_2-U1-550 and Ti3C2-U10-550 compared to Ti_3C_2 could be due to the MXenes being slightly covered by some of the decomposition products or from having a different surface chemistry after the thermal process, which is going to be discussed later using XPS analysis. Meanwhile, the Ti_3C_2-U50-550 sample ended up completely covered with g-C_3N_4 as shown on the XRD pattern of the samples (Figure 4.8).
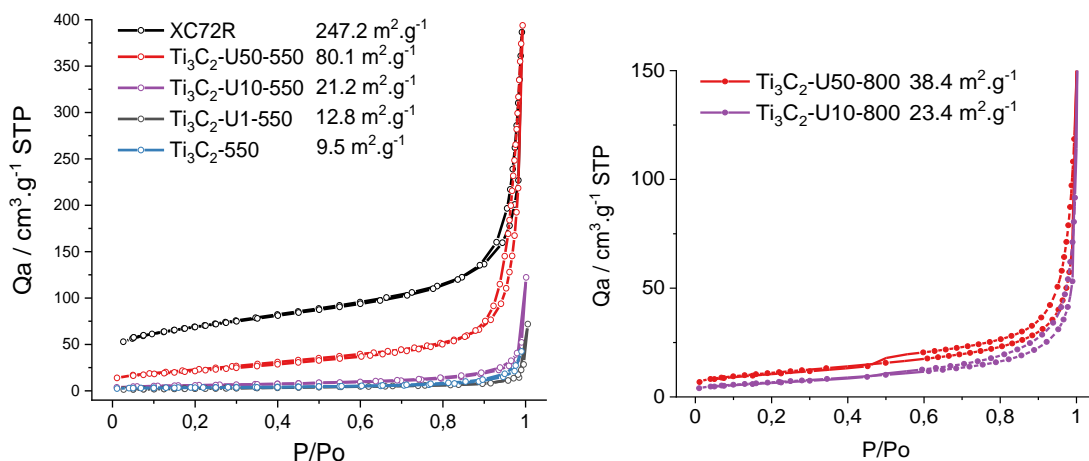
Figure 4.12: Adsorption isotherms from N₂ adsorption-desorption experiments of Ti₃C₂-550, Ti₃C₂-U1-550, Ti₃C₂-U10-550, Ti₃C₂-U50-550 and XC72R (left) and of Ti₃C₂-U10-800 and Ti₃C₂-U50-800 (right). The calculated surface area is given in the legend.

To evaluate the effect of the urea intercalation, as well as the subsequent thermal treatment, on the porosity and surface area of the different samples, N_2 adsorption-desorption experiments were carried out, and the isotherms are presented in Figure 4.12. The BET analysis shows that intrinsically, Ti_3C_2 MXene has a low surface area (9.5 m².g^{-1}) which is in accordance with previous reports, which ranges around 4 – 15 m².g^{-1} depending on the synthesis method.[141,142] The urea-treated samples, in the other hand, show an increase in surface area. The calculated surface areas for Ti_3C_2-U1-550, Ti_3C_2-U10-550 and Ti_3C_2-U50-550 are 12.8 m².g^{-1}, 21.2 m².g^{-1} and 80.1 m².g^{-1} respectively. The increase in surface area can be explained by different factors including the urea decomposition product acting as pillar to avoid the close restacking of MXene layers, as well as the partial delamination during the synthesis, the extra surface area brought by the decomposition products themselves and possible MXene surface morphology modifications. For Ti_3C_2-U50-550, most of the increase in surface area is due to the formation of g-C_3N_4 specific of this sample. Even after the calcination at 800°C, the surface area of Ti_3C_2-U10-800 and Ti_3C_2-U50-800 are still at higher values compared to Ti_3C_2, respectively 23.4 m².g^{-1} and 38.4 m².g^{-1}, which is around twice and thrice the initial surface areas. Although there is a noticeable increase in surface area, these materials are still far from the surface area of XC72R, which is a common catalyst support, and has a measured BET surface area of 247.2 m².g^{-1}. The isotherms for Ti_3C_2-550, Ti_3C_2-U1-550 and Ti_3C_2-U10-550 are type II isotherms, based on IUPAC classification guide,[130] and are characteristic for non-porous or macroporous materials, as reflected by their low surface areas. In comparison, Ti_3C_2-U50-550 isotherm is a type IV isotherm, like XC72-R, characteristic of mesoporous materials. They both have a hysteresis at high p/p° (between 0.9 and 1) of type H3 and is characteristic of non-rigid aggregates of plate-likes particles or when macropores of the materials are not completely filled with pore condensate.[130] After pyrolysis at 800°C, the N_2 adsorption-desorption measurements of Ti_3C_2-U10-800 and Ti_3C_2-U50-800 display an isotherm of type IV, both of them with an hysteresis of type H3.
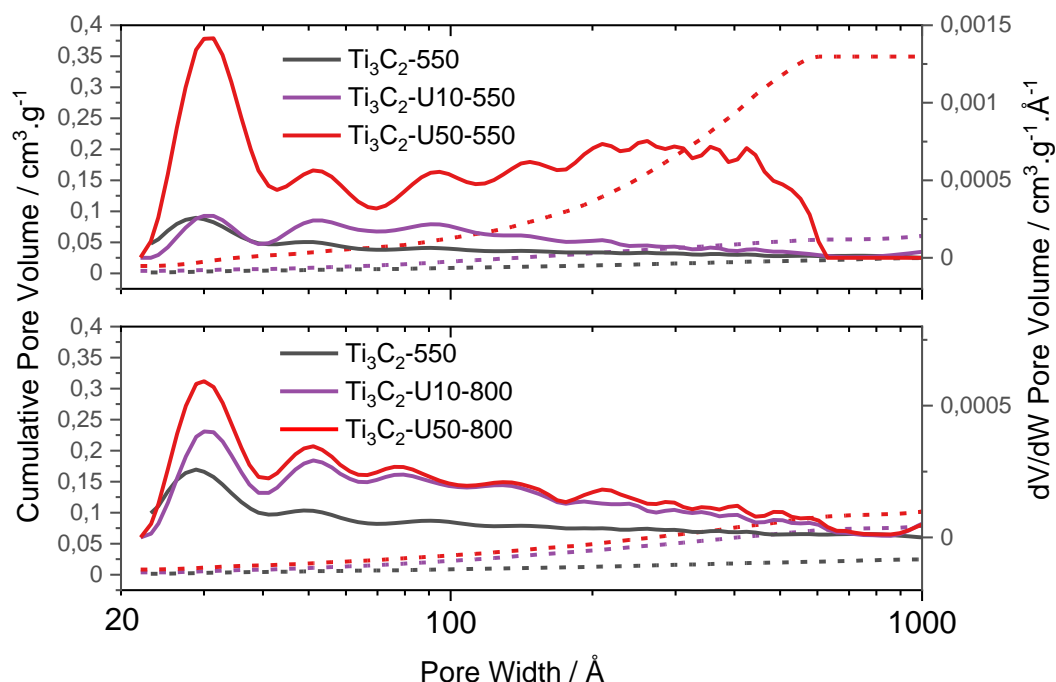
Figure 4.13: Pore size distribution of the different MXenes samples: cumulative pore volume (dotted line) and dV/dW pore volume (solid line)

The pore size distribution of the different samples is given in Figure 4.13. The cumulative pore volume for the MXene reach around 0.025 $cm^3.g^{-1}$, which is very low. The pore width of Ti_3C_2-550 is in the range of 2-10 nm mostly, with the lower peak being centred around 2.8 nm, showing the presence of some mesopores, although most of the porosity is of macroporous nature as shown from the adsorption isotherms of Ti_3C_2. The urea treated samples have a broader pore size distribution, ranging from 2 to 70 nm, with Ti_3C_2-U50-550 showing a bigger proportion of mesopores in the 10-70 nm range compared to other treated samples. The smaller peak is centred around 3.1 nm, which is a slight increase compared to untreated MXene. After the pyrolysis, the Ti_3C_2-U10-800 shows a similar pore width distribution, as well as cumulative pore volume (around 0.07 $cm^3.g^{-1}$), while Ti_3C_2-U50-800 seems to have partially lost its 10-70 nm mesopores, going from 0.35 $cm^3.g^{-1}$ cumulative pore volume to 0.10 $cm^3.g^{-1}$. Based on the fact we previously determined and excess of g-C_3N_4 was synthesized, the porosity lost after pyrolysis for Ti_3C_2-U50-800 can be attributed to the degradation of g-C_3N_4.

A detailed chemical structure of the different samples has also been investigated using X-ray photoelectron spectroscopy (XPS). The deconvolution details are given in appendix A. The full XPS spectra of all samples are available in Figure 4.14. The Ti2p (~ 454 - 466 eV), C1s (~ 280 - 290 eV) and O 1s (~ 528 - 535 eV) peaks are visible on all XPS spectra. In comparison, the N1s peak (~ 395 - 404eV) is only visible on urea-treated samples. The Ti2p spectra for Ti_3C_2-U50-550 is greatly attenuated, due to the high quantity of urea used during the synthesis step, which led to the formation of g-C_3N_4, as discussed earlier. The elemental composition derived from the XPS spectra is given in Table 4.2. As explained in the methods section, XPS is a superficial method of measurement, meaning that the chemical environment described is mostly the one of the atoms close to the surface of the materials, which explains the variations in elemental compositions compared to the one obtained previously from EDS. It is also describing the chemical environment which is going to be relevant to the electrochemical properties of the materials, as it is at the interface between the bulk of the materials and the electrolyte during the electrochemical processes. The ratio of carbon to titanium C/Ti near the surface increases for the Ti_3C_2-Ux-550 samples, showing that the intercalated urea, after decomposition during the thermal treatments, forms some carbonous species on the surface of the MXene flakes.

Table 4.2: Surface elemental composition of Ti_3C_2-Ux-550 and Ti_3C_2-Ux-800 samples from XPS analysis

(at%)	Ti 2p	C 1s (C/Ti)	O 1s	N 1s (N/Ti)	F 1s	Cl 1s
Ti_3C_2-550	16.88	46.43 (2.7)	30.89	-	4.54	1.26
Ti_3C_2-U1-550	11.94	50.72 (4.2)	21.88	13.63 (1.1)	1.84	-
Ti_3C_2-U10-550	14.63	44.06 (3.0)	27.23	12.16 (0.8)	1.92	-
Ti_3C_2-U10-800	14.83	44.55 (3.0)	29.3	8.93 (0.6)	2.39	-
Ti_3C_2-U50-550	0.11	45.56 (414.1)	3.22	45.56 (414.2)	0	-
Ti_3C_2-U50-800	7.75	61.79 (7.97)	15.58	12.75 (1.6)	2.14	-
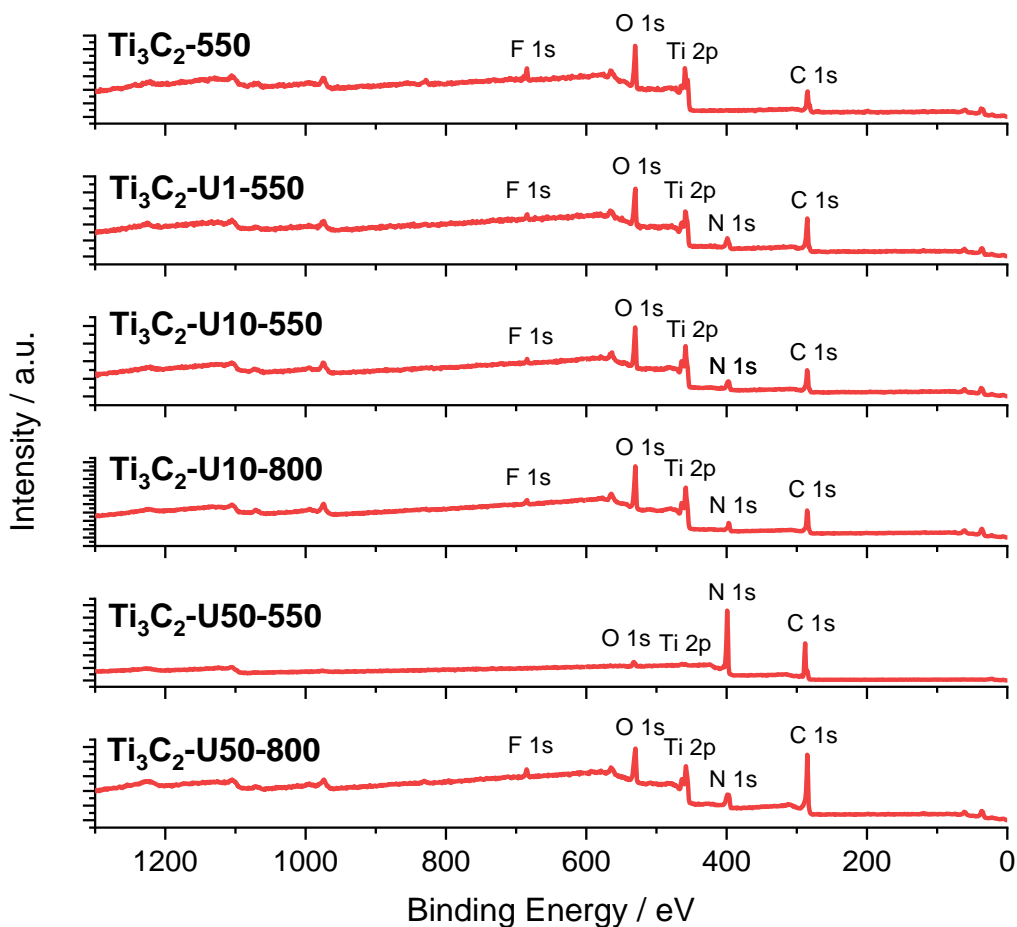
Figure 4.14: Full XPS spectra of Ti₃C₂-550, Ti₃C₂-U1-550, Ti₃C₂-U10-550, Ti₃C₂-U10-800, Ti₃C₂-U50-550 and Ti₃C₂-U50-800

The Ti2p spectra of Ti_3C_2 (Figure 4.15) can be deconvoluted into four doublets (Ti2p$_{3/2}$/Ti2p$_{1/2}$) corresponding to Ti-C (455.1 eV / 460.4 eV), Ti^{2+} (456.2 eV / 461.5 eV), Ti^{3+} (457.5 eV / 462.8 eV) and Ti^{4+} (458.8 eV / 464.5 eV), and is characteristic of Ti_3C_2 MXene.[133] The Ti^{4+} peak is a sign of some surface oxidation occurring during the different experimental steps, especially during the thermal treatment where the surface titanium can be slightly oxidized by –O and –OH surface groups and adsorbed/intercalated water, leading to the formation of some TiO_2 on the surface, although not visible in XRD measurements due to the small amount formed. The Ti^{4+} peak is also present in the Ti2p spectra of the different urea-treated samples. The Ti^{2+} and Ti^{3+} peaks in the MXene sample can be attributed to the different surface groups, such as Ti-OH and Ti-O. The distribution of the different titanium oxidation states for the different samples is given in Table 4.3. The proportions of the different titanium oxidation states vary with the amount of urea used and tend towards an increasing proportion of Ti^{2+} and Ti^{3+} with increasing urea content. These variations of the Ti^{2+} and Ti^{3+} peaks can be attributed to the formation of Ti-N and $Ti-O_xN_y$ bonds during the thermal treatment and are accordance with the literature about N-doped titanium species.[158-160]. These observations are also confirmed by the N1s XPS spectra presented in Figure

4.17. For the two samples pyrolyzed at 800°C, the titanium carbonitride species that have been formed on the MXene surface also contribute to the Ti^{2+} and Ti^{3+} XPS peaks.

The C1s XPS (Figure 4.15) spectrum of Ti_3C_2 can be fitted into four components located at 281.81 eV, 284.76 eV, 286.25 eV and 288.76 eV. They correspond to C-Ti, C-C, C-O and O-C=O/C-F bonds, respectively.[133,161,162] The C-Ti peak intensity decreases for urea-treated samples Ti_3C_2-U1 and Ti_3C_2-U10, and completely disappears for Ti_3C_2-U50, due to the amount of urea degradation products on the surface of the MXene flakes as mentioned earlier. Moreover, a new peak appears for urea-treated samples at around 288.22 eV corresponding to N=C-N bound, which is also a characteristic peak of the C1s XPS spectrum of g-C_3N_4[152], explaining why this peak is significantly higher for the Ti_3C_2-U50 sample. For the other samples, as g-C_3N_4 doesn't seem to be present in the XRD pattern, the N-C=N peak may be due to some N-C species forming on the surface of the samples or due to some nitrogen being introduced in superficial C layers of the MXene during the thermal process.
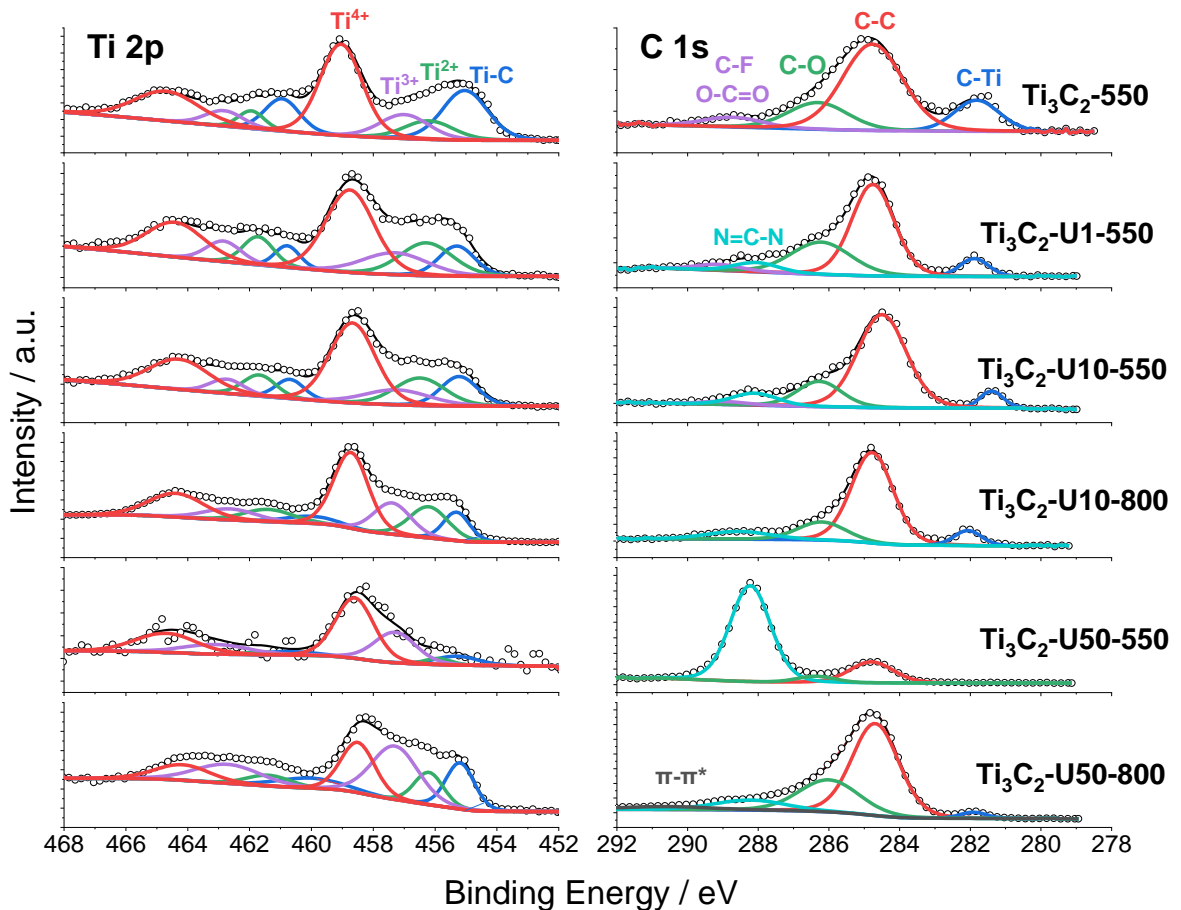
Figure 4.15: Ti2p (left) and C1s (right) XPS spectra of Ti₃C₂-550, Ti₃C₂-U1-550, Ti₃C₂-U10-550, Ti₃C₂-U10-800, Ti₃C₂-U50-550 and Ti₃C₂-U50-800

Table 4.3: Ti2p XPS peak fitting distribution (more details in appendix A)

	Ti-C	Ti^{2+}	Ti^{3+}	Ti^{4+}
B.E (eV)	**455.1**	**456.2**	**457.5**	**458.8**
(at%)	**(460.4)**	**(461.5)**	**(462.8)**	**(464.5)**
Ti$_3$C$_2$-550	27.46	11.08	14.38	47.08
Ti$_3$C$_2$-U1-550	13.1	20.92	17.43	47.55
Ti$_3$C$_2$-U10-550	15.39	19.59	13.84	51.18
Ti$_3$C$_2$-U10-800	12.97	20.97	20.20	45.85
Ti$_3$C$_2$-U50-550	8.96	1.48	30.79	58.77
Ti$_3$C$_2$-U50-800	18.24	29.22	34.70	17.85

The O1s spectra for Ti$_3$C$_2$ (Figure 4.16) can be deconvoluted into three peaks for all samples at 530.1 eV, 531.1 eV and 532.2 eV. The peak at 530.1 eV corresponds to oxygen bounded to titanium in TiO$_2$ materials, while the peaks at 531.1 eV and 532.2 eV corresponds to -O and -OH surface groups respectively, as described in previous MXene studies.[133] These three peaks are still present in the other samples. Overall, a slight increase in proportion of the 531.1 eV and 532.2 eV compared to the peak at 530.1 eV can be noted for the urea samples treated at 550 °C, especially the peak at 532.2 eV for Ti$_3$C$_2$-U50. The proportions of these two peaks decreases after the additional 800 °C pyrolysis compared to their 550 °C counterparts, showing a partial degradation of oxygen surface species. The oxygen species from the 531.1 eV and 532.2 eV for the urea treated samples can be related to Ti$_3$C$_2$ surface groups (-O and -OH) or oxygen surface groups on carbons[163] (>C=O and C-OH) or g-C$_3$N$_4$.[164]

The F1s spectrum (Figure 4.16) for Ti$_3$C$_2$ shows two different peaks: one at 684.56 eV corresponding to the surface fluorine bonds at the surface of the MXene after the etching, the other peak at 688.01 eV corresponds to some fluorine impurities left over after the etching process. The intercalation of urea followed by the thermal treatment at 550°C influences slightly the binding energy of C-Ti-F peak, shifting it towards lower binding energy with increasing urea content. It must be noted that the F1s spectrum for Ti$_3$C$_2$-U50 does not show any signal due to the excess of g-C$_3$N$_4$ contained in the sample. The annealed samples at 800°C both show a shift of the main F1s peak towards greater binding energy (685.10 ± 0.5 eV) compared to Ti$_3$C$_2$ showing a slightly different chemical environment on the surface for these two samples, which still remains to be explained.
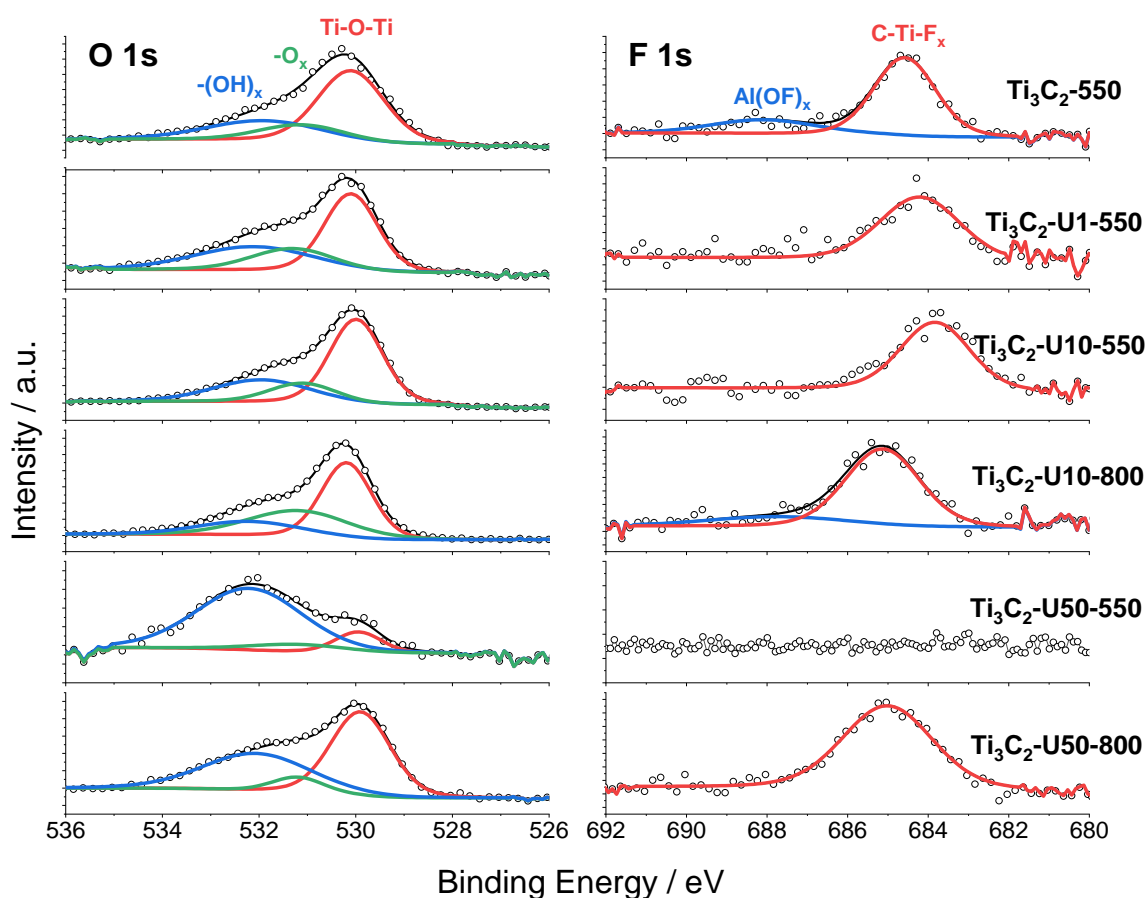
Figure 4.16: O1s (left) and F1s (right) XPS spectra of Ti₃C₂, Ti₃C₂-U1, Ti₃C₂-U10, Ti₃C₂-U10p, Ti₃C₂-U50 and Ti₃C₂-U50p

The N1s spectra of the urea-treated samples are given in Figure 4.17. A peak at 396.3 eV, corresponding to N-Ti bounds, is visible for the urea-treated samples, except for Ti_3C_2-U50, which is easily explained by the excess of urea used, causing the formation of excess g-C_3N_4 covering all the sample and does not interact with the MXene, causing most of other nitrogen species that would be interacting with the MXene from showing on the XPS spectra. The pyrolysis step at 800 °C, which leads to the carbonization and degradation of the excess of g-C_3N_4, leads to the re-apparition of the N-Ti peak for the Ti_3C_2-U50p sample. This claim is also supported by the fact that the N1s spectrum for Ti_3C_2-U50 is characteristic of g-C_3N_4 which can be deconvoluted into three peaks at 398.59, 399.73 and 401.40 eV corresponding at C-N=C, N-(C)$_3$ (bridge) / H-N-(C)$_2$ and graphitic nitrogen respectively.[124,125,165-167] The distribution of the different nitrogen species is given in Table 4.4 and is quite complex due to the variety of materials involved in the synthesis. The literature concerning Ti_3CN MXene synthesis and/or nitrogen doping of Ti_3C_2 diverge slightly concerning the exact peak assignments, but they generally agree that the N-Ti peak at around 396.4 eV, and to some extent the peak at around 400.2 eV shows a successful

nitrogen doping of the MXene through lattice replacement in the carbon layer.[158,168-170] Another factor needs to be taken into consideration forthe peak at 396.4 eV. As seen in the XRD pattern in Figure 4.8, the samples pyrolyzed at 800 °C contain some titanium nitride phases, which would also show up on the XPS at around 396-397 eV for these two samples. The peak at 398.7 eV correspond to pyridinic N and are most likely due to urea decomposition compounds forming on the surface of the MXenes, which explains the decrease from 53.87 to 27.36 at% and from 63.03 to 39.75 at% after the 800 °C pyrolysis for Ti_3C_2-U10p and Ti_3C_2-U50p samples respectively. The peak at 400.2 eV for the samples other than Ti_3C_2-U50 most likely corresponds to pyrrolic species from the decomposition products or nitrogen surface groups on MXenes[169]. A small peak at around 401.4 eV can be assigned to graphitic nitrogen of surface carbonous species.
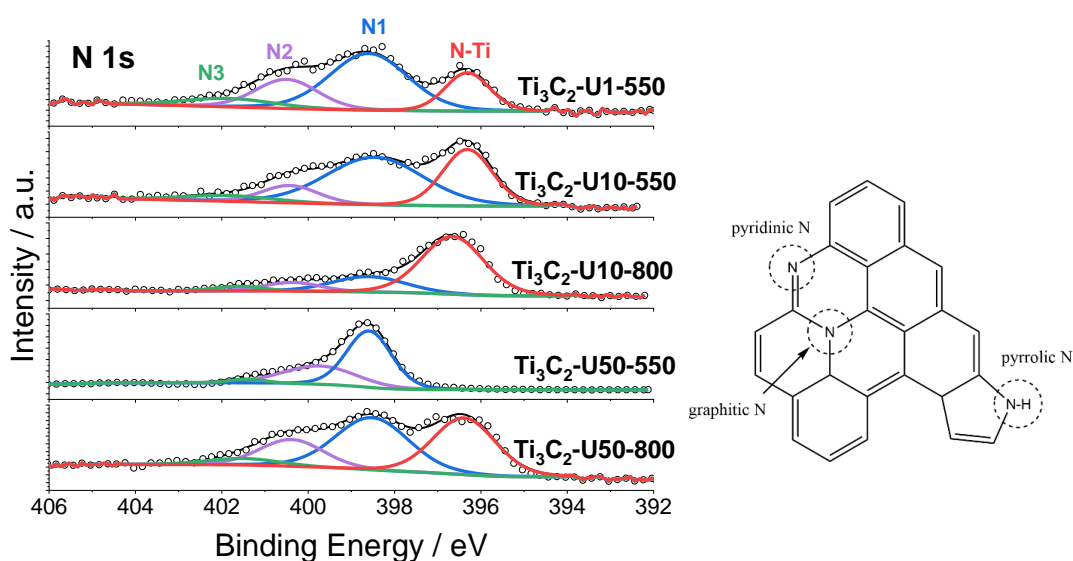
Figure 4.17: : N1s XPS spectra of Ti_3C_2-U1, Ti_3C_2-U10, Ti_3C_2-U10p, Ti_3C_2-U50 and Ti_3C_2-U50p (left) and schematic of N species in carbon materials (right)

Table 4.4: N1s XPS peak fitting distribution (more details in appendix A)

	N-Ti	N1	N2	N3
B.E (eV) **(at%)**	396.4	398.7	400.	401.4
Ti_3C_2-550	-	-	-	-
Ti_3C_2-U1-550	20.60	52.46	19.53	7.41
Ti_3C_2-U10-550	34.92	53.87	8.74	2.47
Ti_3C_2-U10-800	63.12	27.36	5.80	3.71
Ti_3C_2-U50-550	-	63.02	33.48	3.51
Ti_3C_2-U50-800	37.01	39.75	18.96	4.28

4.3. Conclusion

In conclusion, the synthesis and characterization of Ti_3C_2, as well as N-C on N-doped Ti_3C_2 has been reported. After determining the best chemical to intercalate between the MXene layers to be used as nitrogen precursor, MXene samples have been intercalated with different amount of urea before going through a thermal treatment. It has been shown that urea intercalates readily between MXene layers allowing for a more homogenous intercalation for the MXene samples mixed with urea. Moreover, the introduction of urea has permitted an increase in interlayer spacing for the intercalated MXenes. It has been demonstrated to be the case even after the different thermal treatments at 550°C and 800°C, based on XRD measurements where the (002) MXene peak has been measured at around 7° 2θ for all urea-treated samples, while this peak is at 8.56° for Ti_3C_2-550. This has mainly been attributed to the presence of some urea-decomposition compounds on the surface of MXene layers, serving as pillars inhibiting the MXene layer restacking during the thermal treatment. This has led to an increase of the surface area of the different urea treated MXenes, to values of 12.8, 21.2 and 80.1 $m^2.g^{-1}$ for Ti_3C_2-U1-550, Ti_3C_2-U10-550 and Ti_3C_2-U50-550 respectively, from 9.5 $m^2.g^{-1}$ for Ti_3C_2-550, although most of the SSA measured for Ti_3C_2-U50-550 is coming from excess g-C_3N_4 formed during synthesis. But even for the samples treated at 800°C, which decomposed the excess g-C_3N_4, the MXene samples Ti_3C_2-U10-800 and Ti_3C_2-U50-800, have improved SSA values of 23.4 and 38.4 $m^2.g^{-1}$ respectively.

Based on XRD and SEM pictures of the samples, the MXene structure has been kept throughout the different synthesis steps, even for the samples treated at 800°C, although partial degradation may have happened for the samples treated at this temperature, forming some titanium carbide and titanium nitrides species. The chemical analysis, EDS and XPS, show a homogenous distribution of nitrogen throughout the samples, as well as the successful doping of the Ti_3C_2, where peaks present on Ti2p and N1s have been reported to support the successful nitrogen doping of Ti_3C_2 structures. Moreover, C1s and N1s XPS spectra of the samples support the fact that N-containing carbonous species have formed on the surface of the MXenes.

CHAPTER 5: Evaluation of N-Carbon on N-Ti$_3$C$_2$ for Oxygen Reduction Reaction

5.1. Introduction

MXenes face several shortcomings when it comes to electrochemical applications. First, MXenes have a small surface area compared to commonly used electrode materials, which usually are made of high surface area support materials decorated/functionalized with electroactive species. Although not directly correlated, a higher specific surface area means there will potentially be a higher number of electrochemical sites available for electrochemical species to adsorb on for electrochemical reactions, therefore improving the electrochemical properties of the materials. A high SSA is also important when trying to decorate a support material with a catalyst, as a bigger SSA means there will be more surface available for the catalyst to grow or be deposited on the support. It usually translates to a better dispersion of the catalyst particles on the support and smaller particle sizes during the synthesis. It also usually slows down the aggregation and degradation of the catalyst particles, especially if there is a strong interaction between the support material and the catalyst particles.

Moreover, although Ti$_3$C$_2$ has shown to have some activity towards ORR in alkaline media, especially once it has been delaminated into single layers,[101] it is still far from conventional AFC ORR catalysts. Therefore, in the previous chapter, a method to intercalate and functionalize the MXene has been successfully developed to synthesize N-Carbon species on N-doped Ti$_3$C$_2$ layers surface, with the carbon species on top of the MXene flakes also acting as pillars, which stopped the restacking of the MXene layers during the thermal treatment and ended up increasing the surface area of our materials.

Now that the physico-chemical properties of the different materials have been measured and analysed, it is necessary to evaluate their electrochemical properties. The main focus of this chapter is to evaluate the activity of the materials synthesised previously towards ORR in alkaline media and try to connect them with their physico-chemical properties.

5.2. Results and discussion

The ORR properties of the samples were investigated using RDE measurements in aerated 0.1M KOH electrolyte. The different urea-treated MXene were tested and compared to bare Ti_3C_2-550 and commercial XC72-R, which is a common carbon support for catalyst materials in electrochemistry, due to its conductivity and reasonable specific surface area (SSA), as well as 20% Pt/C which is the benchmark catalyst when it comes to testing ORR activity.

5.2.1. Linear sweep voltammetry of Ti_3C_2-U-X samples

Linear sweep voltammetry (LSV) has been performed on the different samples to determine their electrochemical properties, such as onset potential (E_{onset}), half-wave potential ($E_{1/2}$), and the diffusion-limiting current density (j_L). LSV curves of the different samples were measured in the [0.1;1.1] V (vs RHE) potential range in 0.1 M KOH purged with air and are displayed on Figure 5.1. All the LSVs have been iR and background corrected, as specified in the method section. The current has also been normalized to the geometrical surface area of the working electrode (0.247 cm^2).

The bare MXene sample Ti_3C_2-550 displays the highest overpotential (lowest E_{onset}) towards ORR and the lowest diffusion-limiting current of all samples, showing its overall poor ORR activity. For the urea-treated samples Ti_3C_2-U1-550, Ti_3C_2-U10-550 and Ti_3C_2-U50-550, the overpotential first decreased with increasing urea amount added during the protocol, with an E_{onset} going from 0.72 V (Ti_3C_2-550) to 0.76 V and 0.78 V for Ti_3C_2-U1-550 an Ti_3C_2-U10-550 respectively, but then the overpotential for Ti_3C_2-U50-550 has increased comparatively to Ti_3C_2-U10-550, with an E_{onset} of 0.76 V. A similar trend is displayed by the diffusion-limiting current density (j_L), The improved electrochemical properties can be explained by the change in surface chemistry of the samples, which are covered with urea decomposition products and varying surface groups, increasing the number of active sites, while having close interactions with the MXene support. This is supported by the previously discussed physicochemical results, where the Ti2p XPS peaks show changes in Ti states after being thermally treated with urea (Ti_3C_2-U1-550 and Ti_3C_2-U10-550) compared to the reference sample Ti_3C_2-550). Moreover, this result seems to be in accordance with other studies, where an increase in ORR performance have been demonstrated when using a free-standing g-C_3N_4/Ti_3C_2 composite[171] or g-C_3N_4 decorated with Ti_3C_2 nanoparticles[123] as electrocatalysts. The decrease of E_{onset} between Ti_3C_2-U10-550 and Ti_3C_2-U50-550 can be explained by excess g-C_3N_4 forming around the MXene flakes that do not directly interact with them and are hindering oxygen reduction, as well as decreasing overall electron conductivity, leading to a worse overall performance for the material. Moreover, the LSV behaviour for Ti_3C_2-U50-550 is very similar to what have been reported for g-C_3N_4 when tested

for ORR.[172] It displays a typical 2-step pathway through two reduction waves with onset potentials at around 0.76 V and 0.39 V (vs RHE).

For the samples annealed at 800°C, Ti_3C_2-U10-800 and Ti_3C_2-U50-800, a greater onset potential has been measured compared to their counterparts which have only gone through a 550°C thermal treatment. The onset potentials measured for these two samples are 0.82 V and 0.88 V respectively.

The Figure 5.1 (b) shows a direct comparison between the Ti_3C_2-U10-800, Ti_3C_2-U50-800, XC72-R and Pt/C LSV curves in aerated 0.1M KOH electrolyte at 1600 rpm. The LSV curve profile of Ti_3C_2-U10-800 is very similar to the one for XC72-R, while Ti_3C_2-U50-800 shows a smaller overpotential toward ORR. The XC72-R LSV curve is characteristic and has already been investigated in the literature,[173] it has an E_{onset} around 0.8 V vs RHE and displays two reduction waves: the first one corresponding to the oxygen reduction via a 2-electron pathway (Eq. 5.1) and the second one corresponding to the further reduction of the HO_2^- intermediate species (Eq. 5.2). HO_2^- species formation during electrochemical testing and the different mechanisms involved are going to be further investigated and discussed later on through RRDE measurements.

$$O_2 + H_2O + 2e^- \rightleftharpoons HO_2^- + OH^-$$ *Eq. 5.1*

$$HO_2^- + H_2O + 2e^- \rightleftharpoons 3OH^-$$ *Eq. 5.2*
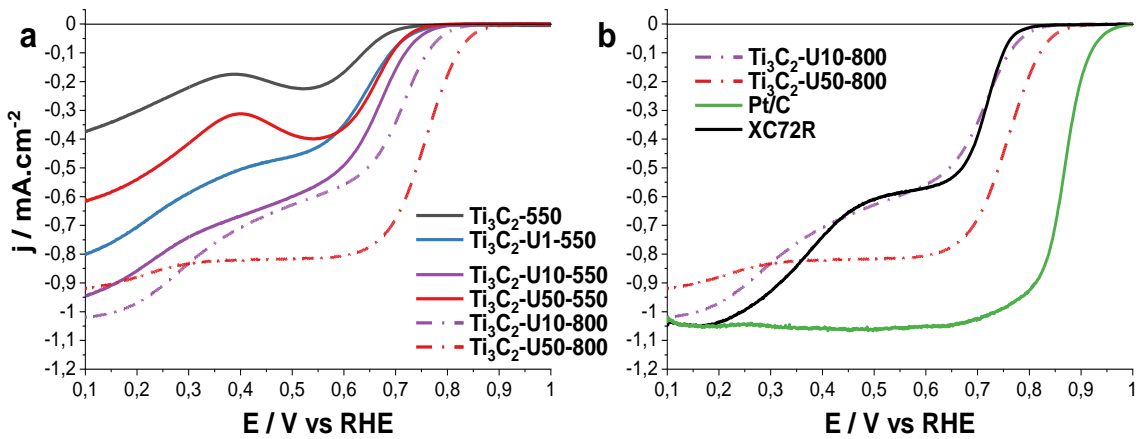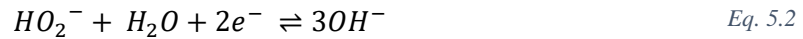
Figure 5.1: (a) LSVs (5 mV.s^{-1}) of the different Ti$_3$C$_2$ samples in 0.1M aerated KOH electrolyte (corrected) at 1600 rpm, (b) Comparison of pyrolyzed Ti$_3$C$_2$-Ux-800 samples with XC72-R and Pt/C

5.2.2. Rotating Ring-Disk Electrode measurements

To better understand the oxygen reduction processes involved with the different samples, RRDE measurements were investigated and presented in Figure 5.2 and Figure 5.3. The ring potential was held at 1.3 V vs RHE during oxygen reduction experiments to detect HO_2^- by-products formed during ORR processes happening on the catalysts when a 2-electrons ORR pathway is

involved. Therefore, RRDE will give us more insight on the ORR mechanisms involved during the electrochemical measurements of the different samples. First, the corrected disk and ring currents measured at 1600 rpm in 0.1 M aerated KOH were measured, then the electron transfer number n and the HO_2^- yield can be determined from the disk and ring current measurements and have been calculated using the following equations, as described in the method chapter.

$$n = \frac{4I_d N}{I_d N + I_r}$$

$$\%H_2O_2 = 100\frac{2I_r N}{I_d N + I_r}$$

First, having a look at the bare MXene sample RRDE response is going to be useful to understand the influence of the urea-intercalation and thermal treatment done on the other catalysts. The RRDE measurements of Ti_3C_2-550 is given in Figure 5.2, the ring-response current density j_{ring} for Ti_3C_2-550 varies following the same trend as the disk current density j_{disk} curve and increases synchronically for both reduction waves. This suggests that the ORR on Ti_3C_2-550 is happening mostly through a 2-electron pathway, which supports the previous observations. However, the calculated *n* is around 3.2 in the [0.3;0.7] V vs RHE potential window, which means that there is a mixed process where some of the peroxide is further reduced to OH⁻ or there could be partial disproportionation of HO_2^-, which would lead to a lower ring current, and a higher apparent *n* calculated from RRDE. For the samples Ti_3C_2-U1-550 and Ti_3C_2-U10-550, j_{ring} has a completely different behaviour compared to the bare MXene, during the first reduction wave, the ring current increases, showing that a 2-electron process is involved. However, during the second reduction process, while j_{disk} increases, j_{ring} decreases, hinting towards the further reduction of HO_2^- into OH⁻ following the reaction given by Eq. 5.2. This explains why the calculated HO_2^- yield decreases, while the apparent n increases, with increasing applied overpotential.

These results show that the urea intercalation followed by thermal treatment led to improved electrochemical properties towards ORR through a modification of the surface chemistries of the samples, which assisted the further oxidation of the HO_2^- ions on the surface of the materials compared to the sample in which urea was not used, Ti_3C_2-550. The surface chemistry of the samples has been characterized previously, especially through XPS measurements, and the improvement in electrochemical properties of the sample could be explained by an increase of active sites thanks to the presence of N-C compounds interaction with the MXene surface. Indeed, N-doped carbon species have widely been reported as having good activity towards ORR, especially in alkaline media. Based on the previous XPS results, we have shown that some N-C decomposition species have deposited on the MXene surface to form mostly pyridinic N species, which is known to be an active site for ORR.

Ti_3C_2-U50-550 displays the highest j_{ring}, with a peroxide yield reaching about 40%. The electron transfer number calculated for this sample using RRDE is around 3 over the potential range of the measurements. Although the urea treatment has improved the ORR performance of the samples when a ratio of 1:1 and 1:10 of Ti_3C_2 to urea by weight, further increase seems to impede the ORR processes. As discussed during the previous Chapter 4, it is mostly likely due to the excess g-C_3N_4 that has been produced during the thermal treatment at 550 °C of the sample Ti_3C_2-U50-550.
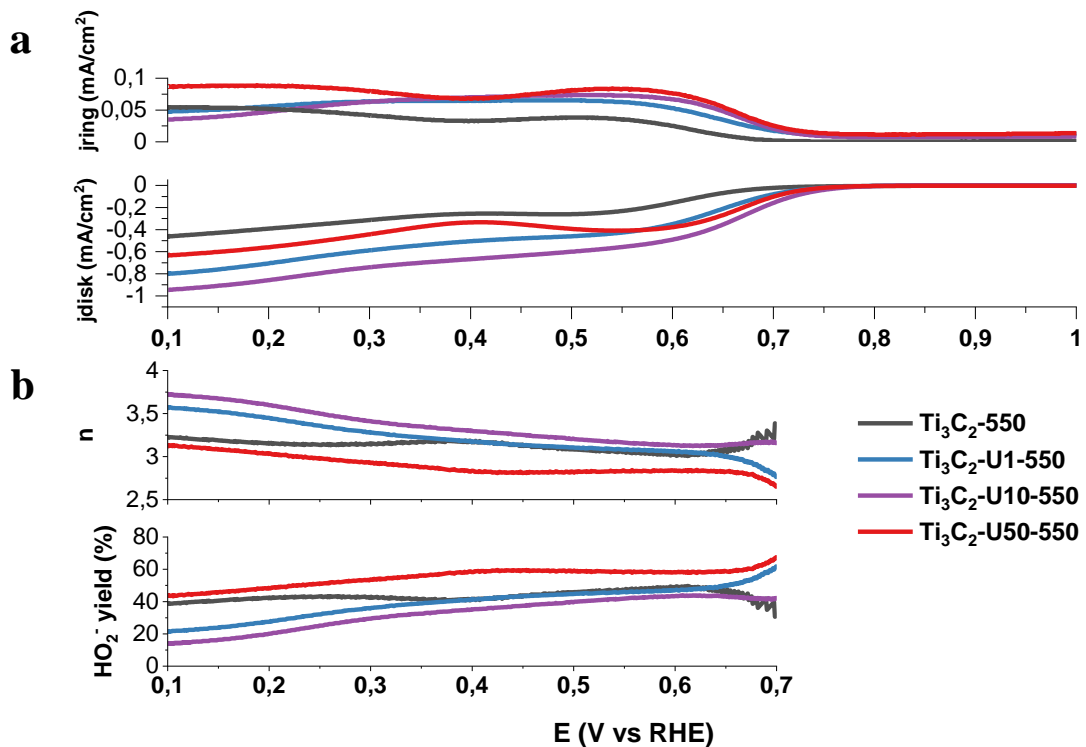
Figure 5.2: RRDE measurements of the different Ti_3C_2-Ux-550 samples in 0.1M aerated KOH electrolyte (corrected) at 1600 rpm: (a) j_{disk} and j_{ring} , (b) calculated HO_2^- yield and electron-transfer number

The RRDE measurements results for the samples which underwent the extra thermal step at 800 °C Ti_3C_2-U10-800 and Ti_3C_2-U50-800 are given in Figure 5.3, and compared to XC72-R and Pt/C. The RRDE results of the Pt/C benchmark is as expected. The ring current density j_{ring} increases just slightly with increasing overpotential and barely any HO_2^- is produced. The electron transfer number calculated for Pt/C is near around 3.9 in average over the potential range, meaning that Pt/C catalyses ORR through a near 4-electron pathway. On the other hand, the ring response of XC72-R supports the previous observations. Indeed, j_{ring} starts increasing significantly throughout the first reduction wave of the LSV, and then decreases slowly at lower potentials.

This is in agreement with the fact that XC72-R reduces oxygen through a two-step process, where O_2 is first reduced to peroxide and then peroxide can be further reduced to OH^-.

The RRDE measurements of Ti_3C_2-U10-800 and Ti_3C_2-U50-800 shows that the ORR occurs with slightly different mechanisms between this samples. Ti_3C_2-U10-800 seems to catalyse the ORR in a similar fashion than XC72-R, where an increase of j_{ring} is noticeable with increasing overpotential, until around 0.4 V vs RHE, it starts decreasing. The apparent electron transfer number for Ti_3C_2-U10-800 increases slowly from about 3.2 at 0.8 V vs RHE up to 3.8 at 0.1 V vs RHE, where a 2+2 electron ORR is taking place. On the other hand, for Ti_3C_2-U50-800, j_{ring} slowly increases with decreasing potential, leading to a stable 20% H_2O^- yield between 0.1 and 0.8 V vs RHE, and an apparent electron transfer number of 3.5.
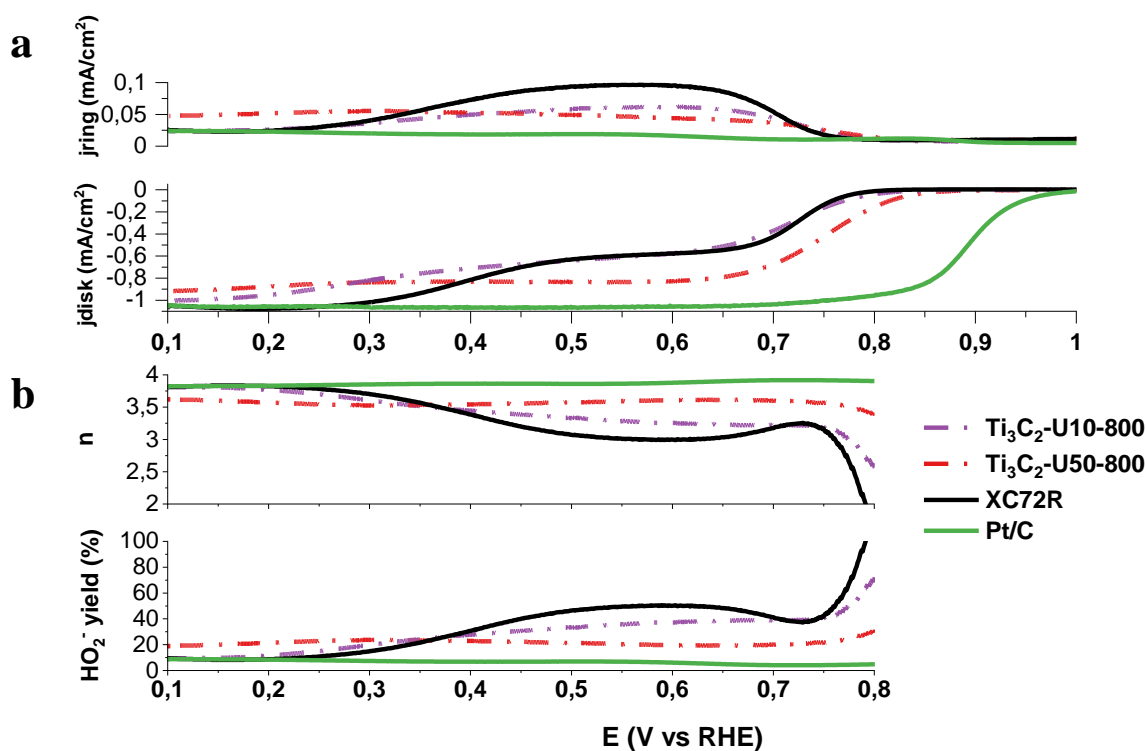
Figure 5.3: RRDE measurements of the different Ti_3C_2-Ux-800 samples, XC72R and Pt/C in 0.1M aerated KOH electrolyte (corrected) at 1600 rpm: (a) j_{disk} and j_{ring} , (b) calculated HO_2^- yield and electron-transfer number

5.2.3. Stability testing

Stability of a catalyst is a very important parameter to test, as it will determine how quickly the catalyst will degrade and therefore its lifetime. Stability and degradation studies are usually done

by comparing the catalyst performance before and after cycling. Cycling of the materials is done through an ADT (Accelerated Durability Test).

The stability of the different samples was then evaluated. To do so, the different electrodes were cycled between [0.5;1] V (vs RHE) for 2000 cycles at 50 mV.s^{-1}, then LSV measurements were done on the cycled materials and compared to the initial LSV curves. The pre- and post-LSVs comparison of the different samples is given in Figure 5.4. The $E_{1/2}$ measurements for the different samples before and after cycling are summarized in Table 5.1.
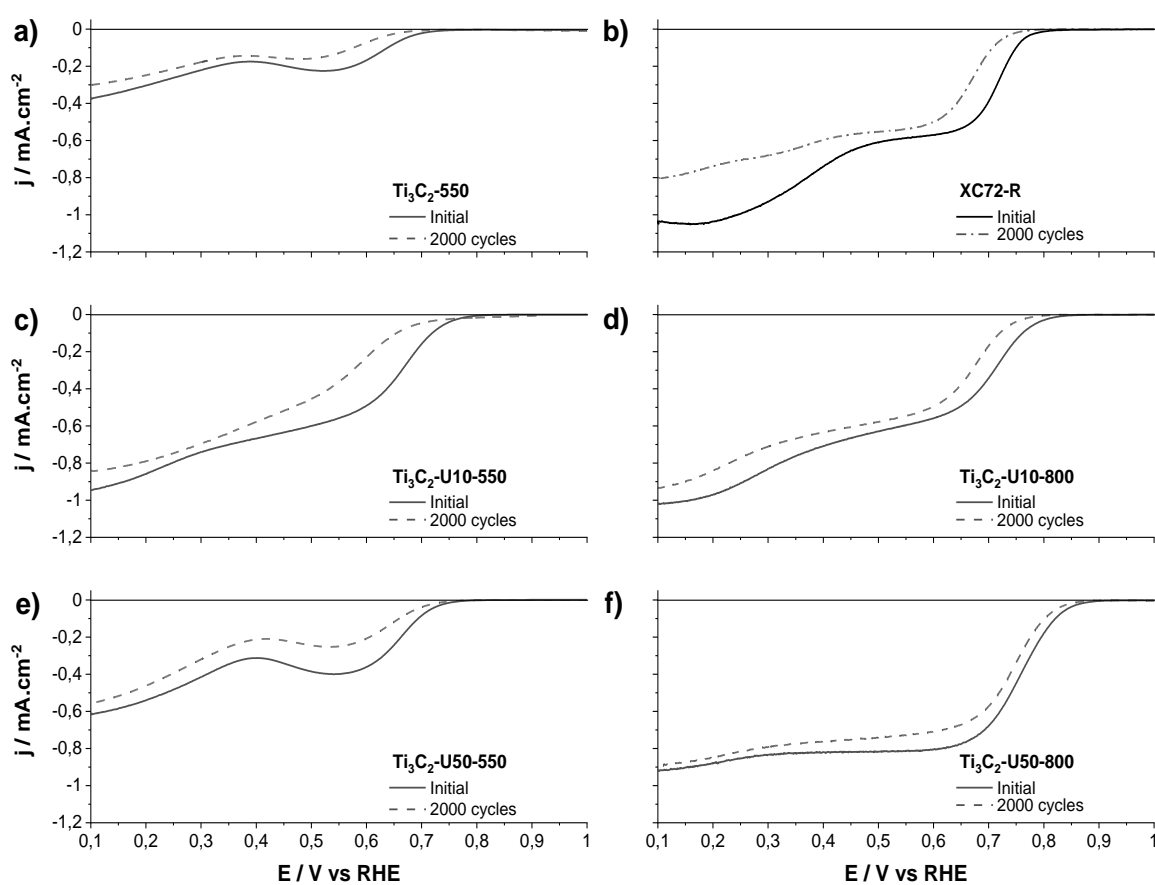
Figure 5.4: LSVs (5 mV.s^{-1}) at 1600 rpm before and after cycling between [0.5;1] V (vs RHE) of the different support materials: (a) Ti$_3$C$_2$-550, (b) XC72-R, (c) Ti$_3$C$_2$-U10-550, (d) Ti$_3$C$_2$-U10-800, (e) Ti$_3$C$_2$-U50-550, (f) Ti$_3$C$_2$-U50-800. The electrolyte used is a 0.1M aerated KOH solution.

The half-wave potentials $E_{1/2}$ of all samples has been shifted to lower potential value, indicating degradation of the materials, and poorer ORR performance. The extent of the shift gives some indication about the degradation, the lower the shift the more stable the materials. Untreated

94

MXene, Ti_3C_2-550, on top of having pretty poor ORR performance, also has some stability issues, which a shift of 80 mV after 2000 cycles. Overall, the stability of the samples treated at 550 °C are the worse of the materials synthesized, with a $\Delta E_{1/2}$ of 110 and 70 mV for Ti_3C_2-U10-550 and Ti_3C_2-U50-550 respectively. On the other hand, it seems that the thermal step at 800 °C has helped improve the electrochemical stability of the materials. The LSVs of the samples Ti_3C_2-U10-800 and Ti_3C_2-U50-800 do not shift as much as the previous samples, with a $\Delta E_{1/2}$ of 40 and 10 mV. Thus, the thermal treatment, may have improved the interaction between the degradation products and the MXene surface. Moreover, the decomposition products may also help inhibits the mechanisms that are behind the electrochemical degradation of Ti_3C_2-550.

Table 5.1: Summary of electrochemical properties of MXene samples and XC72-R in air saturated 0.1M KOH electrolyte
[a] The $E_{1/2}$ of the first wave has been measured for the appropriate samples

	E_{onset} (V vs RHE)	$E_{1/2}$ before cycling [a] (V vs RHE)	$E_{1/2}$ after cycling [a] (V vs RHE)	$\Delta E_{1/2}$ (mV)
Ti_3C_2-550	0.72	0.61	0.53	80
Ti_3C_2-U1-550	0.76	-	-	-
Ti_3C_2-U10-550	0.78	0.64	0.53	110
Ti_3C_2-U50-550	0.76	0.65	0.58	70
Ti_3C_2-U10-800	0.82	0.67	0.6	40
Ti_3C_2-U50-800	0.88	0.734	0.73	10
XC72-R	0.80	0.70	0.64	60
Pt/C	0.96	-	-	-

5.3. Conclusion

In this chapter, Ti_3C_2 and the different urea treated samples have been electrochemically characterised, with a focus and their behaviour toward ORR. Firstly, we have determined that Ti_3C_2 on its own has very limited ORR performances, due to low intrinsic ORR properties of the materials, as well as a very small surface area of 9.5 $m^2.g^{-1}$ as measured in Chapter 4. To overcome these problems, several urea-treated materials have been synthesized with different urea content and annealing temperature to form a heterostructures composed of Ti_3C_2 with N-C compounds. It has been found that the introduction of N-C species on top of the MXenes have improved the overall ORR performance of the materials compared to Ti_3C_2 and is thought to be due to interactions between the decomposition products of the urea and the MXene surface.

Overall, for the samples treated at 550 °C, the ORR performance increased with the amount of urea, except for the mass ratio of 1:50 of Ti_3C_2 to urea, for which the performance got worse. It is explained by the synthesis of an excess of g-C_3N_4 all over the sample and has been supported by XRD and XPS results.

Moreover, the second thermal treatment at 800 °C has helped improve the ORR activity of the urea treated samples even further, especially for Ti_3C_2-U50-800, for which the ORR performance has drastically improved. The treatment at 800 °C seems to have improved the overall electrochemical stability of the prepared samples. One of the possible explanations is that the treatment at 800 °C allows for stronger interaction between the N-C compound and the MXene, providing more stability to the heterostructure.

CHAPTER 6: Fe$_3$C/Fe/Fe-N$_x$ functionalized N-Ti3C2@NC for Oxygen Reduction Reaction

6.1. Introduction

As seen in the previous chapter, the materials developed by the intercalation and the decomposition of urea within the MXene layers led to higher specific surface areas, which is a crucial parameter for a lot of applications, especially when it comes to electrochemical performance for catalysis. The materials synthesized have also shown to have some activity towards ORR. But the performance of the samples is still far from the benchmark catalyst for ORR, which is Pt/C. To improve the ORR performance of an electrocatalyst, several strategies are available, the main ones being: (1) increasing the intrinsic activity of the electrocatalyst, by introducing species with greater activity or by tuning the composition, (2) controlling the porosity distribution and surface area of the materials, (3) controlling the distribution and size of the electroactive species.

Based on the fact that the catalysts designed previously still have low surface area compared to usual electrocatalysts used for ORR, as well as lower intrinsic ORR activity, this chapter is focused on developing electrocatalysts while focusing on:

- using the MXene-based materials as support for catalyst particles with greater activity towards ORR. In addition to increasing the ORR activity by introducing better catalytic species, numerous studies have shown that MXenes could enhance the electrochemical activity of other catalysts for electrochemical reactions such as HER[174], OER[111,121], ORR[110] and others, by forming an electronic interaction between catalyst particles and the support. Several methods have been used to make these MXene/catalysts composites, such as electrostatic interactions, intercalation, impregnation, followed or not by a thermal treatment (hydrothermal treatment, pyrolysis under different atmosphere…).

- increasing the SSA of the materials. Indeed, the thermal treatment of the samples intercalated with urea led to an overall increase of the surface area of the samples, but the catalyst with the best ORR performance still had a very low surface area. The measured

BET surface area was 38.4 m².g^{-1}, which is around one order of magnitude lower compared to conventional Pt/XC72R catalysts, which exhibit surface area around 200-300 m².g^{-1}.

- controlling the distribution and morphology of the catalyst particles. Indeed, the catalysts particle size and distribution play an important role on the overall ORR performance of the final material.

To meet these conditions, a strategy relying on the intercalation of a Fe precursor along with urea, as C and N source, between Ti_3C_2 layers has been designed, followed by thermal annealing of the samples. The Fe precursor used is $FeCl_3$ and is expected to form iron species such as Fe, Fe_3C and/or $Fe-N_x$, which are materials that have shown to have good ORR activities, especially in alkaline media.[175-178] Moreover, based on the previous synthesis of the N-doped MXenes, a lot of the urea decomposition products are not being used and just lost in the gas stream. The addition of the Fe precursor is expected to catalyse the formation of carbon compounds on the surface of the MXenes from the decomposition products of urea during the high temperature thermal treatment. Indeed, Fe and Fe_3C have shown to be good catalysts for the growth of carbon nanofibers and nanotubes.[179] Finally, the layered nature of the MXenes and their capability to easily intercalate cations[180,181] will likely allow the intercalation of the Fe ions from the precursor and a homogenous distribution of the synthesized Fe-species.

In this chapter, the synthesized samples are going to first be physico-chemically characterized by XRD, ^{57}Fe Mössbauer spectroscopy, SEM-EDS, BET and XPS to determine the influence of the addition of the Fe-precursor on the chemistry and morphology of the different samples. The electrochemical performance towards ORR of the samples is then going to be probed using a 3-electrode setup in 0.1M KOH, through CVs, LSVs, RRDE measurements and stability testing.

6.2. Results and discussion

6.2.1. Synthesis and physico-chemical characterization

6.2.1.1. Influence of the introduction of FeCl₃ as Fe-precursor on the chemical structure of the samples

Based on our previous results, only samples with a Ti_3C_2 to urea ratio of 1:10 and 1:50 were considered for the synthesis of Fe-containing MXene catalysts. To compare the influence of the support on the Fe species synthesis, a sample where the MXene has been replaced by carbon black (XC72R) has also been synthesized: C-U50-Fe-800. The details for the synthesis of the different samples are given in the section 3.1.4 of the Materials and Methods chapter.

To study the effect of the introduction of $FeCl_3$ as Fe precursor on the chemical structure of our samples, XRD measurements have been carried out on the different Fe-containing samples to evaluate the crystalline phases present in our catalysts and will be compared to results discussed in section 4.2.2 of CHAPTER 4: The XRD patterns of the different samples are given in Figure 6.1. The XRD pattern of the reference sample C-U50-Fe-800, shows distinct peaks at 37.6°, 39.7°, 40.6°, 42.9°, 43.7°, 44.5°, 44.9°, 45.8°, 48.5° 49.1°, 51.8°, 54.2°, 56.2°, 58.0° and 61.4°, which are characteristic of the phase Fe_3C.[177] However, the peak intensities of the peaks at 44.5° and 44.9° does not match the literature, and a small peak at 65.0° is also present. Both of these can be explained by the presence of α-Fe in the sample, as the (110) and (200) planes of α-Fe have peaks at 44.5° and 65.0° 2θ.[177] Another broad peak around 25° is visible with an extra peak around 26° shouldering it. The broad peak is characteristic of amorphous carbon present in XC72R carbon black powders, while the peak around 26° can be attributed to the (002) plane of some organized graphitic carbon species in the sample.
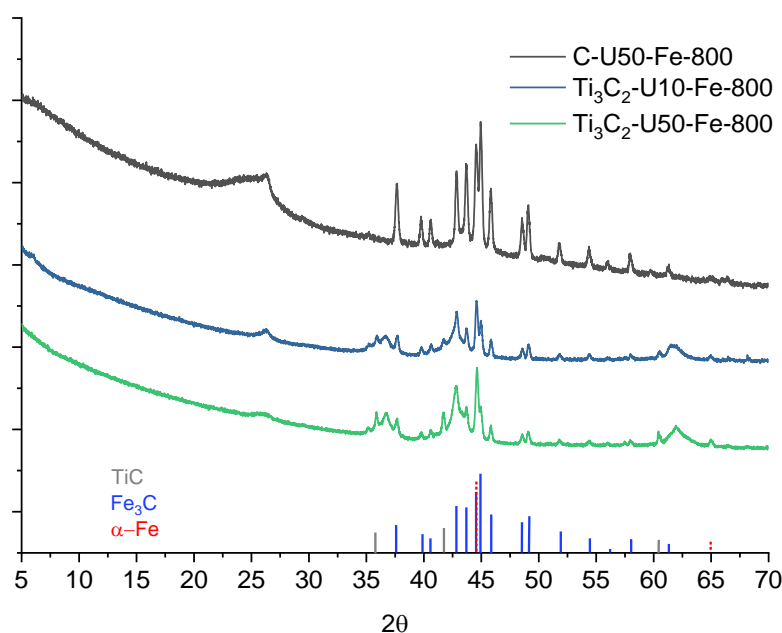
Figure 6.1: Broad XRD pattern of Ti₃C₂-U10-Fe-800, Ti₃C₂-U50-Fe-800, and C-U50-Fe-800 samples

The samples containing MXenes as support, Ti_3C_2-U10-Fe-800 and Ti_3C_2-U50-Fe-800, both display the same Fe_3C and α-Fe peaks as C-U50-Fe-800. It should be noted that the intensity ratio of the peaks at 44.5° and 44.9° differs between samples, meaning that the composition of the Fe phases varies based on the support being used and the amount of urea. This will be discussed more thoroughly later on. The peak at 26° is also present, showing the presence of some graphitic carbon in the samples. Based on the XRD pattern of the samples Ti_3C_2-U10-800 and Ti_3C_2-U50-800, given in Figure 4.8 of the previous chapter where the peak at 26° is absent, it can be inferred

that the graphitic carbon was formed during the synthesis of the samples and that the Fe-species are playing a key role in the process. Moreover, the XRD results do not show peaks relating to TiO_2 phases, such as rutile or anatase, which have strong diffraction peaks at 2θ $25°$ and $27°$ respectively. The MXene does not seem to have been oxidized into TiO_2 rutile or anatase during the thermal treatment, even with the introduction of the Fe precursor. In addition to the Fe-species and the carbon peaks, the MXene samples show characteristic peaks of TiC, at $35.9°$, $41.7°$ and $60.5°$, coming most likely from impurities in the starting materials as well as some possible surface degradation. Also, a set of broad peaks centred around $36.6°$, $42.9°$ and $61.7°$ is present, these peaks could be from some MXenes layer arrangement or from titanium nitride forming on the surface during the thermal step. It must be noted that, although the synthesis method is the same between Ti_3C_2-Ux-800 and Ti_3C_2-Ux-Fe-800 except for the addition of Fe precursor, the (002) MXene peak doesn't seem to be showing in the XRD pattern of the sample. Based on the results from the previous chapters, in which thermal treatment done at 800°C of urea-treated samples, still showed the presence of MXene on the XRD pattern, it is very unlikely that the MXene structure has been completely degraded. The most probable explanation is that the formation of extra carbonaceous species between the MXene layers has completely disordered the MXene structure along the [002] direction, leading to the peak not being visible on the XRD pattern.

Elemental analysis of the samples Ti_3C_2-U10-Fe-800 and Ti_3C_2-U50-Fe-800 was performed using EDS measurements. The elemental composition is presented in Table 6.1, and the EDS mapping is shown in Figure 6.2. Based on the results for the samples without the introduction of $FeCl_3$, presented earlier in Chapter 4, the addition of the Fe precursor has led to a decrease in Ti atomic proportion in the sample, meaning that more urea decomposition products have reacted with the materials during the thermal treatment, to form nitrogen and carbon containing compounds. This is in agreement with the XRD, where a small graphitic carbon peak has appeared for Ti_3C_2-U10-Fe-800 and Ti_3C_2-U50-Fe-800. To make the comparison easier, the compositions of C, N and Fe have also been normalized by the amount of Ti to make the comparison easier between samples. It can definitely be seen that the overall proportion of carbon and nitrogen content has increased relatively to Ti for the samples containing Fe. Moreover, as expected, the atomic proportions of Ti and Fe are similar for both Ti_3C_2-U10-Fe-800 and Ti_3C_2-U50-Fe-800, as the amount of both Ti_3C_2 and $FeCl_3$ were the same during the synthesis.

Table 6.1: EDS elemental composition of Ti$_3$C$_2$-Ux-Fe-800 samples and Ti$_3$C$_2$-Ux-800 samples for comparison [a] averaged over 3 measurements

(at%) [a]	Ti	C (C/Ti)	O	N (N/Ti)	Fe (Fe/Ti)	Cl	Al
Ti$_3$C$_2$-U10-*Fe-800*	11.3 ± 3.9	70.1 ± 6.2 (6.20)	9.8 ± 0.2	3.6 ± 1.5 (0.32)	4.2 ± 0.4 (0.37)	0.8 ± 0.2	0.2 ± 0.1
Ti$_3$C$_2$-U10-800	23.0 ± 0.9	50.3 ± 2.8 (2.19)	19.2 ± 1.0	5.5 ± 0.2 (0.24)	-	1.1 ± 0.2	0.3 ± 0.1
Ti$_3$C$_2$-U50-Fe-*800*	10.7 ± 1.3	63.8 ± 6.5 (5.96)	13.5 ± 3.8	6.5 ± 2.3 (0.61)	4.4 ± 1.2 (0.41)	0.3 ± 0.2	0.4 ± 0.3
Ti$_3$C$_2$-U50-800	17.2 ± 0.8	61.1 ± 2.4 (3.55)	13.9 ± 0.7	5.7 ± 0.3 (0.33)	-	0.5 ± 0.0	0.4 ± 0.2
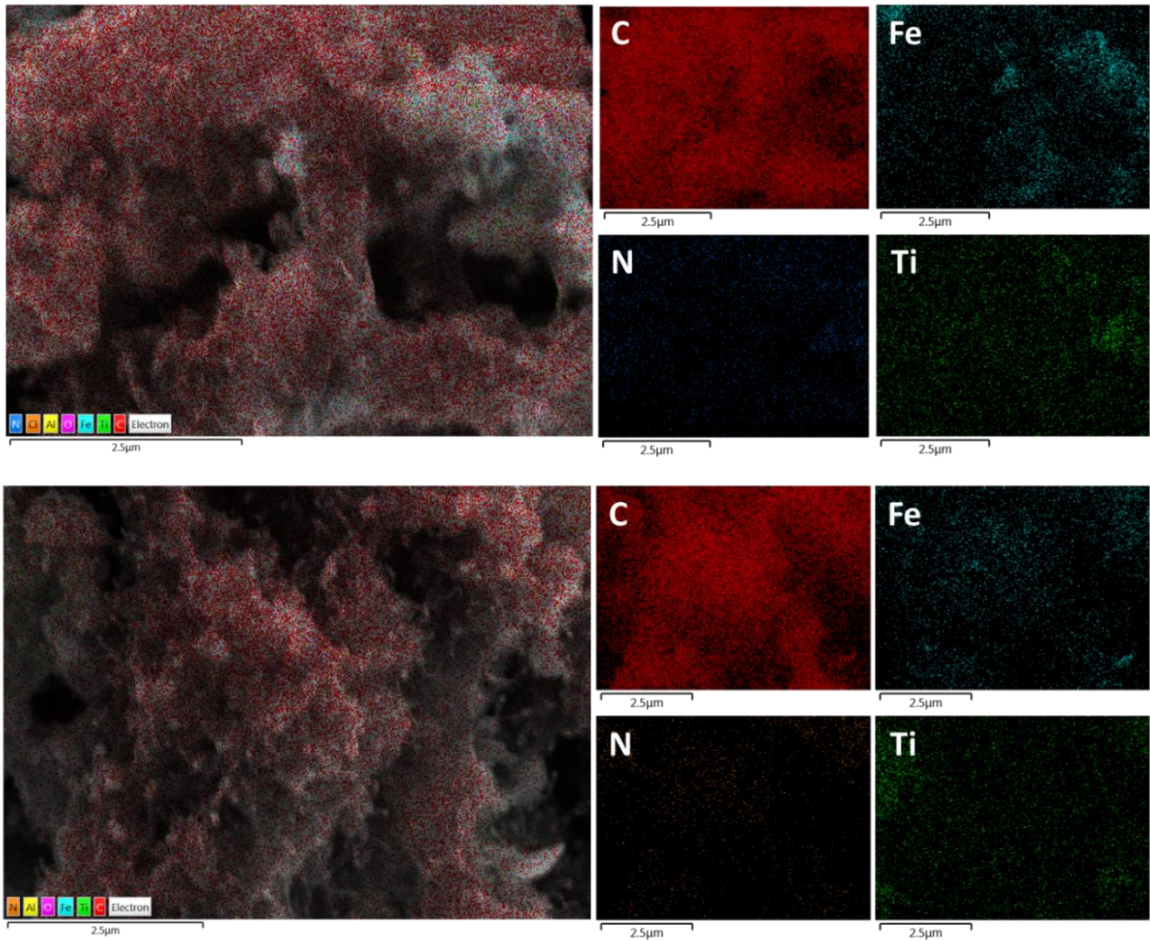
Figure 6.2: Elemental composition EDS pictures of Ti$_3$C$_2$-U10-Fe-800 (top), and Ti$_3$C$_2$-U50-Fe-800 (bottom)

The EDS mapping of Ti$_3$C$_2$-U10-Fe-800 and Ti$_3$C$_2$-U50-Fe-800 for Ti, C, N and Fe is shown on Figure 6.2. The main takeaway from it is that the carbon mapping shows a high distribution of carbon species, even on top of the materials, while the Ti mapping, which shows that Ti is present everywhere with a few spots with higher concentration, is not as intense as carbon. This leads to believe carbon species have covered most of the MXene flakes. The nitrogen signal, although being low, seems to show a homogenous distribution throughout the samples. The Fe EDS

mapping for Ti₃C₂-U50-Fe-800 shows an even Fe distribution with a few spots with higher Fe density, while the Fe distribution for Ti₃C₂-U10-Fe-800 seems to be a lot less homogenous, and the Fe looks more aggregated to specific regions.

6.2.1.2. Characterization and analysis of the Fe species

To get further insight concerning the composition of the Fe-species present in the sample, an analysis of the XRD pattern between 2θ values of 39° and 50° has been performed (Figure 6.3). From the intensities of the two peaks at 44.5° and 44.9°, it is clear that there is a distinct distribution of the Fe-species in the different samples and that it both depends on the amount of urea and the support used for the synthesis. The Fe_3C/Fe ratio determined from Rietveld analysis of the XRD patterns are given in Table 6.2. and are as follow: 5.4, 3.4, 16.8 for Ti₃C₂-U10-Fe-800, Ti₃C₂-U50-Fe-800 and XC72R-U10-Fe-800 respectively. The highest proportion of Fe_3C for the sample containing XC72R instead of MXene can be explained by the presence of more carbon readily available to react, during the thermal annealing, with the Fe introduced from $FeCl_3$. Indeed, during the annealing, the Fe can react with both the urea decomposition products and the XC72-R carbon support. Moreover, it has already been shown from other studies that MXenes interact easily with cations, leading in a lot of cases to spontaneous intercalation and diffusion of cations between the MXene layers.[180] The presence of the MXenes allows the intercalation and interaction of the Fe and stops it from readily reacting to form Fe_3C, which would also explain the lower Fe_3C content relatively to Fe. The lower Fe_3C to α-Fe ratio for Ti₃C₂-U50-Fe-800 compared to Ti₃C₂-U10-Fe-800 while introducing more urea could not be explained and would require further investigation.
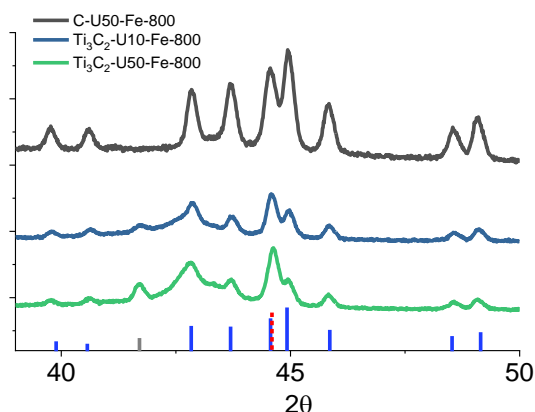
Table 6.2: Fe3C/α-Fe ratios calculated from XRD analysis of the [39°;50°] region

Sample	Fe3C/α-Fe
Ti₃C₂-*U10-Fe-800*	5.4
Ti₃C₂-*U50-Fe-800*	3.4
C-*U50-Fe-800*	16.8

Figure 6.3: XRD pattern of Ti₃C₂-U10-Fe-800, Ti₃C₂-U50-Fe-800, and C-U50-Fe-800 samples between 39° and 50°

As XRD is a technique that only allows for the detection of crystalline compounds, it has been decided to carry out ⁵⁷Fe Mössbauer spectroscopy of the samples. The Mössbauer spectroscopy

has the advantage to be able to detect all the Fe in a sample, regardless of its physical state and the signal measured is directly proportional to the amount of Fe-species in the sample. The details of the deconvolution can be found in Annexe B. The deconvolution of the Mössbauer spectra is given in Figure 6.4 and shows that the spectra of all three samples have been deconvoluted into one doublet and two sextets.

Based on literature regarding Mössbauer spectroscopy measurement of different Fe-containing species,[137,182,183] the doublet has been attributed to Fe-N_x species, which are usually seen in N-doped carbon materials containing Fe, where Fe can form Fe-N_x moieties with four pyridine-like nitrogen on the carbon layer as depicted in Figure 6.5. Moreover, the sextet 1 and sextet 2 are attributed to α-Fe and Fe_3C respectively. These results are in agreement with the previous XRD measurements, where both α-Fe and Fe_3C were detected. The Fe-N_x species, on the other hand could not be picked up by XRD due to the non-crystalline nature of the compound. The Fe-species compositions of the different samples are given in Table 6.3, and seem to corroborate the XRD analysis done previously. Indeed, the Fe_3C/α-Fe ratios are similar to the one calculated from XRD analysis and are following the same trend. In addition to the evolution of the α-Fe and Fe_3C, which was discussed earlier, the content of Fe-N_4 in the sample increases with the amount of urea, which can be explained by a greater amount of nitrogen available to form these moieties. Moreover, the Fe-N_x content for the sample containing XC72R decreases drastically and amounts only to 7% of the Fe-species. This can be explained by the spatial confinement the MXenes layers can bring to the Fe ions and the urea, which inhibits the agglomeration of the Fe into bigger particles during the thermal treatment (See SEM results discussed in the next part), which allows for more Fe to reacts and form Fe-N_x moieties.

Table 6.3: Fe-species composition taken from experimental ^{57}Fe Mössbauer analysis of Ti_3C_2-U10-Fe-800, Ti_3C_2-U50-Fe-800 and C-U50-Fe-800

(at%)	Doublet 1 (Fe-N_x)	Sextet 1 (α-Fe)	Sextet 2 (Fe_3C)	Fe_3C/α-Fe
Ti_3C_2-U10-Fe-*800*	15.8	15.8	68.3	4.3
Ti_3C_2-U50-Fe-*800*	18.3	23.8	57.9	2.4
C-U50-Fe-*800*	7.0	6.0	87.0	14.5
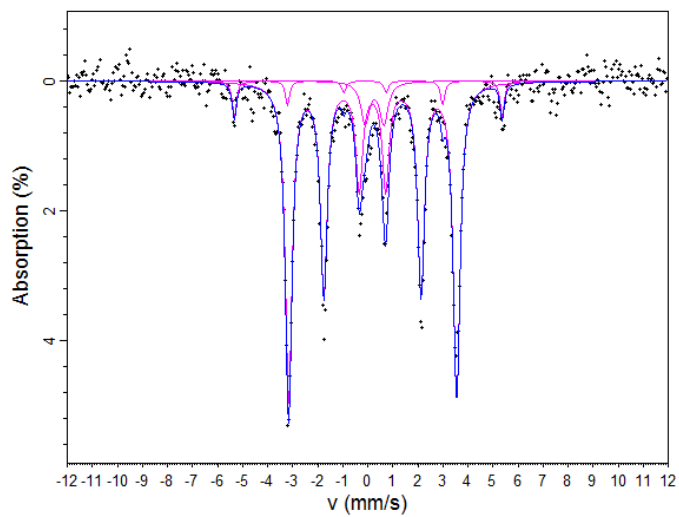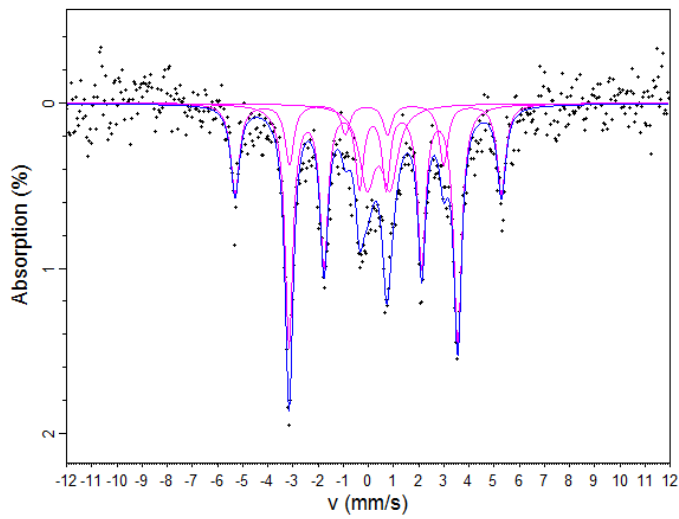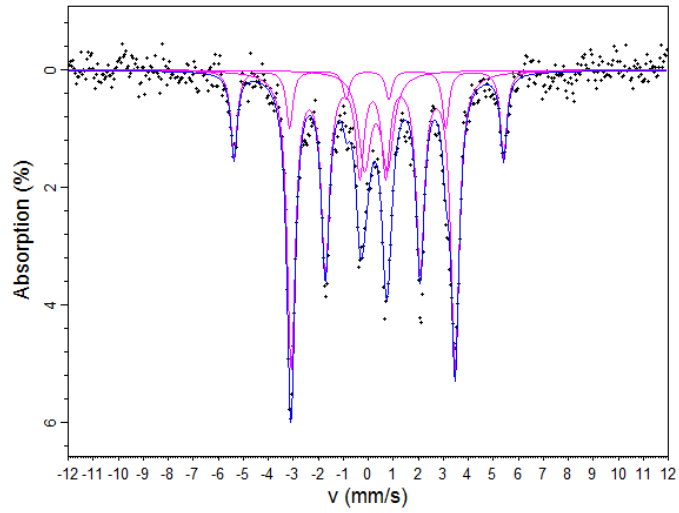
Figure 6.4: Experimental ^{57}Fe Mössbauer transmission spectra at 293 K of (a) Ti₃C₂-U10-Fe-800, (b) Ti₃C₂-U50-Fe-800 and (c) C-U50-Fe-800 and their fitting
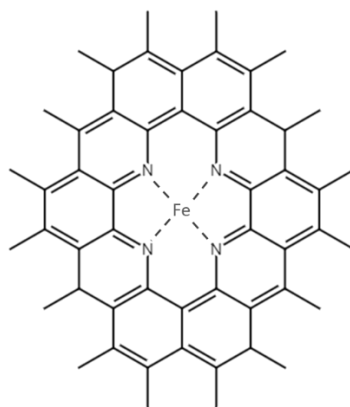
Figure 6.5: Example schematic of a Fe-N$_4$ moiety in carbon materials

6.2.1.3. Morphology characterization of the samples

With the bulk chemistry of our samples already characterized, the morphology of the materials synthesized needs to be examined. This has first been analysed by SEM and is presented in Figure 6.6. The morphology of the Ti$_3$C$_2$-U10-Fe-800 displays interconnected flake-like particles, with small spherical particles dispersed on it. The flake-like MXene particles don't seem to have any particular arrangement, which explains the (002) peak missing from the XRD pattern. In the case of Ti$_3$C$_2$-U50-Fe-800 the flake-like particles are still present, and there seems to be more and smaller particles spread across the materials compared to the Ti$_3$C$_2$-U10-Fe-800 but is not conclusive enough to infer an influence on particle size based on the Ti$_3$C$_2$:urea ratio, although EDS mapping has shown the Fe species to less homogenously distributed in the materials. And interesting difference between of Ti$_3$C$_2$-U10-Fe-800 of Ti$_3$C$_2$-U50-Fe-800 is that carbon nanotubes (CNTs) or nanofibers (CNFs) seems to have grown on the MXenes support for of Ti$_3$C$_2$-U50-Fe-800 (see Figure 6.7), while it does not seem to be visible on the MXene sample containing less urea. C-U50-Fe-800, as a reference sample with XC72-R as support, shows the characteristic morphology of XC72-R, and also clearly exhibits CNTs with spherical particles encapsulated in them (a close-up SEM picture is shown on Figure 6.7). As seen in the literature, Fe and/or Fe$_3$C are both good catalysts for the growth of CNTs,[179] and the Fe ions after being reduced to Fe$_3$C and Fe during the thermal treatment are allowing for CNTs to start growing on the carbon support by reacting with the decomposition products of urea. Moreover, a higher amount of urea allows for more decomposition products to be formed and react with the Fe/Fe$_3$C particles to form CNT/CNF on the sample.

From the SEM pictures, it can be seen that the introduction of Fe-precursor led to the formation of carbon species on top of the different support used, XC72R or Ti$_3$C$_2$, which agrees with the XRD results discussed previously, in which a characteristic (002) carbon peak is visible for all samples. This result is also supported by literature. For instance, Zhong & al. have made N-doped

carbon nanotubes with encapsulated Fe_3C and Fe by pyrolysis under Ar a mix of melamine and $FeCl_3$ at 800°C.[184] It was shown that the Fe-precursor/melamine mix would form Fe_xO_y if pyrolyzed at 650°C, but would undergo reduction to Fe_3C/Fe at temperatures above 680°C. In the meantime, the carbonous species from the degradation of melamine would form carbon nanotubes at pyrolysis temperatures between 700-800°C around the Fe_3C/Fe particles and encapsulate them.
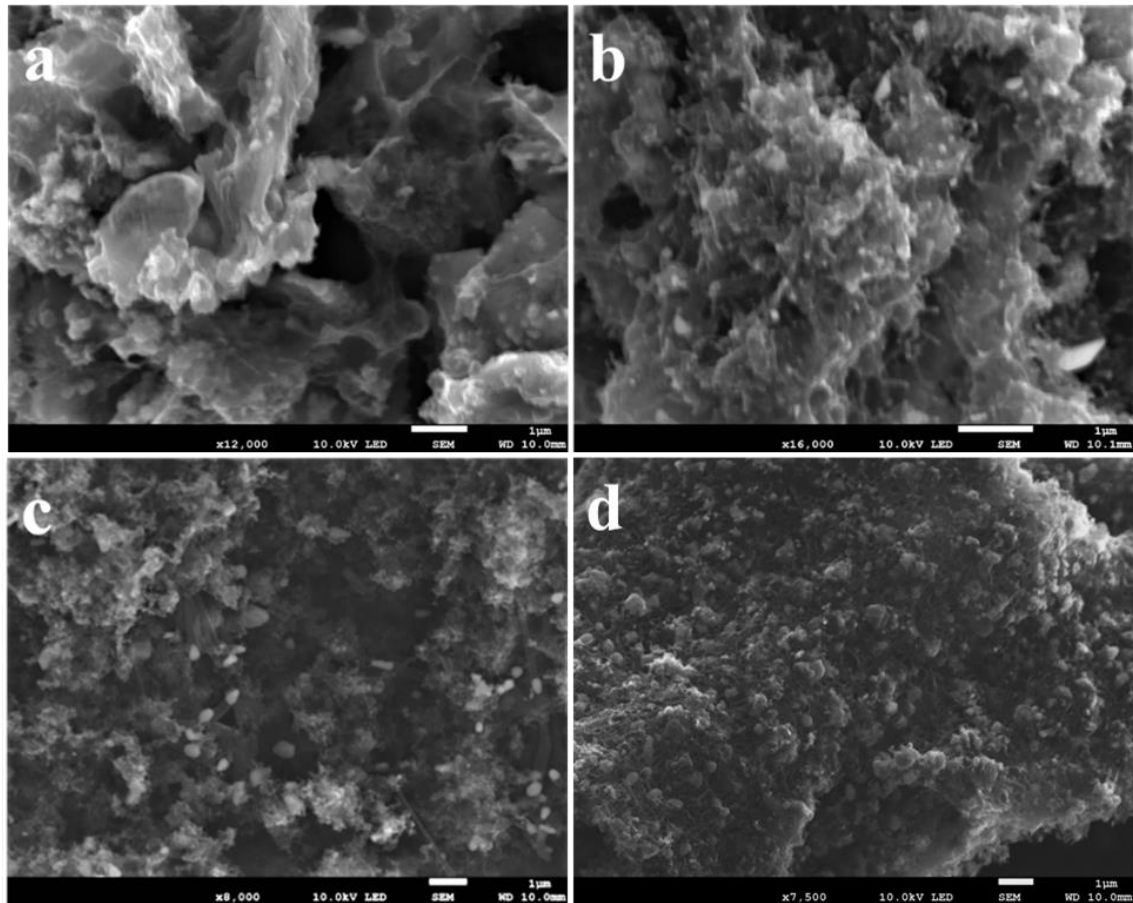
Figure 6.6: SEM pictures of (a) Ti₃C₂-U10-Fe-800, (b) Ti₃C₂-U50-Fe-800, (c) C-U50-Fe-800 and (d) U50-Fe-800 samples (scale bar: 1 μm)

The picture (d) in Figure 6.6 shows the structure of the materials synthesized following the same procedure as the samples Ti_3C_2-U50-Fe-800 and C-U50-Fe-800 without any of the MXene or XC72-R supports. The materials synthesized displays a porous network with bigger sphere-like particles attached to it. The morphology of this sample shows that the use of a support, MXene or XC72-R, is helpful to avoid the coalescence of the Fe containing species into bigger particles during the thermal treatment.
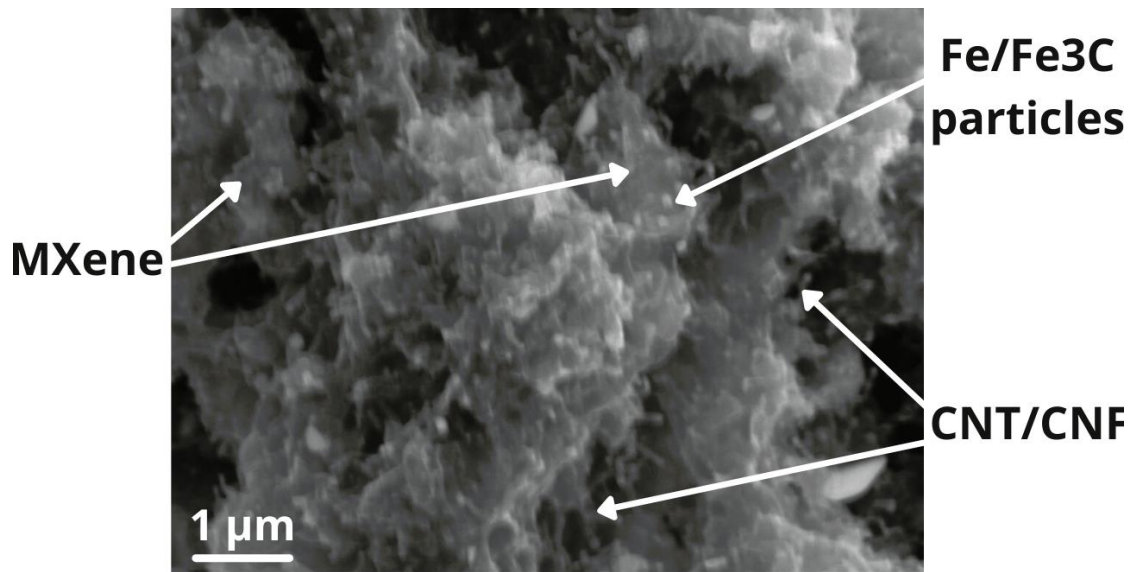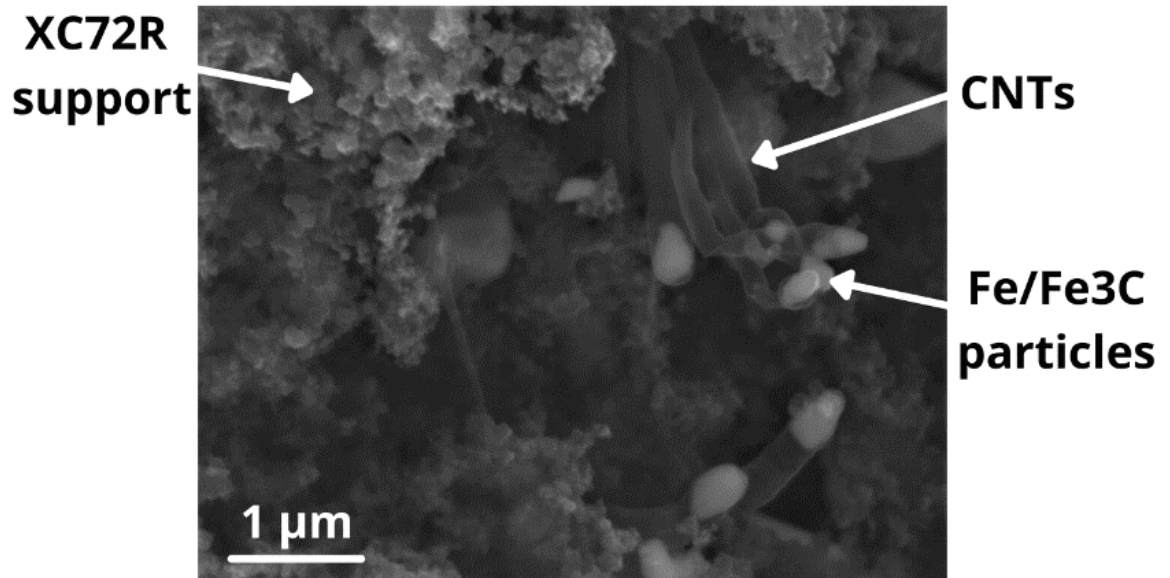
Figure 6.7: SEM picture of C-U50-Fe-800 (top) and Ti$_3$C$_2$-U50-Fe-800 (bottom) with the different structures present
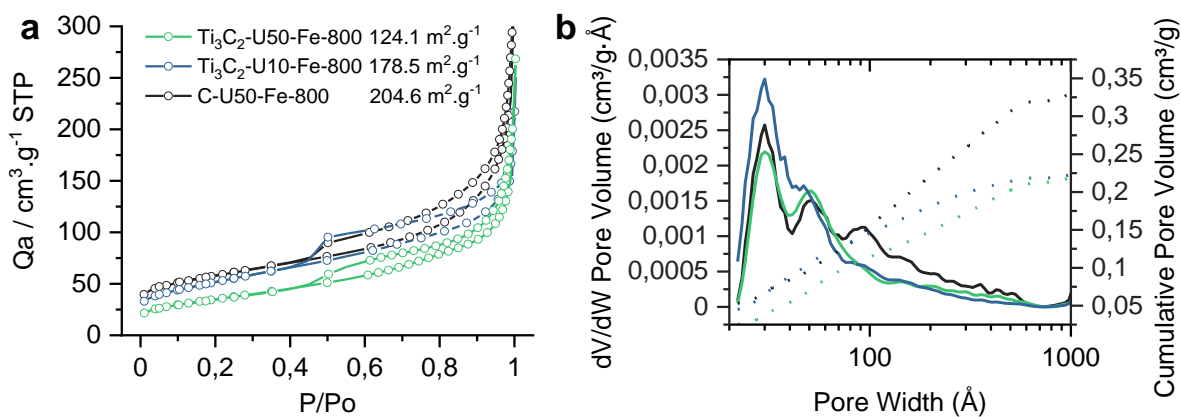
Figure 6.8: (a) Adsorption isotherms from N₂ adsorption-desorption experiments of Ti₃C₂-U10-Fe-800, Ti₃C₂-U50-Fe-800 and C-U50-Fe-800. The calculated surface area is given in the legend, (b) Pore size distribution from NLDFT of the Fe-containing samples: cumulative pore volume (dotted line) and dV/dW pore volume (solid line)

To determine the influence of the addition of the Fe precursor (Fe_3Cl) during the synthesis on the surface area and porosity of the samples, N_2 adsorption-desorption experiments were carried out, and the isotherms are presented in Figure 6.8.a. The isotherms of all three samples are, based on the IUPAC classification guide, type IV isotherms, which is characteristic of porous materials, especially with mesopores, due to the presence of the hysteresis loop representative of capillary condensation occurring in mesopores. The hysteresis loop occurring between 0.5 to 1 p/p° is a H3 hysteresis for all samples, that is the distinctive hysteresis type for non-rigid aggregates of plate like particles, displaying a slit-shaped pore structure. BET surface area measurements of the samples containing Fe show that the presence of the Fe precursor has drastically improved the surface area of the MXene samples compared to their counterparts without it, which were discussed previously (Figure 4.12). The surface area measured for Ti_3C_2-U10-Fe-800 and Ti_3C_2-U50-Fe-800 are 178.5 $m^2.g^{-1}$ and 124.1 $m^2.g^{-1}$ respectively, up from 23.4 $m².g^{-1}$ and 38.4 $m².g^{-1}$ for Ti_3C_2-U10-p800 and Ti_3C_2-U50-800. The increase in surface area shows that the presence of the precursor allows, by acting as a catalyst, the formation of a greater amount of carbon species from urea and g-C_3N_4 decomposition products on the surface of the MXenes during the thermal treatment. This increase in SSA of the different samples, in addition to the formation of species carbonous species containing nitrogen and Fe_3C and Fe-N_x as discussed earlier, should be beneficial in term of electrochemical activity. It is interesting to note that although more carbonous precursors are available during the synthesis of Ti_3C_2-U50-Fe-800 compared to Ti_3C_2-U10-Fe-800, the surface area measured of the former is smaller. Further investigation would be required to clearly understand why this is occurring. The reference samples using XC72R as replacement for the MXene during the synthesis, on the other hand, shows a lower surface area compared to bare XC72R (247.2 $m^2.g^{-1}$), displaying a SSA of 204.6 $m^2.g^{-1}$ for the composite materials.

The pore size distribution of the samples is presented in Figure 6.8.b and was carried out using NLDFT with a slit pore model. The cumulative pore of the Ti_3C_2-Ux-Fe-800 samples are both around 0.225 $cm^3.g^{-1}$, which is greater than the samples prepared without the Fe precursor. Moreover, the pore size distribution for the Fe-containing MXene samples display pore sizes with two peaks, one centred around 3.0 nm and the other one at 4.9 nm, as well as a broad pore size window from 10 to 60 nm. In the case of Ti_3C_2-U10-Fe-800, the peak at 3 nm is sharper and the peak at 4.9 nm is shouldering the first peak, showing the presence of more pore with intermediate size compared to the sample Ti_3C_2-U50-Fe-800. C-U50-Fe-800 pore size distribution is slightly different, with a cumulative pore volume reaching around 0.3225 $cm^3.g^{-1}$, and three distinct peaks centred around 3, 5 and 10 nm.

6.2.1.4. Surface chemistry analysis

Lastly, it is important to investigate the surface chemistry of the different samples, as the surface/electrolyte interface is where electrochemical reactions happen. It is especially interesting to see the effect of introducing $FeCl_3$ on the surface chemistry of the different samples. Therefore, XPS has been performed to study the states of Ti, C, N and Fe to understand the chemical environment at the materials surface.

The broad XPS spectra and the surface chemical composition calculated from the XPS analysis are given in Figure 6.9 and Table 6.4 respectively. All three samples show a main peak centred around 282 - 292 eV corresponding to the C1s contribution. Carbon is the biggest contribution to the surface chemistry of all samples, which was to be expected for C-U50-Fe-800, but even for Ti_3C_2-U10-Fe-800 and Ti_3C_2-U50-Fe-800. A comparison of the amount of surface C relative to Ti for the samples with and without the Fe precursor is given in Figure 6.9, and show that the samples in which the Fe precursor was added during the synthesis have a significantly higher content of carbon on the surface compared to the samples without Fe. This result is in accordance with the previous XRD and SEM observations and it can be reasonably be concluded that the MXene flakes have been covered with carbon species. In addition to the C1s peak, a small Ti2p at 454-466 eV is present in MXene samples, as well as O1s peak (~ 528 - 535 eV) for all samples. Concerning the N1s peak (~ 395 - 404eV) and the Fe2p peak (~ 705 - 735 eV), their intensity is very small, and are almost not visible on the broad XPS spectrum of C-U50-Fe-800. Based on the XRD results, showing obvious peaks for α-Fe and Fe_3C, and the EDS chemical characterization, the low Fe2p peak intensity could be explained by the fact that the Fe-species are encapsulated within carbon layers, which is usually what have been reported when Fe species have been used as catalysts to grow carbon structures. Following the same trend as for the C content, the amount

of surface nitrogen detected by XPS has increased in MXene samples containing Fe-species compared to the samples without.
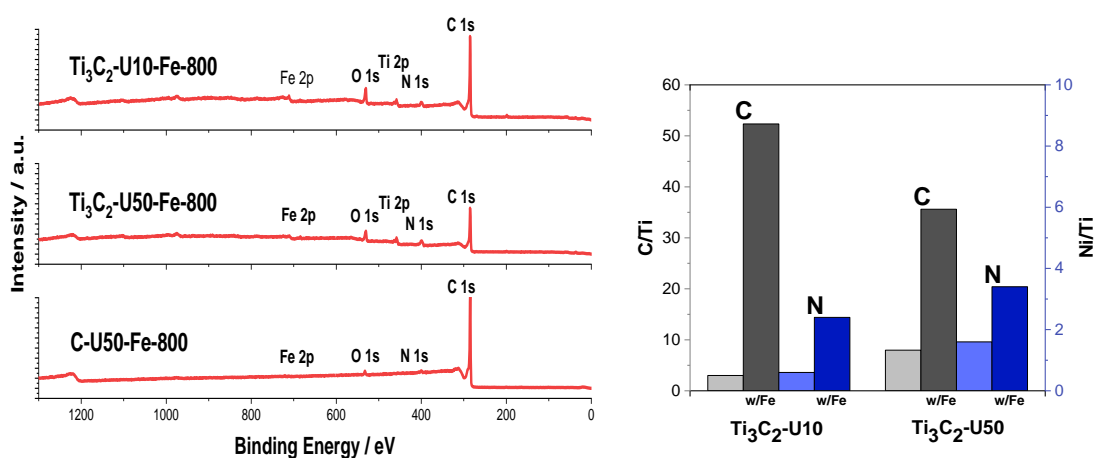
Figure 6.9: Full XPS spectra of Fe-containing catalysts(left, surface carbon and nitrogen content relative to Ti in samples treated at 800 °C with and without Fe₃Cl (right)

Table 6.4: Surface elemental composition of Ti3C2-Ux-Fe-800 and C-U50-Fe-800 samples from XPS analysis

At%	Ti 2p	C 1s (C/Ti)	O 1s	N 1s (N/Ti)	Fe 2p	F 1s	Cl 1s
Ti₃C₂-U10-Fe-800	1.63	85.31 (52.34)	7.51	3.96 (2.4)	0.62	0.24	0.73
Ti₃C₂-U50-Fe-800	2.25	80.09 (35.60)	8.25	7.73 (3.4)	0.57	0.63	0.49
C-U50-Fe-800	-	97.63	1.50	0.81	0.06	-	-

The Ti2p peak-fitted spectra of Ti₃C₂-U10-Fe-800 and Ti₃C₂-U50-Fe-800 are given in Figure 6.10, and display the typical 2p spin-orbit splitting of titanium. The spectra could be both deconvoluted into 4 components at (455.3 eV / 4460.0 eV), (456.3 / 461.2) eV, (457.7 / 462.8) eV and (458.7 / 464.4) eV corresponding respective to Ti-C, Ti^{2+}, Ti^{3+} and Ti^{4+} respectively. As discussed in section 4.2.2.2 of CHAPTER 4: Physicochemical characterization of N-Carbon on N-Ti₃C₂, the variation of the oxidation state of surface Ti shows that there has been a change in the chemical environment at the surface of the MXenes, showing electronic interaction between the MXene support and the Fe-containing carbon structure which was formed on top of it during the synthesis.

The C1s spectra was deconvoluted into five peaks. The main peak centred at 284.8 eV, corresponding to C-C bonds, and was attributed to the carbon structures formed on top the MXenes. Moreover, there is no obvious C-Ti at around 282 eV, which is a peak characteristic from Ti₃C₂. A very small shoulder at 283.9 eV is present and is believed to be corresponding to

the C-Fe bond from Fe$_3$C based on literature.[137,185] based on these results and the XPS elemental composition from Table 6.4, it can be concluded that apart from small amount of Ti$_3$C$_2$ and Fe species which are still detected as surface species, most of the MXene and Fe species are covered and/or encapsulated in carbonous compounds.
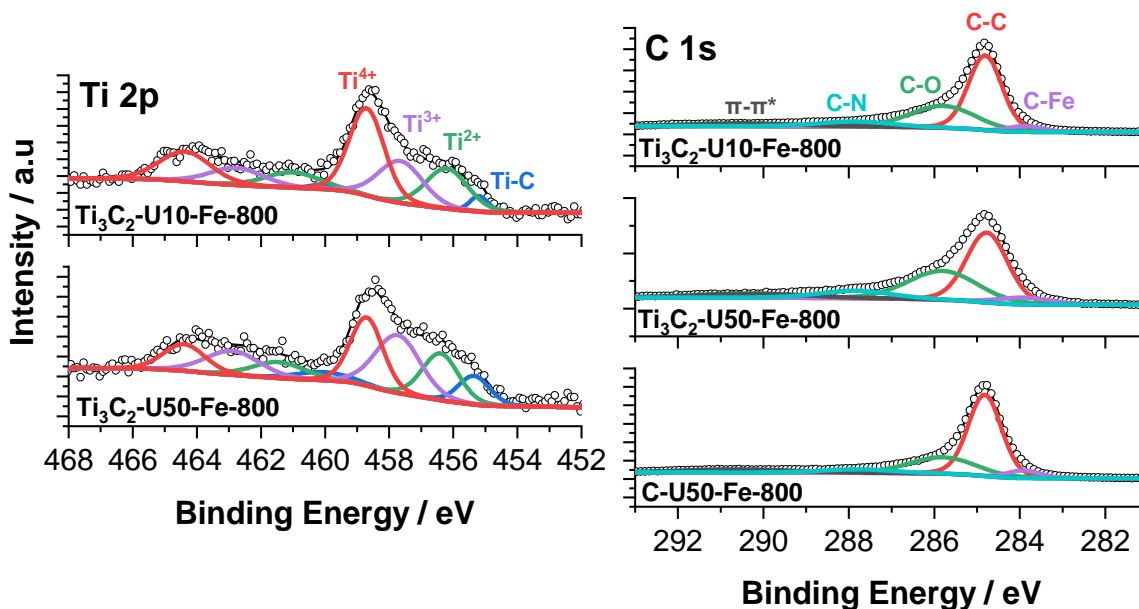
Figure 6.10: Ti2p XPS spectra of Ti$_3$C$_2$-U10-Fe-800 and Ti$_3$C$_2$-U50-Fe-800 (left) and C1s XPS spectra of Ti$_3$C$_2$-U10-Fe-800, Ti$_3$C$_2$-U50-Fe-800 and C-U50-Fe-800 (right)

Table 6.5: Ti2p XPS peak fitting distribution (more details in appendix A)

	Ti-C	Ti^{2+}	Ti^{3+}	Ti^{4+}
B.E (eV)	455.1	456.2	457.5	458.8
(at%)	(460.4)	(461.5)	(462.8)	(464.5)
Ti$_3$C$_2$-U10-Fe-800	4.09	24.37	27.03	44.83
Ti$_3$C$_2$-U10-800	12.97	20.97	20.20	45.85
Ti$_3$C$_2$-U50-Fe-800	12.04	22.85	35.14	29.97
Ti$_3$C$_2$-U50-800	18.24	29.22	34.70	17.85

The chemical state of nitrogen and Fe-species, as well as their local environment, on the surface of the materials are keys in term of catalytic performance towards ORR. Therefore, investigating N1s and Fe2p spectra is of interest. The N1s XPS spectra of the different samples are given in Figure 6.11. The spectra of Ti$_3$C$_2$-U10-800 and Ti$_3$C$_2$-U50-800 are also given to better understand the role played by the Fe precursor on the surface chemistry of the different materials. Firstly, the N1s spectra of all the samples can be deconvoluted into four peaks, except for C-U50-Fe-800, with binding energies around 396.4, 398.7, 400.2 and 401.4 eV, which can be assigned to N-Ti

bonds, pyridinic N (N1), pyrrolic N (N2) and graphitic N (N3), respectively. The XPS peak fitting distribution is given in Table 6.6, where the atomic concentrations of the different N species are presented. The proportions of the different N species on the surface of both MXene samples are very similar, even with a urea content which is 5 times as much for Ti_3C_2-U50-Fe-800 compared to Ti_3C_2-U10-Fe-800. It can still be noticed that the Ti_3C_2-U50-Fe-800 samples contains a bit more pyridinic N and a bit less graphitic N. Based on previous studies, Fe-N_x species usually forms at pyridinic N, where Fe atoms coordinate with pyridinic N,[186,187] meaning that a proportion of the pyridinic N (N1) peak can be attributed to Fe-N_x moieties. In some case it is possible to deconvolute the N1 peak into two separate peaks, pyridinic N and Fe-N_x due to a small shift of the Fe-N_x peak relatively to pyridinic N that do not interact with a Fe centre, but the data was found to be too noisy to be able to perform this deconvolution and have meaningful data.
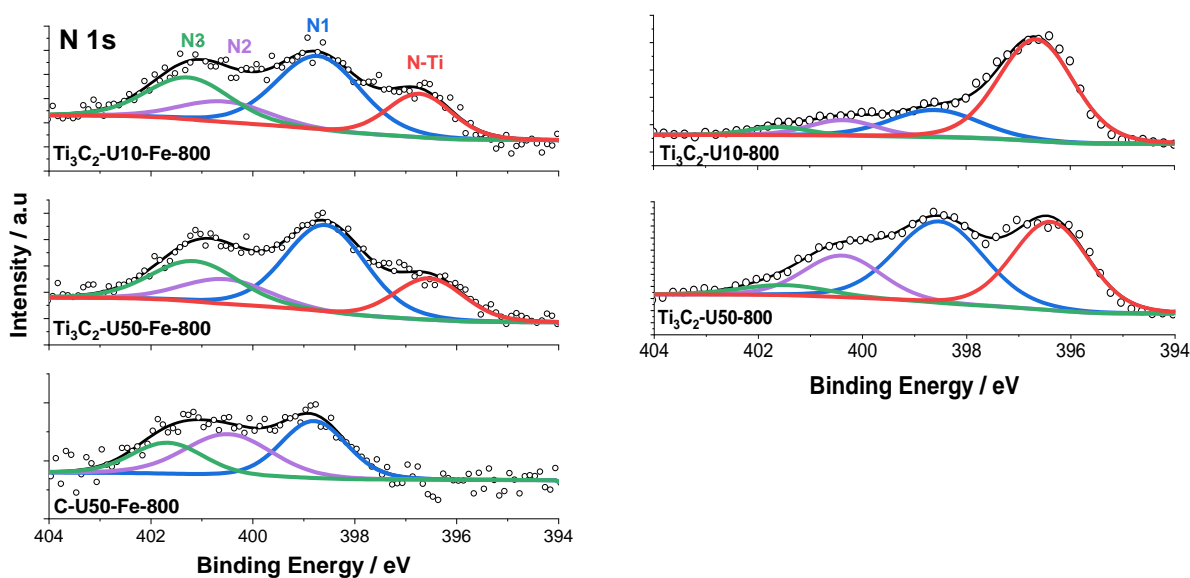
Figure 6.11: N1s XPS spectra of Ti_3C_2-U10-Fe-800, Ti_3C_2-U50-Fe-800 and C-U50-Fe-800 (left) and of Ti_3C_2-U10-800 and Ti_3C_2-U50-800 (right)

Table 6.6: N1s XPS peak fitting distribution (more details in appendix A)

	N-Ti	N1	N2	N3
B.E (eV) **(at%)**	396.4	398.7	400.2	401.4
Ti_3C_2-U10-Fe-800	19.78	43.31	12.55	24.37
Ti_3C_2-U10-800	63.12	27.36	5.80	3.71
Ti_3C_2-U50-Fe-800	18.49	45.14	13.77	22.61
Ti_3C_2-U50-800	37.01	39.75	18.96	4.28
C-U50-Fe-800	-	39.21	37.45	23.34

The Fe2p spectra of the samples are presented in Figure 6.12. The overall XPS signal for Fe being of very small intensity, a lot of noise has been introduced. Therefore, a deconvolution of the Fe 2p spectra has not been successful. Although the deconvolution was not possible, peaks are still visible on spectra of Ti_3C_2-U10-Fe-800 and Ti_3C_2-U50-Fe-800. The two peaks detected are located at around 711.5 eV and 724.9 eV.
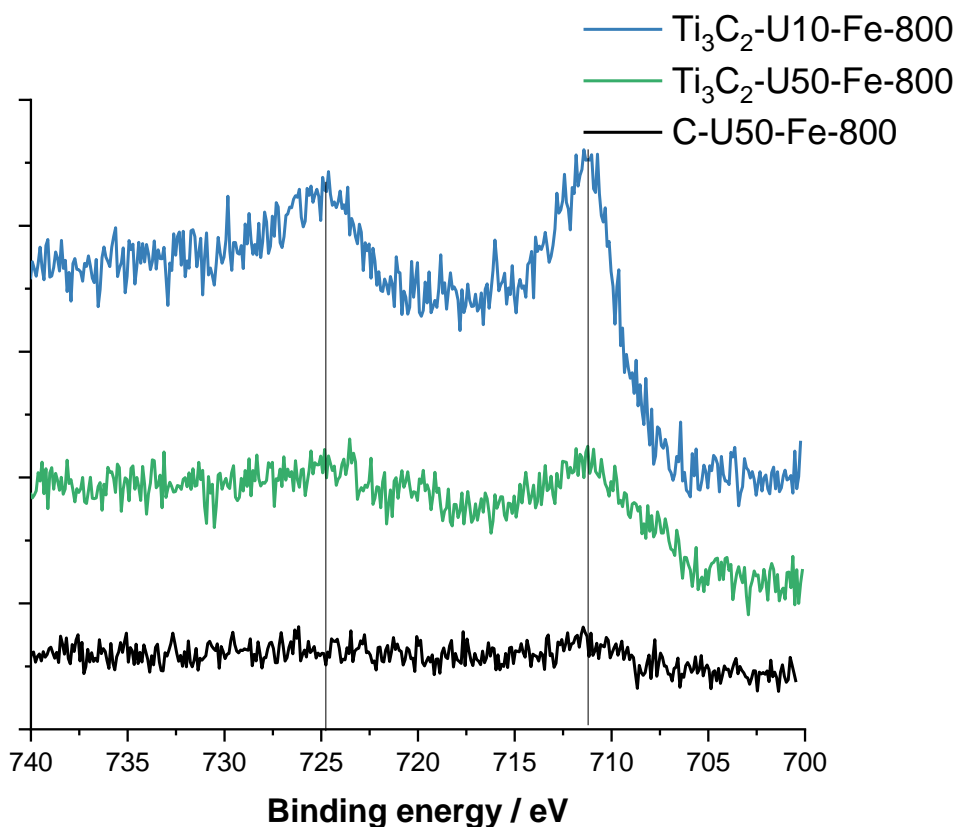
Figure 6.12: Fe2p XPS spectra of Ti3C2-U10-Fe-800, Ti3C2-U50-Fe-800 and C-U50-Fe-800

As discussed in the introduction to this chapter, the main objective for the $FeCl_3$ introduction during one of the synthesis steps was to be able to increase the overall surface area of our materials, while introducing species which could improve activity of the materials towards ORR. Synthesized materials, independently of the proportion of urea, have shown greater surface area than their counterpart in which no $FeCl_3$ was added. Moreover, the chemical characterization shows a greater C and N content, as well as the formation of Fe-species such as Fe_3C, α-Fe and Fe-N$_4$, which have shown to have interesting ORR properties in alkaline media.[176] Also, based on the XRD, [57]Fe Mössbauer spectroscopy, and SEM results using different supporting materials, the choice of support has played a role in the morphology of the materials and the chemistry of the Fe-species synthesized.

6.2.2. Electrochemical characterization

The next section is going to look at the influence of the different parameters, such as the introduction of FeCl$_3$, the use of Ti$_3$C$_2$ and XC72-R as different supports and the amount of urea in the MXene samples, on the electrochemical activity of the synthesized materials. And whenever possible, the changes in performance are going to be compared with the different physico-chemical properties determined previously.

The electrochemical characterization of the different samples towards ORR were investigated using RDE measurements in air saturated 0.1M KOH electrolyte. Ti$_3$C$_2$-U10-Fe-800, Ti$_3$C$_2$-U50-Fe-800 and C-U50-Fe-800 were tested and compared to 20%Pt/C which is the benchmark catalyst when it comes to testing ORR activity.

6.2.2.1. ORR performance characterization

ORR is the limiting reaction in a fuel cell, due to its sluggish kinetics. Therefore, developing catalyst that have good activity and good stability is of interest. In the case of ORR in alkaline solutions, a wider range of catalyst materials are available to use, due to better ORR kinetics in alkaline media compared to acidic media. Thus, the development of catalyst without platinum group metals is possible when looking for AFC catalyst, such as M-N-C catalyst like Fe-N-C, which is a N-doped carbon support containing Fe-N$_x$ moieties. The synthesized materials are therefore expected to have better ORR performance than Ti$_3$C$_2$-U10-800 and Ti$_3$C$_2$-U50-800.

Linear sweep voltammetry (LSV) has been performed on the different samples to determine their electrochemical properties, such as onset potential (E$_{onset}$), half-wave potential (E$_{1/2}$), the diffusion-limiting current density (j$_L$), as well as some other kinetic properties through Koutecky-Levich and Tafel plots. LSV curves of the different samples were measured in the [0.1;1.1] V (vs RHE) potential range in 0.1 M KOH purged with air and are displayed on Figure 6.13. All the LSVs have been iR and background corrected, as specified in the method section. The current has also been normalized to the geometrical surface area of the working electrode (0.247 cm^2). All the electrochemical characteristics measured and discussed in this section are summarized in Table 6.7.
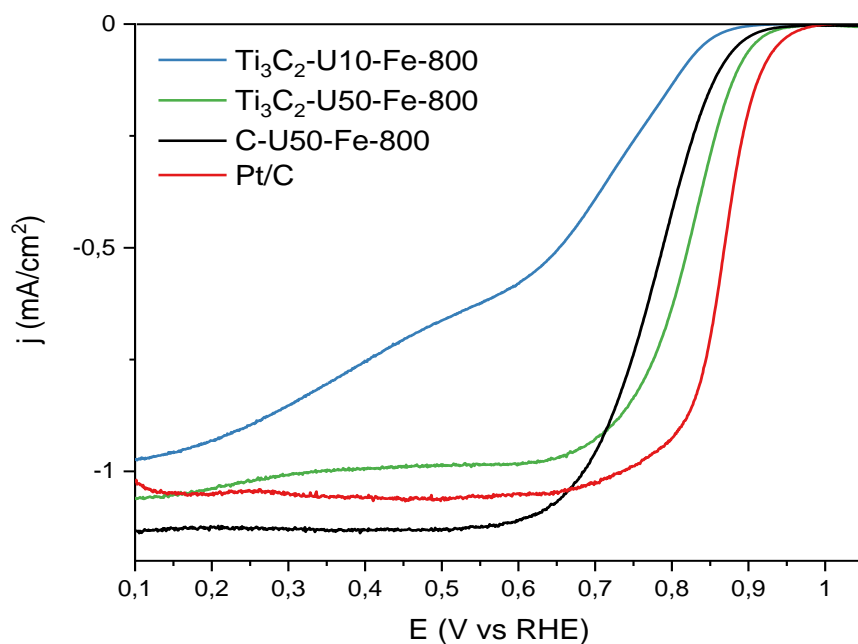
Figure 6.13: LSVs (5 mV.s^{-1}) of the different samples in 0.1M aerated KOH electrolyte (corrected) at 1600 rpm

From the LSV curves performed at 1600 rpm presented in Figure 6.13, it can be seen that for the samples Ti$_3$C$_2$-U50-Fe-800 and C-U50-Fe-800 the ORR has reached mass transport limitation at potentials below 0.6 V vs RHE, while at potential higher than 0.6 V vs RHE the LSV is dictated by a mixed region, where both kinetics and diffusion play a role. In the case of Pt/C the potential at which the mass-transport region is attained is 0.7 V vs RHE owing for better ORR performance. On the other hand, the LSV for Ti$_3$C$_2$-U10-Fe-800, although getting close to theoretical limiting current values, does not reach a plateau at any potential.

The onset potential is a parameter which can give a first idea of how active a catalyst is towards ORR. Indeed, a greater onset potential means that a smaller overpotential is required to overcome the energy needed to start ORR. The E$_{onset}$ measured for the different catalysts are as follows. E$_{onset}$ for Pt/C is the greatest at 0.96 V vs RHE, owing to its incredible activity towards ORR. It can be seen that the onset potential for all three synthesized catalysts Ti$_3$C$_2$-U10-Fe-800, Ti$_3$C$_2$-U50-Fe-800 and C-U50-Fe-800 are lower than Pt/C, at potential values of 0.86, 0.93 and 0.91 V vs RHE respectively. But for both MXene samples, it seems that the introduction of Fe precursor during the synthesis achieved to goal of improving the performance towards ORR, as the onset potentials of both Ti$_3$C$_2$-U10-Fe-800 and Ti$_3$C$_2$-U50-Fe-800 are greater than for Ti$_3$C$_2$-U10-800 and Ti$_3$C$_2$-U50-F800, which were measured to be 0.82 and 0.88 V vs RHE respectively. Moreover, it can be seen that using Ti$_3$C$_2$ as a support has helped improve the onset potential compared to the sample using XC72-R. This could be explained by the fact that the using Ti$_3$C$_2$ as support promoted the formation of Fe-N$_x$ moieties, which have shown to have outstanding electrochemical activity towards ORR, especially when coupled with Fe$_3$C and α-Fe.[176-178,188,189] On the other hand, Ti$_3$C$_2$-U10-Fe-800 also displays a higher content of Fe-N$_x$ compared to C-

U50-Fe-800, but out of all three samples synthesized, Ti_3C_2-U10-Fe-800 is the one with the poorer onset potential. One possibility to explain this could be the difference in morphology of Ti_3C_2-U10-Fe-800, which was the only sample on which didn't grow CNT/CNF like carbonous structures.

Some variation in limiting current density is observable between Ti_3C_2-U50-Fe-800, C-U50-Fe-800 and Pt/C. Based on Levich equation:

$$j_L = 0.201\, n\, F\, C_o\, D_o^{2/3}\, \nu^{-1/6}\, \omega^{1/2}$$

where, j_L is the current density

n is the electron transfer number of the reaction

F is the Faraday's constant

C_o is the concentration of oxygen in solution

D_o is the diffusion coefficient of oxygen in solution

ν is the kinematic viscosity of the electrolyte

ω is the rotation speed of the electrode in rpm

It can be seen that the limiting current density does not depend on the intrinsic properties of the catalyst, except for n, which is the number of electrons exchanged during the reaction. Looking at the LSV graphs, it seems that the Ti_3C_2-U10-Fe-800 could have some mixed ORR processes happening during the electrochemical testing as the LSV displays a two reduction waves, denoted by the shoulder on the LSV at potential 0.6 V vs RHE. This could be indicative of two different active sites which would participate towards ORR at different potentials. Concerning the other samples, which all reached a j_L around the theoretical value for n=4, the observed variations could most likely be due to small defects on the surface of the electrode and/or the non-uniform coating of catalyst on the working electrode surface.

LSV curves done in aerated 0.1 M KOH at different rotation rates for all samples containing Fe species and Pt/C, as well as their corresponding K-L plots, are given in Figure 6.14. The K-L plots show good parallelism and linearity, indicating first-order reaction kinetics. Based on Koutecky-Levich equation, it is possible to determine the electron transfer number. Indeed, the K-L equation relates the current measured to the kinetic current and the limiting current following the equation:

$$\frac{1}{j} = \frac{1}{j_k} + \frac{1}{j_L}$$

By introducing the Levich equation, it gives:

$$\frac{1}{j} = \frac{1}{j_k} + \frac{1}{B_L}\,\omega^{-1/2}$$

$$\text{with } B_L = 0.201\, n\, F\, C_o\, D_o^{2/3}\, v^{-1/6}$$

$1/B_L$ corresponds to the slope of the plot j^{-1} vs $\omega^{-1/2}$ and corresponds to the K-L plot. The calculated electron transfer number for all the samples at potentials 0.4, 0.5, 0.6, 0.7 and 0.8 are given in the legends of the K-L plots (see Figure 6.14). As expected, the sample with the highest electron transfer number is Pt/C, with an average value of 3.91 over the potential used to plot the K-L curves. The samples Ti_3C_2-U50-Fe-800 and C-U50-Fe-800 have a similar electron transfer number of 3.66 and 3.69 on average, respectively. But the evolution of n differs for the two samples, as both show a pretty stable value of n between the potentials 0.4 and 0.7 V vs RHE, but the value of the electron transfer number increases at 0.8 V vs RHE for Ti_3C_2-U50-Fe-800, while it decreased for C-U50-Fe-800. Last of all, Ti_3C_2-U10-Fe-800 displays the lower n value with an average of 2.96, starting at 2.83 at 0.8 V vs RHE and up to 3.33 at 0.4 V vs RHE, which support the fact that two processes may be into play for the ORR.
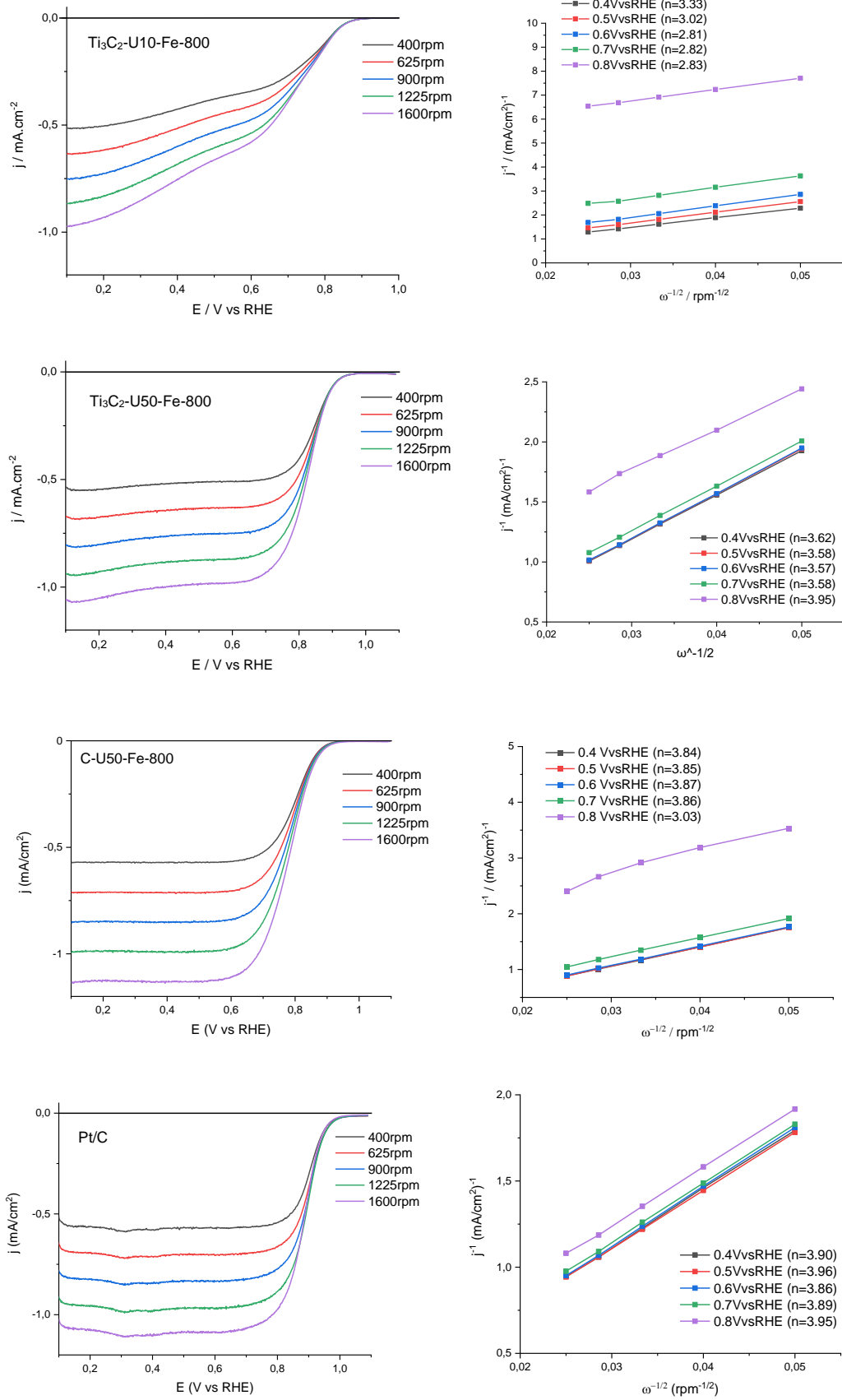
Figure 6.14: Linear sweep voltammograms (5 mV.s⁻¹) of Ti₃C₂-U10-Fe-800, Ti₃C₂-U50-Fe-800, C-U50-Fe-800 and Pt/XC72R (20%wt) at different rotation speed in 0.1 aerated KOH electrolyte. K-L plots at potential between [0.4;0.8] VvsRHE (calculated n given in legend)

Therefore, from the K-L plots, it can be concluded that the samples Ti_3C_2-U50-Fe-800 and C-U50-Fe-800 can catalyse the ORR through an apparent ~4 electron pathway, while ORR on Ti_3C_2-U10-Fe-800 seems to occur with mixed processes. To elucidate some of the mechanisms happening during the ORR experiments, ring-disk rotating electrode measurements have been performed on the different samples. RRDE is a great tool to understand if the ORR is going through a 2e⁻ or a 4e⁻ pathway.
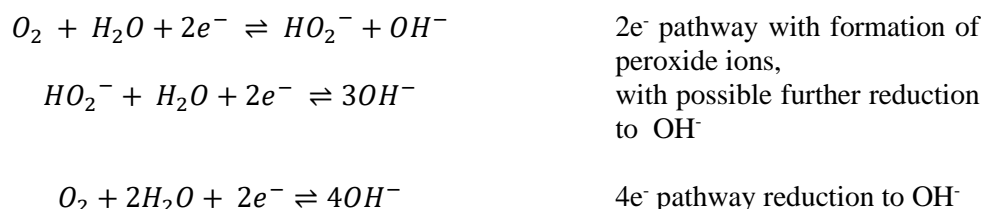
$$O_2 + H_2O + 2e^- \rightleftharpoons HO_2^- + OH^-$$

2e⁻ pathway with formation of peroxide ions,

$$HO_2^- + H_2O + 2e^- \rightleftharpoons 3OH^-$$

with possible further reduction to OH⁻

$$O_2 + 2H_2O + 2e^- \rightleftharpoons 4OH^-$$

4e⁻ pathway reduction to OH⁻

The ring potential was held at 1.3 V vs RHE during oxygen reduction experiments to detect HO_2^- by-products formed during ORR processes going through a 2-electrons ORR pathway. First, the corrected disk and ring current densities measured at 1600 rpm in 0.1 M aerated KOH were measured, then the electron transfer number n and the HO_2^- yield can be determined from the disk and ring current measurements and have been calculated using the following equations, as described in the Materials and Methods chapter.

$$n = \frac{4I_d N}{I_d N + I_r}$$

$$\%H_2O_2 = 100\frac{2I_r N}{I_d N + I_r}$$

The RRDE measurements, as well as the calculated peroxide yield and electron transfer number are given in Figure 6.15. The RRDE of Pt/C is characteristic, with a slight increase of j_{ring} at lower potential. The peroxide formation is below 10% throughout the potential window and the calculated transfer number ranges between 3.8 and 3.9, which is supporting the previously calculated n using K-L plots. Thus, it is clear that Pt/C materials catalyses the ORR through a 4e⁻ process in majority. In the case of C-U50-Fe-800, the evolution of j_r is very similar to Pt/C, the ring current density barely increases at lower potentials, which yields a small amount of peroxide during the testing. The electron transfer number also ranges around 3.8 and 3.9 for this sample, which is close to the values deducted from K-L. Ti_3C_2-U50-Fe-800 displays a ring current density which increases slightly more than the two previous samples around 0.4 V vs RHE. The electron transfer number is evaluated at around 3.8 using RRDE for Ti_3C_2-U50-Fe-800, which is higher than the value of 3.66, but is still reasonably within error. Out of all the samples, only Ti_3C_2-U10-Fe-800, shows a noticeable increase in j_r during the first reduction wave, owning to peroxide

formation. The ring current density then decreases during the second reduction wave of the LSV. This shows that the ORR reaction on the surface of Ti_3C_2-U10-Fe-800 happens through a 2e⁻ pathway forming peroxide that could be detected on the ring but would be further reduced to OH⁻ at lower potential. The most surprising aspect here is that the calculated electron transfer number is a lot higher than the one deduced from K-L curves, going from 3.4 at 0.8 V vs RHE to 3.9 at 0.1 V vs RHE. This phenomenon could not be explained, but some studies have shown that both K-L and RRDE methods both have limitations when it comes to the determination of the apparent electron transfer number.[190]
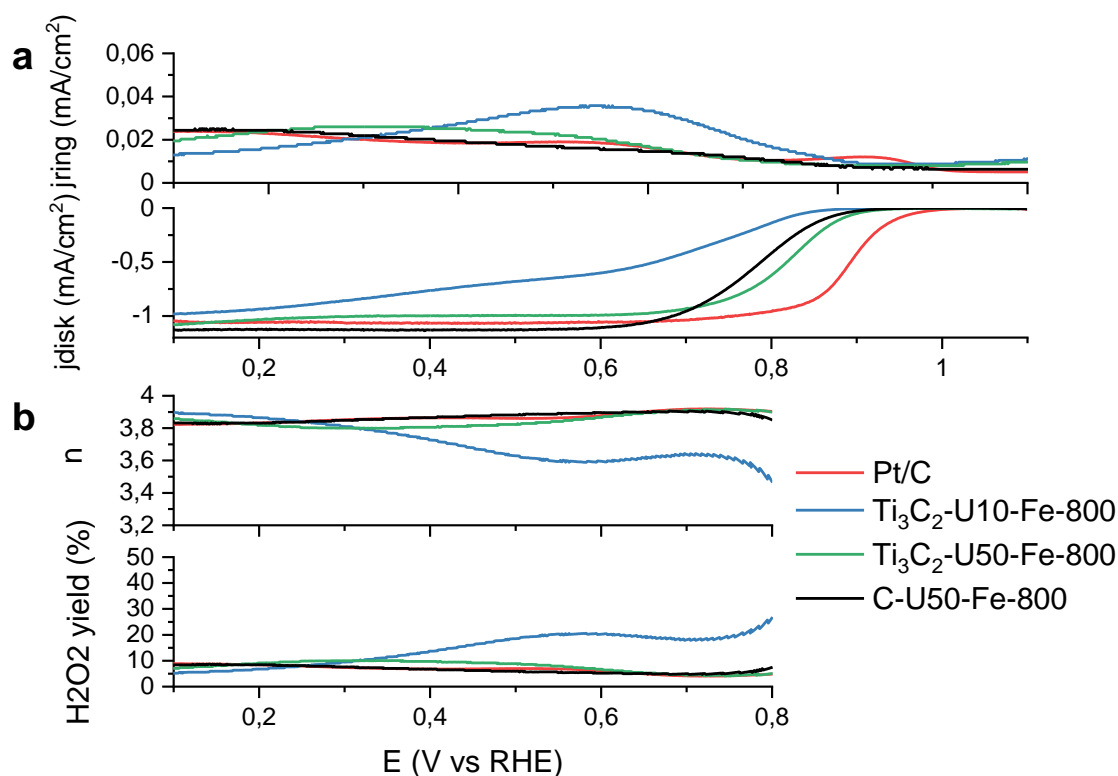
Figure 6.15: RRDE measurements of the different Ti3C2-Ux-Fe-800 samples, C-U50-Fe-800 and Pt/C in 0.1M aerated KOH electrolyte (corrected) at 1600 rpm and scan rate of 5mV.s⁻¹: (a) jdisk and jring , (b) calculated HO2- yield and electron-transfer number

Now that the onset potential, as well as the electron transfer number have been determined, it would be interesting to have a look at the kinetics of the ORR when catalysed with the different materials. Tafel plots are displayed in Figure 6.16 and compared to the benchmark Pt/C catalyst. The Tafel curves of all catalyst show two slopes, one in the higher potential (lower overpotential) region and another one in the lower potential (higher overpotential) region. The region of interest, when looking at the kinetics of reaction for a catalyst is the lower overpotential region, as a minor change in potential can induce a drastic variation in current density. The slope of the Tafel plot is a great tool to evaluate the ORR kinetics on a catalyst and helps comparison between different catalysts. The calculated Tafel slopes are given in Table 6.7. First of all, value of Tafel slope

obtained for Pt/C is 61 mV/dec for the low j_k region, which is characteristic for commercial Pt/C catalysts.[26] The Tafel slopes of the other samples are as follows: 66, 73 and 89 for Ti_3C_2-U50-Fe-800, C-U50-Fe-800 and Ti_3C_2-U10-Fe-800 respectively. These results shows that the kinetics of ORR on Ti_3C_2-U50-Fe-800 are the best out of the materials synthesized, while Ti_3C_2-U10-Fe-800 shows poorer kinetics.
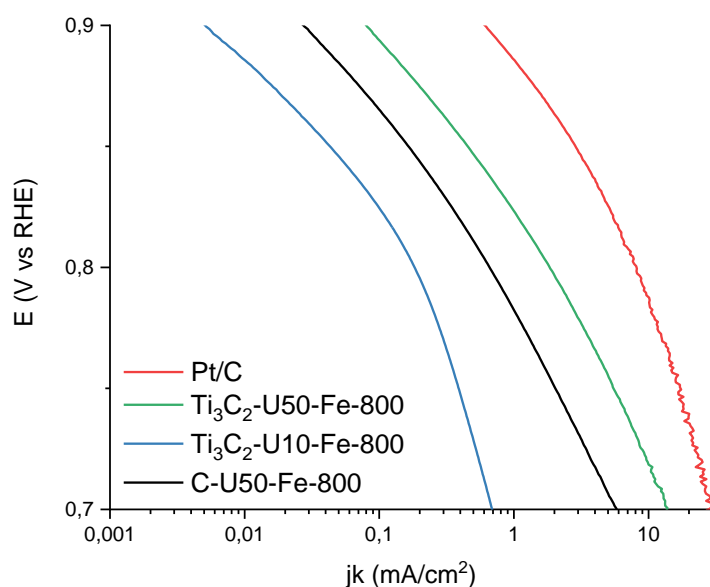
Figure 6.16: Tafel plots of Ti₃C₂-U10-Fe-800, Ti₃C₂-U50-Fe-800 and Pt/XC72R (20%wt)

The kinetic current densities j_k at 0.85 and 0.9 V vs RHE have been calculated and given in Table 6.7. It is clearly visible from the j_k values of 3.02 and 0.61 mA.cm^{-2} that Pt/C is the most active towards ORR. It can be seen that, by comparing Ti_3C_2-U50-Fe-800 and C-U50-Fe-800, that the presence of the MXene as support, has permitted to more than double the values of j_k at both 0.85 and 0.9 V vs RHE, definitely showing that Ti_3C_2-U50-Fe-800 has a better activity towards ORR than C-U50-Fe-800. Based on previous physico-chemical characterisation, this improvement towards ORR is most likely owed to the fact that the presence of the MXene, by interacting with the different precursors, has allowed for the formation of a greater number of Fe-N$_x$ moieties on Ti_3C_2-U50-800 compared to C-U50-Fe-800. Moreover, previous studies have showed that MXenes can also interact with compounds which have been deposited on, leading to greater ORR activity compared to the materials without MXene support.[110,113,123] On the other hand, the MXene sample, which was prepared with a lesser quantity of urea, is showing poor activity towards ORR, with j_k values of 0.04 and 0.005 at 0.85 and 0.9 V vs RHE respectively. Based on the previous Mössbauer measurements, it can be seen that Ti_3C_2-U10-Fe-800 has a slightly lower amount of Fe-N$_x$ comparatively to Ti_3C_2-U50-Fe-800, but still higher than C-U50-Fe-800. The possible

explanations for this difference in activity between the MXene samples may be the overall higher nitrogen content of Ti_3C_2-U50-800 compared to Ti_3C_2-U10-800 (see EDS and XPS nitrogen content measurements), providing more pyridinic N active sites towards ORR.[191] Thus, it can be seen that the presence of MXene alone as support is not the only factor to consider when synthesizing the materials.

Table 6.7: Summary of electrochemical properties in air saturated 0.1M KOH electrolyte

	E_{onset} (V vs RHE)	j_k at 0.85 mA.cm$_{disk}^{-2}$ (mA.cm^{-2})	j_k at 0.9 mA.cm$_{disk}^{-2}$ (mA.cm^{-2})	n (K-L)	Tafel slope (mV/dec)
Ti_3C_2-U10-Fe-800	0.86	0.04	0.005	2.96	89
Ti_3C_2-U50-Fe-800	0.93	0.47	0.08	3.66	66
C-U50-Fe-800	0.91	0.17	0.03	3.69	73
Pt/C	0.96	3.02	0.61	3.91	61

Overall, the different ORR performance indicators of the different samples seem to follow this trend: Pt/C > Ti_3C_2-U50-Fe-800 > C-U50-Fe-800 > Ti_3C_2-U10-Fe-800. Based on the physico chemical characterisation of the materials, most of the improvement in ORR performance of Ti_3C_2-U50-Fe-800 compared to the other two materials synthesized is due to:

- A higher nitrogen content, which favourably formed pyridinic N species (see deconvolution of XPS N1s spectra). Pyridinic N is well known to improve ORR activity compared to other carbonous N species.
- The choice of support materials. Indeed, based on SEM and Mössbauer results, it seems that the MXene have interacted with the Fe precursor and allowed some spatial confinement during the synthesis, restricting the agglomeration of Fe particles during thermal treatment and allowing for more Fe-N_x species to form.

6.2.2.2. Stability testing

Stability of a catalyst is a very important parameter to test, as it will determine how quickly the catalyst will degrade and therefore its lifetime. Stability and degradation studies are usually done by comparing the catalyst performance before and after cycling. Cycling of the materials is done through an ADT (Accelerated Durability Test). In this work ADT was performed by cycling the different samples between [0.5;1] V (vs RHE) for 2000 cycles sweeping at 50 mV.s-1 rate. The LSV measurements were performed post-cycling and compared to the pre-cycling LSVs. The pre- and post-cycling LSVs of the different samples are given in Figure 6.17.

.

As expected, all post-cycling LSVs show similar onset potential compared to the pre-cycling LSV, but cycling has shifted the kinetic region of the curve toward lower potentials, which is a sign that degradation has happened in the catalyst materials. A good way to evaluate the amount of degradation of a catalyst is to measure the shift of the half-wave potential of the LSV curve after the ADT compared to the pristine sample. The sample with the less degradation overall is the Pt/C, by displaying a $\Delta E_{1/2}$ of 16 mV. The half-wave potential shifts after ADT are more consequent for the Fe containing materials. The $\Delta E_{1/2}$ are 85, 37 and 47 mV for Ti_3C_2-U10-Fe-800, Ti_3C_2-U50-Fe-800 and C-U50-Fe-800 respectively.
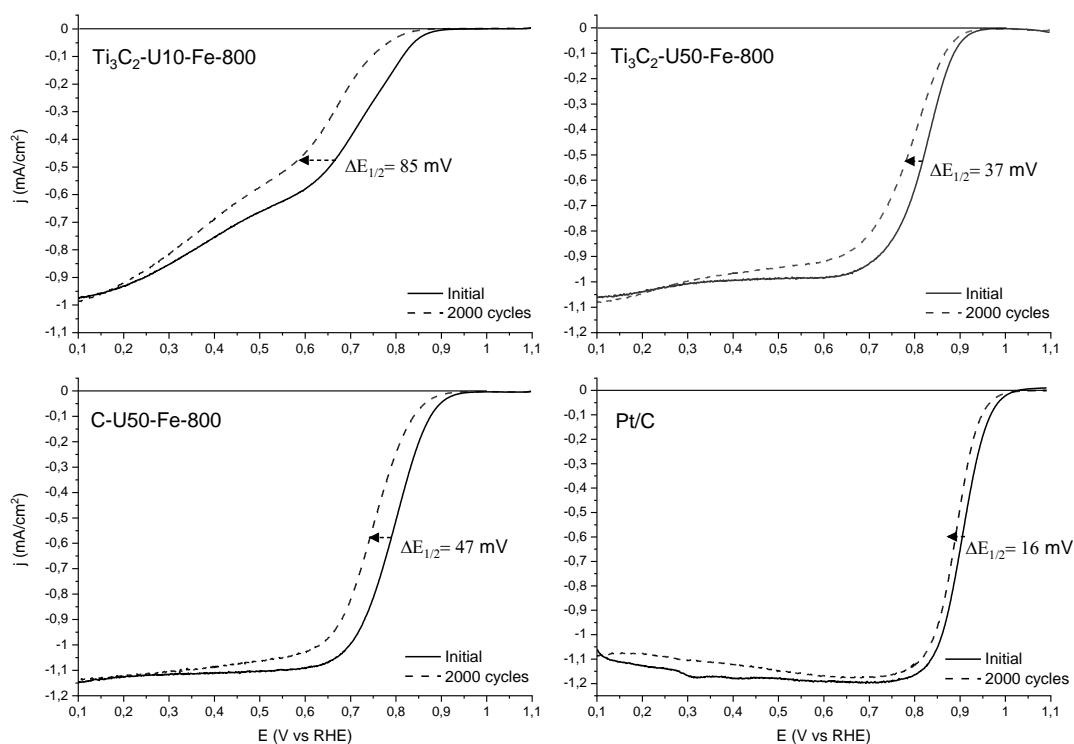
Figure 6.17: LSVs before and after cycling between [0.5;1] VvsRHE of the different support materials: (a) Ti_3C_2-U10-Fe-800p and (b) Ti_3C_2-U50-Fe-800. The electrolyte used is a 0.1M aerated KOH solution.

6.3. Conclusion

The approach of introducing Fe-containing precursor with the MXene and the urea before thermal treatment has shown to succeed on several aspects that needed to be improved based on the results of the previous chapters. Indeed, both Ti_3C_2-U10-Fe-800 and Ti_3C_2-U50-Fe-800 have shown a drastic increased in term of activity towards ORR compared to the samples which were prepared previously without $FeCl_3$. The overall activity towards ORR for the different samples prepared in this chapter are as follow: Ti_3C_2-U50-Fe-800 > C-U50-Fe-800 > Ti_3C_2-U10-Fe-800.

Based on the physico-chemical characterisation of the samples, several aspects have found to have an impact on this increase in activity.

First, the surface area of both Ti_3C_2-U10-Fe-800 and Ti_3C_2-U50-Fe-800 have increased, going from 24.4 and 38.4 $m^2.g^{-1}$ for their Fe-free homologues, to 178.5 and 124.1$cm^2.g^{-1}$ respectively. This was explained by the presence of Fe species, which allowed for more urea decomposition product to react and form carbonous species on the surface of the MXenes. XRD measurement supports this with the apparition of the (002) graphitic carbon peak at 26° 2θ. Moreover, the XPS spectra show an increased content of C on the surface of the materials compared to the samples Ti_3C_2-U10-800 and Ti_3C_2-U50-800. Based on SEM, it seems that the quantity of urea added during the synthesis has an influence on the morphology of the materials. Indeed, the sample containing more urea has shown to have grown CNT/CNF structures on the surface of the MXene flakes, while no CNT/CNF seems to have formed if the urea amount is too low. Based on literature, The CNT/CNF growth is most likely catalyzed by the presence of Fe species such as α-Fe and Fe_3C.[179]

The use of Ti_3C_2 as support has a positive impact on the ORR activity of the final material. This could be explained by the higher quantity of Fe-N_x formed during the synthesis when Ti_3C_2 was used as a support, while when the support was change to XC72-R the Fe-N_x content dropped. Therefore, the MXene layers must have played a role during the synthesis. The main hypothesis is that the MXene must have restricted the aggregation of Fe into α-Fe and Fe_3C during the thermal treatment, allowing the formation of the Fe-N_x moieties, by either interacting with the $FeCl_3$ precursor or by providing a steric restriction once the ions have been intercalated. SEM pictures seem to support this, as qualitatively, the particles sizes of the Fe species visible seem to be smaller for Ti_3C_2-U50-Fe-800 compared to C-U50-Fe-800.

CHAPTER 7: Conclusion and future work

7.1. Conclusions

This thesis mainly focused on using Ti_3C_2 MXenes as support / co-catalyst for oxygen reduction reaction in alkaline media. While MXenes have shown some potential as support for Pt nanoparticles with great activity toward ORR in acidic and alkaline media, their low specific surface area is a significant drawback both for catalyst deposition and electrochemical performance.

The first approach of this thesis was to intercalate nitrogen precursors between MXene layers before further thermal treatment. The main objectives were to dope Ti_3C_2 with nitrogen while forming carbonaceous decomposition compounds between layers to hinder the layer restacking of the MXene during the thermal treatment. After an intercalation experiment with several nitrogen precursors, urea has been found to effectively intercalate between MXene layers, resulting in a more homogeneous distribution of MXene in the sample. Additionally, the introduction of urea leads to an increase in the interlayer spacing of intercalated MXene samples, as indicated by X-ray diffraction measurements. This effect is observed even after the samples undergo thermal treatment at 550°C and 800°C. The increase in interlayer spacing has been attributed to the presence of urea decomposition products on the surface of the MXene layers, which serve as pillars which prevent the MXene layers from restacking during thermal treatment. This results in an increase in the surface area of the MXene samples, with values of 12.8, 21.2, and 80.1 $m^2.g^{-1}$ for samples treated at 550°C and values of 23.4 and 38.4 $m^2.g^{-1}$ for samples treated at 800°C. Moreover, the chemical characterization techniques have shown the successful nitrogen doping of the MXene, as well as the presence of carbonaceous species on their surface.

The electrochemical characterization of the samples was then performed in aerated 0.1 M KOH electrolyte. First as a reference Ti_3C_2 was tested. It had limited oxygen reduction reaction (ORR) performance due to its low intrinsic ORR properties and small surface area of 9.5 $m^2.g^{-1}$. It was found that the addition of N-C species to the MXene surface improved the overall ORR performance of the materials compared to Ti_3C_2. This is thought to be due to interactions between the decomposition products of the urea and the MXene surface. For samples treated at 550°C, the ORR performance increased with increasing amounts of urea, with the exception of the sample with the highest urea content (1:50), which had worse performance due to the synthesis of excess g-C_3N_4. The second thermal treatment at 800°C further improved the ORR activity of the urea-treated samples, particularly for the sample with the highest urea content (Ti_3C_2-U50-800), which

showed a drastic improvement in performance. This second treatment may have improved the overall electrochemical stability of the prepared samples by strengthening the interaction between the N-C compound and the MXene, providing more stability to the heterostructure.

Although the activities towards ORR of the synthesized materials had shown an improvement, the performance of the different materials were far from the Pt/C benchmark. Indeed, the previously designed catalysts still had a lower specific surface areas and intrinsic ORR activities compared to Pt/C. Therefore, another approach was then considered to improve the materials based on the addition of an additional precursor during the synthesis process, which would help increase the specific surface area, as well as the ORR activity, of the MXene-based materials. To do so, $FeCl_3$ was chosen as Fe precursor. The objective is for the Fe precursor to catalyze and react with the urea decomposition products to form additional carbon species on the MXenes, as well as forming Fe and Fe-N-C species, which are known to have good ORR activities in alkaline media. The introduction of $FeCl_3$ along with urea and MXenes has proven to be effective in improving several aspects of the materials. Both Ti_3C_2-U10-Fe-800 and Ti_3C_2-U50-Fe-800 show a significant increase in ORR activity compared to the previous samples. Several factors have been found to contribute to this increase in activity based on the physicochemical characterization of the samples. Firstly, the surface area of both Ti_3C_2-U10-Fe-800 and Ti_3C_2-U50-Fe-800 has increased to 178.5 and 124.1 $m^2.g^{-1}$, respectively. This is believed to be due to the presence of Fe species, which allowed for more urea decomposition products to react and form carbonous species on the surface of the MXenes. X-ray diffraction measurements support this, showing the appearance of the (002) graphitic carbon peak. XPS also show an increase in the content of C on the surface of the. Scanning electron microscopy images suggested that carbonaceous species such as CNT and SNF have formed on the different samples. It is believed that the CNT/CNF growth is likely catalyzed by the presence of Fe species such as α-Fe and Fe_3C. Moreover, using the MXene as a support has a positive impact on the ORR activity of the final material. This may be due to the higher quantity of Fe-Nx formed during synthesis when Ti_3C_2 is used as a support, while using a XC72-R as support led to a decrease in Fe-Nx content. The overall ORR activity for the different samples prepared in this study is as follows: Ti_3C_2-U50-Fe-800 > C-U50-Fe-800 > Ti_3C_2-U10-Fe-800.

To summarize, the aims and objectives fixed have been achieved:

- A porous and stable MXene-based structure has been synthesized through intercalation of urea into MXene layers before annealing.
- The different samples have been characterized and the influence of urea content, as well as the annealing temperature, has been investigated.
- The samples were then tested as catalyst towards ORR. An overall increase in ORR performance was achieved for the treated samples.

- Improvement of the synthesis process has been achieved based on previous results. A novel method combining urea as N/C precursor and $FeCl_3$ as Fe precursor mixed with Ti_3C_2, used as backbone, led to the synthesis of α-Fe/Fe_3C/Fe-N_X species on a N-carbon/N-Ti_3C_2 support, which displayed promising ORR performance.

7.2. Future work

This thesis was focused on the synthesis of Ti_3C_2-based materials for ORR application, with a focus on increasing the specific surface area of the materials as well as improving the intrinsic catalytic activity towards ORR. Based on the different results presented previously, the following suggesting could be considered for future work:

- The MXene family has a wide range of chemistries available, but the most studied MXene is Ti_3C_2. Other chemistries may be a better fit for electrochemical and ORR applications. Therefore, a study of a wider range of chemistries is suggested, which also could lead to a better general understanding of MXene properties.
- The nitrogen precursor, which was selected, is urea. A lot of other precursors are available, some of them, with longer carbon chains, could provide a better support once intercalated, and serve as pillars. Due to their flake morphology, intercalation approaches similar to the ones used with clays could be considered.
- The Fe-containing samples have been tested in a 3-electrodes setup using the RDE method. Although it gives a good idea of ORR performance of a materials, the conditions in a real fuel cell, especially the degradation mechanisms, are very different. Therefore, testing these materials in AFC conditions would be beneficial.
- The method described in the last result chapter could be exploited with other types of catalysts precursors.

REFERENCES

1   Ryan O'Hayre, S.-W. C., Whitney G. Colella, Fritz B. Prinz. *Fuel Cell Fundamentals*. Third Edition edn, (Wiley, 2016).

2   Badwal, S. P. S., Giddey, S. S., Munnings, C., Bhatt, A. I. & Hollenkamp, A. F. Emerging electrochemical energy conversion and storage technologies. *Frontiers in Chemistry* **2** (2014). https://doi.org:10.3389/fchem.2014.00079

3   Thomas, B. R. *Linden's Handbook of Batteries, Fourth Edition*. 4th ed. edn, (McGraw-Hill Education, 2011).

4   Liang, Y. *et al.* A review of rechargeable batteries for portable electronic devices. *InfoMat* **1**, 6-32 (2019). https://doi.org:https://doi.org/10.1002/inf2.12000

5   Liang, Y., Dong, H., Aurbach, D. & Yao, Y. Current status and future directions of multivalent metal-ion batteries. *Nature Energy* **5**, 646-656 (2020). https://doi.org:10.1038/s41560-020-0655-0

6   Kubota, K., Dahbi, M., Hosaka, T., Kumakura, S. & Komaba, S. Towards K-Ion and Na-Ion Batteries as "Beyond Li-Ion". *The Chemical Record* **18**, 459-479 (2018). https://doi.org:https://doi.org/10.1002/tcr.201700057

7   Rahman, M. A., Wang, X. & Wen, C. High Energy Density Metal-Air Batteries: A Review. *Journal of The Electrochemical Society* **160**, A1759-A1771 (2013). https://doi.org:10.1149/2.062310jes

8   Cheng, F. Y. & Chen, J. Metal-air batteries: from oxygen reduction electrochemistry to cathode catalysts. *Chem. Soc. Rev.* **41**, 2172-2192 (2012). https://doi.org:10.1039/c1cs15228a

9   Zhang, X., Wang, X.-G., Xie, Z. & Zhou, Z. Recent progress in rechargeable alkali metal–air batteries. *Green Energy & Environment* **1**, 4-17 (2016). https://doi.org:https://doi.org/10.1016/j.gee.2016.04.004

10   Weber, A. Z. *et al.* Redox flow batteries: a review. *Journal of Applied Electrochemistry* **41**, 1137 (2011). https://doi.org:10.1007/s10800-011-0348-2

11   González, A., Goikolea, E., Barrena, J. A. & Mysyk, R. Review on supercapacitors: Technologies and materials. *Renewable and Sustainable Energy Reviews* **58**, 1189-1206 (2016). https://doi.org:https://doi.org/10.1016/j.rser.2015.12.249

12   Hoogers, G. *Fuel Cell Technology Handbook*. (CRC Press, 2003).

13   Winter, M. & Brodd, R. J. What Are Batteries, Fuel Cells, and Supercapacitors? *Chemical Reviews* **104**, 4245-4270 (2004). https://doi.org:10.1021/cr020730k

14   Gülzow, E. & Schulze, M. Long-term operation of AFC electrodes with CO2 containing gases. *Journal of Power Sources* **127**, 243-251 (2004). https://doi.org:https://doi.org/10.1016/j.jpowsour.2003.09.020

15   McLean, G. F., Niet, T., Prince-Richard, S. & Djilali, N. An assessment of alkaline fuel cell technology. *International Journal of Hydrogen Energy* **27**, 507-526 (2002). https://doi.org:https://doi.org/10.1016/S0360-3199(01)00181-1

16   Walkowiak-Kulikowska, J., Wolska, J. & Koroniak, H. in *10. Polymers application in proton exchange membranes for fuel cells (PEMFCs):*   (eds Tylkowski Bartosz, Wieszczycka Karolina, & Jastrzab Renata) 293-348 (De Gruyter, 2017).

17   Chandan, A. *et al.* High temperature (HT) polymer electrolyte membrane fuel cells (PEMFC) – A review. *Journal of Power Sources* **231**, 264-278 (2013). https://doi.org:https://doi.org/10.1016/j.jpowsour.2012.11.126

18   Wu, L., Xu, T. & Yang, W. Fundamental studies of a new series of anion exchange membranes: Membranes prepared through chloroacetylation of poly(2,6-dimethyl-1,4-

phenylene oxide) (PPO) followed by quaternary amination. *Journal of Membrane Science* **286**, 185-192 (2006). https://doi.org:https://doi.org/10.1016/j.memsci.2006.09.035

19   Zhang, Z., Xiao, X., Yan, X., Liang, X. & Wu, L. Highly conductive anion exchange membranes based on one-step benzylation modification of poly(ether ether ketone). *Journal of Membrane Science* **574**, 205-211 (2019). https://doi.org:https://doi.org/10.1016/j.memsci.2018.12.080

20   Zhang, H.-W., Chen, D.-Z., Xianze, Y. & Yin, S.-B. Anion-Exchange Membranes for Fuel Cells: Synthesis Strategies, Properties and Perspectives. *Fuel Cells* **15**, 761-780 (2015). https://doi.org:https://doi.org/10.1002/fuce.201500039

21   Hren, M., Božič, M., Fakin, D., Kleinschek, K. S. & Gorgieva, S. Alkaline membrane fuel cells: anion exchange membranes and fuels. *Sustainable Energy & Fuels* **5**, 604-637 (2021). https://doi.org:10.1039/D0SE01373K

22   Mahato, N., Banerjee, A., Gupta, A., Omar, S. & Balani, K. Progress in material selection for solid oxide fuel cell technology: A review. *Progress in Materials Science* **72**, 141-337 (2015). https://doi.org:https://doi.org/10.1016/j.pmatsci.2015.01.001

23   Choudhury, A., Chandra, H. & Arora, A. Application of solid oxide fuel cell technology for power generation—A review. *Renewable and Sustainable Energy Reviews* **20**, 430-442 (2013). https://doi.org:https://doi.org/10.1016/j.rser.2012.11.031

24   Ivers-Tiffée, E., Weber, A. & Herbstritt, D. Materials and technologies for SOFC-components. *Journal of the European Ceramic Society* **21**, 1805-1811 (2001). https://doi.org:https://doi.org/10.1016/S0955-2219(01)00120-0

25   Kirubakaran, A., Jain, S. & Nema, R. K. A review on fuel cell technologies and power electronic interface. *Renewable and Sustainable Energy Reviews* **13**, 2430-2440 (2009). https://doi.org:https://doi.org/10.1016/j.rser.2009.04.004

26   Ge, X. *et al.* Oxygen Reduction in Alkaline Media: From Mechanisms to Recent Advances of Catalysts. *ACS Catal.* **5**, 4643-4667 (2015). https://doi.org:10.1021/acscatal.5b00524

27   Bidault, F., Brett, D. J. L., Middleton, P. H. & Brandon, N. P. Review of gas diffusion cathodes for alkaline fuel cells. *Journal of Power Sources* **187**, 39-48 (2009). https://doi.org:https://doi.org/10.1016/j.jpowsour.2008.10.106

28   Liang, Y. *et al.* Co3O4 Nanocrystals on Graphene as a Synergistic Catalyst for Oxygen Reduction Reaction. *Nat. Mater.* **10**, 780 (2011).

29   Jia, Q. *et al.* Metal and Metal Oxide Interactions and Their Catalytic Consequences for Oxygen Reduction Reaction. *Journal of the American Chemical Society* **139**, 7893-7903 (2017). https://doi.org:10.1021/jacs.7b02378

30   Jäger, R., Härk, E., Kasatkin, P. E. & Lust, E. Investigation of a Carbon-Supported Pt Electrode for Oxygen Reduction Reaction in 0.1M KOH Aqueous Solution. *Journal of The Electrochemical Society* **161**, F861 (2014). https://doi.org:10.1149/2.0491409jes

31   Perez, J., Gonzalez, E. R. & Ticianelli, E. A. Oxygen electrocatalysis on thin porous coating rotating platinum electrodes. *Electrochim. Acta* **44**, 1329-1339 (1998). https://doi.org:https://doi.org/10.1016/S0013-4686(98)00255-2

32   Geniès, L., Faure, R. & Durand, R. Electrochemical reduction of oxygen on platinum nanoparticles in alkaline media. *Electrochim. Acta* **44**, 1317-1327 (1998). https://doi.org:https://doi.org/10.1016/S0013-4686(98)00254-0

33   Campos-Roldán, C. A., Calvillo, L., Granozzi, G. & Alonso-Vante, N. Alkaline hydrogen electrode and oxygen reduction reaction on PtxNi nanoalloys. *Journal of Electroanalytical Chemistry* **857**, 113449 (2020). https://doi.org:https://doi.org/10.1016/j.jelechem.2019.113449

34   Jiang, L., Hsu, A., Chu, D. & Chen, R. Oxygen Reduction Reaction on Carbon Supported Pt and Pd in Alkaline Solutions. *Journal of The Electrochemical Society* **156**, B370 (2009). https://doi.org:10.1149/1.3058586

35   Lu, F. *et al.* Surface Proton Transfer Promotes Four-Electron Oxygen Reduction on Gold Nanocrystal Surfaces in Alkaline Solution. *Journal of the American Chemical Society* **139**, 7310-7317 (2017). https://doi.org:10.1021/jacs.7b01735

36   Erikson, H., Sarapuu, A. & Tammeveski, K. Oxygen Reduction Reaction on Silver Catalysts in Alkaline Media: a Minireview. *ChemElectroChem* **6**, 73-86 (2019). https://doi.org:https://doi.org/10.1002/celc.201800913

37   Rocha, I. M. *et al.* N-doped Carbon Nanotubes for the Oxygen Reduction Reaction in Alkaline Medium: Synergistic Relationship between Pyridinic and Quaternary Nitrogen. *ChemistrySelect* **1**, 2522-2530 (2016). https://doi.org:https://doi.org/10.1002/slct.201600615

38   Zhao, S. *et al.* Tunable Ternary (N, P, B)-Doped Porous Nanocarbons and Their Catalytic Properties for Oxygen Reduction Reaction. *ACS Appl. Mater. Interfaces* **6**, 22297-22304 (2014). https://doi.org:10.1021/am506284k

39   Wang, Y.-X. *et al.* Surface-engineered N-doped carbon nanotubes with B-doped graphene quantum dots: Strategies to develop highly-efficient noble metal-free electrocatalyst for online-monitoring dissolved oxygen biosensor. *Carbon* **186**, 406-415 (2022). https://doi.org:https://doi.org/10.1016/j.carbon.2021.10.027

40   Borghei, M. *et al.* Porous N,P-doped carbon from coconut shells with high electrocatalytic activity for oxygen reduction: Alternative to Pt-C for alkaline fuel cells. *Applied Catalysis B: Environmental* **204**, 394-402 (2017). https://doi.org:https://doi.org/10.1016/j.apcatb.2016.11.029

41   Li, W., Yang, D., Chen, H., Gao, Y. & Li, H. Sulfur-doped carbon nanotubes as catalysts for the oxygen reduction reaction in alkaline medium. *Electrochim. Acta* **165**, 191-197 (2015). https://doi.org:https://doi.org/10.1016/j.electacta.2015.03.022

42   Liu, B., Huang, B., Lin, C., Ye, J. & Ouyang, L. Porous carbon supported Fe-N-C composite as an efficient electrocatalyst for oxygen reduction reaction in alkaline and acidic media. *Appl. Surf. Sci.* **411**, 487-493 (2017). https://doi.org:https://doi.org/10.1016/j.apsusc.2017.03.150

43   Shah, S. S. A. *et al.* Exploring Fe-Nx for Peroxide Reduction: Template-Free Synthesis of Fe-Nx Traumatized Mesoporous Carbon Nanotubes as an ORR Catalyst in Acidic and Alkaline Solutions. *Chemistry – A European Journal* **24**, 10630-10635 (2018). https://doi.org:https://doi.org/10.1002/chem.201802453

44   Li, B. *et al.* Fe-N4 complex embedded free-standing carbon fabric catalysts for higher performance ORR both in alkaline & acidic media. *Nano Energy* **56**, 524-530 (2019). https://doi.org:https://doi.org/10.1016/j.nanoen.2018.11.054

45   Mufundirwa, A. *et al.* Durability of template-free Fe-N-C foams for electrochemical oxygen reduction in alkaline solution. *Journal of Power Sources* **375**, 244-254 (2018). https://doi.org:https://doi.org/10.1016/j.jpowsour.2017.07.025

46   Huang, D., Zhang, B., Li, S., Wang, M. & Shen, Y. Mn3O4/Carbon Nanotube Nanocomposites as Electrocatalysts for the Oxygen Reduction Reaction in Alkaline Solution. *ChemElectroChem* **1**, 1531-1536 (2014). https://doi.org:https://doi.org/10.1002/celc.201402052

47   Zhao, S., Rasimick, B., Mustain, W. & Xu, H. Highly durable and active Co3O4 nanocrystals supported on carbon nanotubes as bifunctional electrocatalysts in alkaline media. *Applied Catalysis B: Environmental* **203**, 138-145 (2017). https://doi.org:https://doi.org/10.1016/j.apcatb.2016.09.048

48   Sunarso, J., Torriero, A. A. J., Zhou, W., Howlett, P. C. & Forsyth, M. Oxygen Reduction Reaction Activity of La-Based Perovskite Oxides in Alkaline Medium: A Thin-Film Rotating Ring-Disk Electrode Study. *The Journal of Physical Chemistry C* **116**, 5827-5834 (2012). https://doi.org:10.1021/jp211946n

49   Wang, H. *et al.* Cation Deficiency Tuning of LaCoO3 Perovskite as Bifunctional Oxygen Electrocatalyst. *ChemCatChem* **12**, 2768-2775 (2020). https://doi.org:https://doi.org/10.1002/cctc.201902392

50   Sakthivel, M., Bhandari, S. & Drillet, J.-F. On Activity and Stability of Rhombohedral LaNiO3 Catalyst towards ORR and OER in Alkaline Electrolyte. *ECS Electrochemistry Letters* **4**, A56 (2015). https://doi.org:10.1149/2.0081506eel

51   Novoselov, K. S. *et al.* Electric Field Effect in Atomically Thin Carbon Films. *Science* **306**, 666 (2004). https://doi.org:10.1126/science.1102896

52   Song, L. *et al.* Large Scale Growth and Characterization of Atomic Hexagonal Boron Nitride Layers. *NANO LETTERS* **10**, 3209-3215 (2010). https://doi.org:10.1021/nl1022139

53   Ma, R. Z. & Sasaki, T. Nanosheets of Oxides and Hydroxides: Ultimate 2D Charge-Bearing Functional Crystallites. *ADVANCED MATERIALS* **22**, 5082-5104 (2010). https://doi.org:10.1002/adma.201001722

54   Chhowalla, M. *et al.* The chemistry of two-dimensional layered transition metal dichalcogenide nanosheets. *Nature Chemistry* **5**, 263-275 (2013). https://doi.org:10.1038/nchem.1589

55   Zhang, J., Chen, Y. & Wang, X. Two-dimensional covalent carbon nitride nanosheets: synthesis, functionalization, and applications. *Energy & Environmental Science* **8**, 3092-3108 (2015). https://doi.org:10.1039/C5EE01895A

56   Geim, A. K. & Grigorieva, I. V. Van der Waals heterostructures. *Nature* **499**, 419-425 (2013). https://doi.org:10.1038/nature12385

57   Novoselov, K. S., Mishchenko, A., Carvalho, A. & Neto, A. H. C. 2D materials and van der Waals heterostructures. *Science* **353** (2016). https://doi.org:10.1126/science.aac9439

58   Naguib, M. *et al.* Two-Dimensional Nanocrystals Produced by Exfoliation of Ti3AlC2. *Advanced Materials* **23**, 4248-4253 (2011). https://doi.org:10.1002/adma.201102306

59   Lei, J.-C., Zhang, X. & Zhou, Z. Recent advances in MXene: Preparation, properties, and applications. *Frontiers of Physics* **10**, 276-286 (2015). https://doi.org:10.1007/s11467-015-0493-x

60   Xiong, D., Li, X., Bai, Z. & Lu, S. Recent Advances in Layered Ti3C2Tx MXene for Electrochemical Energy Storage. *Small* **14**, 1703419 (2018). https://doi.org:https://doi.org/10.1002/smll.201703419

61   Jiang, Q. *et al.* Review of MXene electrochemical microsupercapacitors. *Energy Storage Materials* **27**, 78-95 (2020). https://doi.org:https://doi.org/10.1016/j.ensm.2020.01.018

62   Aslam, M. K. *et al.* 2D MXene Materials for Sodium Ion Batteries: A review on Energy Storage. *Journal of Energy Storage* **37**, 102478 (2021). https://doi.org:https://doi.org/10.1016/j.est.2021.102478

63   Kailasa, S. K., Joshi, D. J., Koduru, J. R. & Malek, N. I. Review on MXenes-based nanomaterials for sustainable opportunities in energy storage, sensing and electrocatalytic reactions. *Journal of Molecular Liquids* **342**, 117524 (2021). https://doi.org:https://doi.org/10.1016/j.molliq.2021.117524

64   Zhang, J. *et al.* Single platinum atoms immobilized on an MXene as an efficient catalyst for the hydrogen evolution reaction. *Nature Catalysis* **1**, 985-992 (2018). https://doi.org:10.1038/s41929-018-0195-1

65   Ran, J. *et al.* Ti3C2 MXene co-catalyst on metal sulfide photo-absorbers for enhanced visible-light photocatalytic hydrogen production. *Nat. Commun.* **8**, 13907 (2017). https://doi.org:10.1038/ncomms13907

66   Sinha, A. *et al.* MXene: An emerging material for sensing and biosensing. *TrAC Trends in Analytical Chemistry* **105**, 424-435 (2018). https://doi.org:https://doi.org/10.1016/j.trac.2018.05.021

67   Kalambate, P. K. *et al.* Recent advances in MXene–based electrochemical sensors and biosensors. *TrAC Trends in Analytical Chemistry* **120**, 115643 (2019). https://doi.org:https://doi.org/10.1016/j.trac.2019.115643

68   Sokol, M., Natu, V., Kota, S. & Barsoum, M. W. On the Chemical Diversity of the MAX Phases. *Trends in Chemistry* **1**, 210-223 (2019). https://doi.org:https://doi.org/10.1016/j.trechm.2019.02.016

69   Zhu, J. *et al.* Two-Dimensional Titanium Carbonitride Mxene for High-Performance Sodium Ion Batteries. *ACS Applied Nano Materials* **1**, 6854-6863 (2018). https://doi.org:10.1021/acsanm.8b01330

70   Khazaei, M., Ranjbar, A., Arai, M. & Yunoki, S. Topological insulators in the ordered double transition metals M'2M"C2 MXenes (M' = Mo, W; M" = Ti, Zr, Hf). *Physical Review B* **94**, 125152 (2016). https://doi.org:10.1103/PhysRevB.94.125152

71   Cheng, Y.-W., Dai, J.-H., Zhang, Y.-M. & Song, Y. Two-Dimensional, Ordered, Double Transition Metal Carbides (MXenes): A New Family of Promising Catalysts for the Hydrogen Evolution Reaction. *The Journal of Physical Chemistry C* **122**, 28113-28122 (2018). https://doi.org:10.1021/acs.jpcc.8b08914

72   Maughan, P. A. *et al.* Pillared Mo2TiC2 MXene for high-power and long-life lithium and sodium-ion batteries. *Nanoscale Advances* **3**, 3145-3158 (2021). https://doi.org:10.1039/D1NA00081K

73   Anasori, B. *et al.* Two-Dimensional, Ordered, Double Transition Metals Carbides (MXenes). *ACS Nano* **9**, 9507-9516 (2015). https://doi.org:10.1021/acsnano.5b03591

74   Barsoum, M. W. *MAX Phases: Properties of Machinable Ternary Carbides and Nitrides*. (WILEY, 2013).

75   Naguib, M., Mochalin, V. N., Barsoum, M. W. & Gogotsi, Y. 25th Anniversary Article: MXenes: A New Family of Two-Dimensional Materials. *Advanced Materials* **26**, 992-1005 (2014). https://doi.org:10.1002/adma.201304138

76   Naguib, M. *et al.* Two-Dimensional Transition Metal Carbides. *Acs Nano* **6**, 1322-1331 (2012). https://doi.org:10.1021/nn204153h

77   Ghidiu, M., Lukatskaya, M. R., Zhao, M. Q., Gogotsi, Y. & Barsoum, M. W. Conductive two-dimensional titanium carbide 'clay' with high volumetric capacitance. *Nature* **516**, 78-U171 (2014). https://doi.org:10.1038/nature13970

78   Liu, F. *et al.* Preparation of Ti3C2 and Ti2C MXenes by fluoride salts etching and methane adsorptive properties. *Appl. Surf. Sci.* **416**, 781-789 (2017). https://doi.org:https://doi.org/10.1016/j.apsusc.2017.04.239

79   Lu, J. *et al.* Tin+1Cn MXenes with fully saturated and thermally stable Cl terminations. *Nanoscale Advances* **1**, 3680-3685 (2019). https://doi.org:10.1039/C9NA00324J

80   Soundiraraju, B. & George, B. K. Two-Dimensional Titanium Nitride (Ti2N) MXene: Synthesis, Characterization, and Potential Application as Surface-Enhanced Raman Scattering Substrate. *Acs Nano* **11**, 8892-8900 (2017). https://doi.org:10.1021/acsnano.7b03129

81   Naguib, M. *et al.* New Two-Dimensional Niobium and Vanadium Carbides as Promising Materials for Li-Ion Batteries. *Journal of the American Chemical Society* **135**, 15966-15969 (2013). https://doi.org:10.1021/ja405735d

82   Halim, J. *et al.* Synthesis and Characterization of 2D Molybdenum Carbide (MXene). *Advanced Functional Materials* **26**, 3118-3127 (2016). https://doi.org:https://doi.org/10.1002/adfm.201505328

83   Urbankowski, P. *et al.* 2D molybdenum and vanadium nitrides synthesized by ammoniation of 2D transition metal carbides (MXenes). *Nanoscale* **9**, 17722-17730 (2017). https://doi.org:10.1039/c7nr06721f

84   Abdelmalak, M. N. *MXenes: A New Family of Two-Dimensional Materials and its Application as Electrodes for Li-ion Batteries* Doctor of Philoshopy thesis, Drexel University, (2014).

85   Persson, I. *et al.* Tailoring Structure, Composition, and Energy Storage Properties of MXenes from Selective Etching of In-Plane, Chemically Ordered MAX Phases. *Small* **14**, 1703676 (2018). https://doi.org:https://doi.org/10.1002/smll.201703676

86   Tao, Q. *et al.* Two-dimensional Mo1.33C MXene with divacancy ordering prepared from parent 3D laminate with in-plane chemical ordering. *Nat. Commun.* **8**, 14949 (2017). https://doi.org:10.1038/ncomms14949

87   Meshkian, R. *et al.* W-Based Atomic Laminates and Their 2D Derivative W1.33C MXene with Vacancy Ordering. *Advanced Materials* **30**, 1706409 (2018). https://doi.org:https://doi.org/10.1002/adma.201706409

88   Halim, J. *et al.* Synthesis of Two-Dimensional Nb1.33C (MXene) with Randomly Distributed Vacancies by Etching of the Quaternary Solid Solution (Nb2/3Sc1/3)2AlC MAX Phase. *ACS Applied Nano Materials* **1**, 2455-2460 (2018). https://doi.org:10.1021/acsanm.8b00332

89   Halim, J. *et al.* Transparent Conductive Two-Dimensional Titanium Carbide Epitaxial Thin Films. *Chem. Mat.* **26**, 2374-2381 (2014). https://doi.org:10.1021/cm500641a

90   Li, T. *et al.* Fluorine-Free Synthesis of High-Purity Ti3C2Tx (T=OH, O) via Alkali Treatment. *Angewandte Chemie International Edition* **57**, 6115-6119 (2018). https://doi.org:https://doi.org/10.1002/anie.201800887

91   Alhabeb, M. *et al.* Selective Etching of Silicon from Ti3SiC2 (MAX) To Obtain 2D Titanium Carbide (MXene). *Angewandte Chemie International Edition* **57**, 5444-5448 (2018). https://doi.org:https://doi.org/10.1002/anie.201802232

92   Zhou, J. *et al.* A Two-Dimensional Zirconium Carbide by Selective Etching of Al3C3 from Nanolaminated Zr3Al3C5. *Angewandte Chemie International Edition* **55**, 5008-5013 (2016). https://doi.org:https://doi.org/10.1002/anie.201510432

93   Zhou, J. *et al.* Synthesis and Electrochemical Properties of Two-Dimensional Hafnium Carbide. *ACS Nano* **11**, 3841-3850 (2017). https://doi.org:10.1021/acsnano.7b00030

94   Meshkian, R. *et al.* Theoretical stability and materials synthesis of a chemically ordered MAX phase, Mo2ScAlC2, and its two-dimensional derivate Mo2ScC2 MXene. *Acta Materialia* **125**, 476-480 (2017). https://doi.org:https://doi.org/10.1016/j.actamat.2016.12.008

95   Urbankowski, P. *et al.* Synthesis of two-dimensional titanium nitride Ti4N3 (MXene). *Nanoscale* **8**, 11385-11391 (2016). https://doi.org:10.1039/c6nr02253g

96   Ghidiu, M. *et al.* Synthesis and characterization of two-dimensional Nb4C3 (MXene). *Chem. Commun.* **50**, 9517-9520 (2014). https://doi.org:10.1039/C4CC03366C

97   Tran, M. H. *et al.* Adding a New Member to the MXene Family: Synthesis, Structure, and Electrocatalytic Activity for the Hydrogen Evolution Reaction of V4C3Tx. *ACS Applied Energy Materials* **1**, 3908-3914 (2018). https://doi.org:10.1021/acsaem.8b00652

98   Yang, J. *et al.* Two-Dimensional Nb-Based M4C3 Solid Solutions (MXenes). *Journal of the American Ceramic Society* **99**, 660-666 (2016). https://doi.org:https://doi.org/10.1111/jace.13922

99   Alhabeb, M. *et al.* Guidelines for Synthesis and Processing of Two-Dimensional Titanium Carbide (Ti3C2TX MXene). *Chem. Mat.* **29**, 7633-7644 (2017). https://doi.org:10.1021/acs.chemmater.7b02847

100   Liu, C.-Y. & Li, E. Y. Termination Effects of Pt/v-Tin+1CnT2 MXene Surfaces for Oxygen Reduction Reaction Catalysis. *ACS Appl. Mater. Interfaces* **11**, 1638-1644 (2019). https://doi.org:10.1021/acsami.8b17600

101   Lin, H. *et al.* Two-dimensional titanium carbide MXenes as efficient non-noble metal electrocatalysts for oxygen reduction reaction. *Science China Materials* **62**, 662-670 (2019). https://doi.org:10.1007/s40843-018-9378-3

102   Xie, X., Chen, S., Ding, W., Nie, Y. & Wei, Z. An extraordinarily stable catalyst: Pt NPs supported on two-dimensional Ti3C2X2 (X = OH, F) nanosheets for oxygen reduction reaction. *Chem. Commun.* **49**, 10112-10114 (2013). https://doi.org:10.1039/C3CC44428G

103   Zhang, C., Ma, B., Zhou, Y. & Wang, C. Highly active and durable Pt/MXene nanocatalysts for ORR in both alkaline and acidic conditions. *Journal of Electroanalytical Chemistry* **865**, 114142 (2020). https://doi.org:https://doi.org/10.1016/j.jelechem.2020.114142

104   Xu, C. *et al.* MXene (Ti3C2Tx) and Carbon Nanotube Hybrid-Supported Platinum Catalysts for the High-Performance Oxygen Reduction Reaction in PEMFC. *ACS Appl. Mater. Interfaces* **12**, 19539-19546 (2020). https://doi.org:10.1021/acsami.0c02446

105   Wang, R. *et al.* Pt nanowire/Ti3C2Tx-CNT hybrids catalysts for the high performance oxygen reduction reaction for high temperature PEMFC. *International Journal of Hydrogen Energy* **45**, 28190-28195 (2020). https://doi.org:https://doi.org/10.1016/j.ijhydene.2020.03.068

106   Lee, Y. *et al.* Support structure-catalyst electroactivity relation for oxygen reduction reaction on platinum supported by two-dimensional titanium carbide. *Nano Energy* **79**, 105363 (2021). https://doi.org:https://doi.org/10.1016/j.nanoen.2020.105363

107   Zhang, P. *et al.* The High-Performance Bifunctional Catalyst Pd/Ti3C2Tx–Carbon Nanotube for Oxygen Reduction Reaction and Hydrogen Evolution Reaction in Alkaline

Medium. *Energy Technology* **8**, 2000306 (2020). https://doi.org:https://doi.org/10.1002/ente.202000306

108   Peng, X. *et al.* Trifunctional Single-Atomic Ru Sites Enable Efficient Overall Water Splitting and Oxygen Reduction in Acidic Media. *Small* **16**, 2002888 (2020). https://doi.org:https://doi.org/10.1002/smll.202002888

109   Zhang, Z. *et al.* Self-Reduction Synthesis of New MXene/Ag Composites with Unexpected Electrocatalytic Activity. *ACS Sustain. Chem. Eng.* **4**, 6763-6771 (2016). https://doi.org:10.1021/acssuschemeng.6b01698

110   Li, Z. *et al.* The Marriage of the FeN4 Moiety and MXene Boosts Oxygen Reduction Catalysis: Fe 3d Electron Delocalization Matters. *Advanced Materials* **30**, 1803220 (2018). https://doi.org:https://doi.org/10.1002/adma.201803220

111   Zhang, Y. *et al.* In Situ Growth of Cobalt Nanoparticles Encapsulated Nitrogen-Doped Carbon Nanotubes among Ti3C2Tx (MXene) Matrix for Oxygen Reduction and Evolution. *Advanced Materials Interfaces* **5**, 1800392 (2018). https://doi.org:https://doi.org/10.1002/admi.201800392

112   Wang, W.-T. *et al.* When MOFs meet MXenes: superior ORR performance in both alkaline and acidic solutions. *J. Mater. Chem. A* **9**, 3952-3960 (2021). https://doi.org:10.1039/D0TA10811A

113   Chen, J. *et al.* Integrating MXene nanosheets with cobalt-tipped carbon nanotubes for an efficient oxygen reduction reaction. *J. Mater. Chem. A* **7**, 1281-1286 (2019). https://doi.org:10.1039/C8TA10574J

114   Wen, Y., Ma, C., Wei, Z., Zhu, X. & Li, Z. FeNC/MXene hybrid nanosheet as an efficient electrocatalyst for oxygen reduction reaction. *RSC Advances* **9**, 13424-13430 (2019). https://doi.org:10.1039/C9RA01330J

115   Jiang, L., Duan, J., Zhu, J., Chen, S. & Antonietti, M. Iron-Cluster-Directed Synthesis of 2D/2D Fe–N–C/MXene Superlattice-like Heterostructure with Enhanced Oxygen Reduction Electrocatalysis. *ACS Nano* **14**, 2436-2444 (2020). https://doi.org:10.1021/acsnano.9b09912

116   Chen, L. *et al.* Hybridization of Binary Non-Precious-Metal Nanoparticles with d-Ti3C2 MXene for Catalyzing the Oxygen Reduction Reaction. *ChemElectroChem* **5**, 3307-3314 (2018). https://doi.org:https://doi.org/10.1002/celc.201800693

117   Liu, J., Mi, L., Xing, Y., Wang, T. & Wang, F. Construction of Ti3C2 supported hybrid Co3O4/NCNTs composite as an efficient oxygen reduction electrocatalyst. *Renewable Energy* **160**, 1168-1173 (2020). https://doi.org:https://doi.org/10.1016/j.renene.2020.07.059

118   Xue, Q. *et al.* Mn3O4 nanoparticles on layer-structured Ti3C2 MXene towards the oxygen reduction reaction and zinc-air batteries. *J. Mater. Chem. A* **5**, 20818-20823 (2017). https://doi.org:10.1039/c7ta04532h

119   Lei, H. *et al.* Strongly Coupled NiCo2O4 Nanocrystal/MXene Hybrid through In Situ Ni/Co–F Bonds for Efficient Wearable Zn–Air Batteries. *ACS Appl. Mater. Interfaces* **12**, 44639-44647 (2020). https://doi.org:10.1021/acsami.0c11185

120   Yang, X. *et al.* Multiwall carbon nanotubes loaded with MoS2 quantum dots and MXene quantum dots: Non–Pt bifunctional catalyst for the methanol oxidation and oxygen reduction reactions in alkaline solution. *Appl. Surf. Sci.* **464**, 78-87 (2019). https://doi.org:https://doi.org/10.1016/j.apsusc.2018.09.069

121   Han, S. *et al.* Multi-dimensional hierarchical CoS2@MXene as trifunctional electrocatalysts for zinc-air batteries and overall water splitting. *Science China Materials* **64**, 1127-1138 (2021). https://doi.org:10.1007/s40843-020-1524-5

122   Lei, Y. *et al.* Synthesis of Porous N-Rich Carbon/MXene from MXene@Polypyrrole Hybrid Nanosheets as Oxygen Reduction Reaction Electrocatalysts. *Journal of The Electrochemical Society* **167**, 116503 (2020). https://doi.org:10.1149/1945-7111/aba15b

123   Yu, X., Yin, W., Wang, T. & Zhang, Y. Decorating g-C3N4 Nanosheets with Ti3C2 MXene Nanoparticles for Efficient Oxygen Reduction Reaction. *Langmuir* **35**, 2909-2916 (2019). https://doi.org:10.1021/acs.langmuir.8b03456

134

124   Chidhambaram, N. & Ravichandran, K. Single step transformation of urea into metal-free g-C3N4 nanoflakes for visible light photocatalytic applications. *Materials Letters* **207**, 44-48 (2017). https://doi.org:https://doi.org/10.1016/j.matlet.2017.07.040

125   Dong, F. *et al.* Efficient synthesis of polymeric g-C3N4 layered materials as novel efficient visible light driven photocatalysts. *Journal of Materials Chemistry* **21**, 15171-15174 (2011). https://doi.org:10.1039/c1jm12844b

126   Akhtar, K., Khan, S. A., Khan, S. B. & Asiri, A. M. in *Handbook of Materials Characterization*   (ed Surender Kumar Sharma) 113-145 (Springer International Publishing, 2018).

127   Joseph I. Goldstein, D. E. N., Joseph R. Micheal, Nichilas W.M. Ritchie, John Henry J. Scott, David C. Joy. *Scanning Electron Microscopy and X-Ray Microanalysis*. 4th edn, (Springer New York, NY, 2017).

128   Dollimore, D., Spooner, P. & Turner, A. The bet method of analysis of gas adsorption data and its relevance to the calculation of surface areas. *Surface Technology* **4**, 121-160 (1976). https://doi.org:https://doi.org/10.1016/0376-4583(76)90024-8

129   Lowell, S., Shields, J. E., Thomas, M. A. & Thommes, M. in *Characterization of Porous Solids and Powders: Surface Area, Pore Size and Density*   (eds S. Lowell, Joan E. Shields, Martin A. Thomas, & Matthias Thommes) 58-81 (Springer Netherlands, 2004).

130   Thommes, M. *et al.* Physisorption of gases, with special reference to the evaluation of surface area and pore size distribution (IUPAC Technical Report). *Pure and Applied Chemistry* **87**, 1051-1069 (2015).

131   Kupgan, G., Liyana-Arachchi, T. P. & Colina, C. M. NLDFT Pore Size Distribution in Amorphous Microporous Materials. *Langmuir* **33**, 11138-11145 (2017). https://doi.org:10.1021/acs.langmuir.7b01961

132   Watts , J. F. W., J. *Surface Analysis by XPS and AES*. (WILEY, 2019).

133   Halim, J. *et al.* X-ray photoelectron spectroscopy of select multi-layered transition metal carbides (MXenes). *Appl. Surf. Sci.* **362**, 406-417 (2016). https://doi.org:10.1016/j.apsusc.2015.11.089

134   Biesinger, M. C., Lau, L. W. M., Gerson, A. R. & Smart, R. S. C. Resolving surface chemical states in XPS analysis of first row transition metals, oxides and hydroxides: Sc, Ti, V, Cu and Zn. *Appl. Surf. Sci.* **257**, 887-898 (2010). https://doi.org:https://doi.org/10.1016/j.apsusc.2010.07.086

135   Jones, R. R., Hooper, D. C., Zhang, L., Wolverson, D. & Valev, V. K. Raman Techniques: Fundamentals and Frontiers. *Nanoscale Research Letters* **14**, 231 (2019). https://doi.org:10.1186/s11671-019-3039-2

136   Kuzmann, E., Homonnay, Z., Klencsár, Z. & Szalay, R. (57)Fe Mössbauer Spectroscopy as a Tool for Study of Spin States and Magnetic Interactions in Inorganic Chemistry. *Molecules* **26** (2021). https://doi.org:10.3390/molecules26041062

137   Park, E., Ostrovski, O., Zhang, J., Thomson, S. & Howe, R. Characterization of phases formed in the iron carbide process by X-ray diffraction, mossbauer, X-ray photoelectron spectroscopy, and raman spectroscopy analyses. *Metallurgical and Materials Transactions B* **32**, 839-845 (2001). https://doi.org:10.1007/s11663-001-0071-1

138   Seh, Z. W. *et al.* Two-Dimensional Molybdenum Carbide (MXene) as an Efficient Electrocatalyst for Hydrogen Evolution. *Acs Energy Letters* **1**, 589-594 (2016). https://doi.org:10.1021/acsenergylett.6b00247

139   Zhou, S., Yang, X., Pei, W., Liu, N. & Zhao, J. Heterostructures of MXenes and N-doped graphene as highly active bifunctional electrocatalysts. *Nanoscale* **10**, 10876-10883 (2018). https://doi.org:10.1039/C8NR01090K

140   Yu, Y., Zhou, J. & Sun, Z. Modulation engineering of 2D MXene-based compounds for metal-ion batteries. *Nanoscale* **11**, 23092-23104 (2019). https://doi.org:10.1039/C9NR08217D

141   Le, T. A., Tran, N. Q., Hong, Y., Kim, M. & Lee, H. Porosity-Engineering of MXene as a Support Material for a Highly Efficient Electrocatalyst toward Overall Water Splitting. *ChemSusChem* **13**, 945-955 (2020). https://doi.org:10.1002/cssc.201903222

142   Le, T. A., Tran, N. Q., Hong, Y. & Lee, H. Intertwined Titanium Carbide MXene within a 3 D Tangled Polypyrrole Nanowires Matrix for Enhanced Supercapacitor Performances. *Chemistry – A European Journal* **25**, 1037-1043 (2019). https://doi.org:10.1002/chem.201804291

143   Cho, W., Lee, S.-H., Ju, W.-S., Baek, Y. & Lee, J. K. Conversion of natural gas to hydrogen and carbon black by plasma and application of plasma carbon black. *Catalysis Today* **98**, 633-638 (2004). https://doi.org:https://doi.org/10.1016/j.cattod.2004.09.051

144   Pérez-Rodríguez, S., Pastor, E. & Lázaro, M. J. Electrochemical behavior of the carbon black Vulcan XC-72R: Influence of the surface chemistry. *International Journal of Hydrogen Energy* **43**, 7911-7922 (2018). https://doi.org:https://doi.org/10.1016/j.ijhydene.2018.03.040

145   Luo, J. *et al.* Pillared Structure Design of MXene with Ultralarge Interlayer Spacing for High-Performance Lithium-Ion Capacitors. *ACS Nano* **11**, 2459-2469 (2017). https://doi.org:10.1021/acsnano.6b07668

146   Hu, T. *et al.* Vibrational properties of Ti3C2 and Ti3C2T2 (T = O, F, OH) monosheets by first-principles calculations: a comparative study. *Physical Chemistry Chemical Physics* **17**, 9997-10003 (2015). https://doi.org:10.1039/C4CP05666C

147   Hu, M. *et al.* High-Capacitance Mechanism for Ti3C2Tx MXene by in Situ Electrochemical Raman Spectroscopy Investigation. *ACS Nano* **10**, 11344-11350 (2016). https://doi.org:10.1021/acsnano.6b06597

148   Peng, Q. *et al.* Unique Lead Adsorption Behavior of Activated Hydroxyl Group in Two-Dimensional Titanium Carbide. *Journal of the American Chemical Society* **136**, 4113-4116 (2014). https://doi.org:10.1021/ja500506k

149   Maughan, P. A. *Porous Two-Dimensional Materials (MXenes) for High Capacity Energy Storage*, Lancaster University (United Kingdom), (2020).

150   Overbury, S. H. *et al.* Complexity of Intercalation in MXenes: Destabilization of Urea by Two-Dimensional Titanium Carbide. *Journal of the American Chemical Society* **140**, 10305-10314 (2018). https://doi.org:10.1021/jacs.8b05913

151   Meng, F. *et al.* MXene Sorbents for Removal of Urea from Dialysate: A Step toward the Wearable Artificial Kidney. *ACS Nano* **12**, 10518-10528 (2018). https://doi.org:10.1021/acsnano.8b06494

152   Liu, J. H., Zhang, T. K., Wang, Z. C., Dawson, G. & Chen, W. Simple pyrolysis of urea into graphitic carbon nitride with recyclable adsorption and photocatalytic activity. *Journal of Materials Chemistry* **21**, 14398-14401 (2011). https://doi.org:10.1039/c1jm12620b

153   Mohamed, B. *et al.* One MAX phase, different MXenes: A guideline to understand the crucial role of etching conditions on Ti3C2Tx surface chemistry. *Appl. Surf. Sci.* **530**, 147209 (2020). https://doi.org:https://doi.org/10.1016/j.apsusc.2020.147209

154   Ajikumar, P. K. *et al.* Synthesis, characterization and evaluation of titanium carbonitride surface layers with varying concentrations of carbon and nitrogen. *Ceramics International* **38**, 2253-2259 (2012). https://doi.org:https://doi.org/10.1016/j.ceramint.2011.10.075

155   Seredych, M. *et al.* High-Temperature Behavior and Surface Chemistry of Carbide MXenes Studied by Thermal Analysis. *Chem. Mat.* **31**, 3324-3332 (2019). https://doi.org:10.1021/acs.chemmater.9b00397

156   Persson, I. *et al.* On the organization and thermal behavior of functional groups on Ti 3 C 2 MXene surfaces in vacuum. *2D Materials* **5**, 015002 (2017). https://doi.org:10.1088/2053-1583/aa89cd

157   Persson, I. *et al.* 2D Transition Metal Carbides (MXenes) for Carbon Capture. *Advanced Materials* **31**, 1805472 (2019). https://doi.org:10.1002/adma.201805472

158   Yang, C. *et al.* Flexible Nitrogen-Doped 2D Titanium Carbides (MXene) Films Constructed by an Ex Situ Solvothermal Method with Extraordinary Volumetric Capacitance. *Advanced Energy Materials* **8**, 1802087 (2018). https://doi.org:https://doi.org/10.1002/aenm.201802087

159   Cui, X., Meng, L., Zhang, X., Wang, X. & Shi, J. Heterogeneous atoms-doped titanium carbide as a precious metal-free electrocatalyst for oxygen reduction reaction. *Electrochim. Acta* **295**, 384-392 (2019). https://doi.org:https://doi.org/10.1016/j.electacta.2018.10.169

160   Yang, C. *et al.* Improved capacitance of nitrogen-doped delaminated two-dimensional titanium carbide by urea-assisted synthesis. *Electrochim. Acta* **225**, 416-424 (2017). https://doi.org:https://doi.org/10.1016/j.electacta.2016.12.173

161   Ahmed, B., Anjum, D. H., Hedhili, M. N., Gogotsi, Y. & Alshareef, H. N. H2O2 assisted room temperature oxidation of Ti2C MXene for Li-ion battery anodes. *Nanoscale* **8**, 7580-7587 (2016). https://doi.org:10.1039/c6nr00002a

162   Rakhi, R. B., Ahmed, B., Hedhili, M. N., Anjum, D. H. & Alshareef, H. N. Effect of Postetch Annealing Gas Composition on the Structural and Electrochemical Properties of Ti2CTx MXene Electrodes for Supercapacitor Applications. *Chem. Mat.* **27**, 5314-5323 (2015). https://doi.org:10.1021/acs.chemmater.5b01623

163   Sharma, S. *et al.* Rapid Microwave Synthesis of CO Tolerant Reduced Graphene Oxide-Supported Platinum Electrocatalysts for Oxidation of Methanol. *The Journal of Physical Chemistry C* **114**, 19459-19466 (2010). https://doi.org:10.1021/jp107872z

164   Wu, X., Chen, F., Wang, X. & Yu, H. In situ one-step hydrothermal synthesis of oxygen-containing groups-modified g-C3N4 for the improved photocatalytic H2-evolution performance. *Appl. Surf. Sci.* **427**, 645-653 (2018). https://doi.org:https://doi.org/10.1016/j.apsusc.2017.08.050

165   Yuan, Y. *et al.* High-yield synthesis and optical properties of g-C3N4. *Nanoscale* **7**, 12343-12350 (2015). https://doi.org:10.1039/C5NR02905H

166   Ge, L. & Han, C. Synthesis of MWNTs/g-C3N4 composite photocatalysts with efficient visible light photocatalytic hydrogen evolution activity. *Applied Catalysis B: Environmental* **117-118**, 268-274 (2012). https://doi.org:https://doi.org/10.1016/j.apcatb.2012.01.021

167   Ayiania, M. *et al.* Deconvoluting the XPS spectra for nitrogen-doped chars: An analysis from first principles. *Carbon* **162**, 528-544 (2020). https://doi.org:https://doi.org/10.1016/j.carbon.2020.02.065

168   Tang, Y. *et al.* The effect of in situ nitrogen doping on the oxygen evolution reaction of MXenes. *Nanoscale Advances* **2**, 1187-1194 (2020). https://doi.org:10.1039/C9NA00706G

169   Lu, C. *et al.* Nitrogen-Doped Ti3C2 MXene: Mechanism Investigation and Electrochemical Analysis. *Advanced Functional Materials* **30**, 2000852 (2020). https://doi.org:https://doi.org/10.1002/adfm.202000852

170   Wen, Y. *et al.* Nitrogen-doped Ti3C2Tx MXene electrodes for high-performance supercapacitors. *Nano Energy* **38**, 368-376 (2017). https://doi.org:https://doi.org/10.1016/j.nanoen.2017.06.009

171   Ma, T. Y., Cao, J. L., Jaroniec, M. & Qiao, S. Z. Interacting Carbon Nitride and Titanium Carbide Nanosheets for High-Performance Oxygen Evolution. *Angew. Chem.-Int. Edit.* **55**, 1138-1142 (2016). https://doi.org:10.1002/anie.201509758

172   Tahir, M. *et al.* One Dimensional Graphitic Carbon Nitrides as Effective Metal-Free Oxygen Reduction Catalysts. *Scientific Reports* **5**, 12389 (2015). https://doi.org:10.1038/srep12389

173   Zhutaeva, G. V., Bogdanovskaya, V. A., Davydova, E. S., Kazanskii, L. P. & Tarasevich, M. R. Kinetics and mechanism of oxygen electroreduction on Vulcan XC72R carbon black modified by pyrolysis products of cobalt 5,10,15,20-tetrakis(4-methoxyphenyl)porphyrine in a broad pH interval. *Journal of Solid State Electrochemistry* **18**, 1319-1334 (2014). https://doi.org:10.1007/s10008-013-2233-x

174   Huang, J.-J. *et al.* A facile method to produce MoSe2/MXene hybrid nanoflowers with enhanced electrocatalytic activity for hydrogen evolution. *Journal of Electroanalytical Chemistry* **856**, 113727 (2020). https://doi.org:https://doi.org/10.1016/j.jelechem.2019.113727

175   Yang, W., Liu, X., Yue, X., Jia, J. & Guo, S. Bamboo-like Carbon Nanotube/Fe3C Nanoparticle Hybrids and Their Highly Efficient Catalysis for Oxygen Reduction. *J. Am. Chem. Soc.* **137**, 1436 (2015).

176   Jiang, W. J. *et al.* Understanding the High Activity of Fe–N–C Electrocatalysis in Oxygen Reduction: Fe/Fe3C Nanoparticles Boost the Activity of Fe–Nx. *J. Am. Chem. Soc.* **138**, 3570 (2016).

177   Sun, X. *et al.* Atomic-Level Fe-N-C Coupled with Fe3C-Fe Nanocomposites in Carbon Matrixes as High-Efficiency Bifunctional Oxygen Catalysts. *Small* **16**, 1906057 (2020). https://doi.org:https://doi.org/10.1002/smll.201906057

178   Kim, J. H., Sa, Y. J., Jeong, H. Y. & Joo, S. H. Roles of Fe−Nx and Fe−Fe3C@C Species in Fe−N/C Electrocatalysts for Oxygen Reduction Reaction. *ACS Appl. Mater. Interfaces* **9**, 9567-9575 (2017). https://doi.org:10.1021/acsami.6b13417

179   He, Z. *et al.* Iron Catalysts for the Growth of Carbon Nanofibers: Fe, Fe3C or Both? *Chem. Mat.* **23**, 5379-5387 (2011). https://doi.org:10.1021/cm202315j

180   Lukatskaya, M. R. *et al.* Cation Intercalation and High Volumetric Capacitance of Two-Dimensional Titanium Carbide. *Science* **341**, 1502-1505 (2013). https://doi.org:doi:10.1126/science.1241488

181   Osti, N. C. *et al.* Influence of metal ions intercalation on the vibrational dynamics of water confined between MXene layers. *Physical Review Materials* **1**, 065406 (2017). https://doi.org:10.1103/PhysRevMaterials.1.065406

182   Kramm, U. I., Lefèvre, M., Larouche, N., Schmeisser, D. & Dodelet, J.-P. Correlations between Mass Activity and Physicochemical Properties of Fe/N/C Catalysts for the ORR in PEM Fuel Cell via 57Fe Mössbauer Spectroscopy and Other Techniques. *Journal of the American Chemical Society* **136**, 978-985 (2014). https://doi.org:10.1021/ja410076f

183   Zhong, L. *et al.* 57Fe-Mössbauer spectroscopy and electrochemical activities of graphitic layer encapsulated iron electrocatalysts for the oxygen reduction reaction. *Applied Catalysis B: Environmental* **221**, 406-412 (2018). https://doi.org:https://doi.org/10.1016/j.apcatb.2017.09.014

184   Guoyu, Z., Hongjuan, W., Hao, Y. & Feng, P. Nitrogen doped carbon nanotubes with encapsulated ferric carbide as excellent electrocatalyst for oxygen reduction reaction in acid and alkaline media. *Journal of Power Sources* **286**, 495-503 (2015). https://doi.org:https://doi.org/10.1016/j.jpowsour.2015.04.021

185   Wilson, D. & Langell, M. A. XPS analysis of oleylamine/oleic acid capped Fe3O4 nanoparticles as a function of temperature. *Appl. Surf. Sci.* **303**, 6-13 (2014). https://doi.org:https://doi.org/10.1016/j.apsusc.2014.02.006

186   Chen, Y. *et al.* Isolated Single Iron Atoms Anchored on N-Doped Porous Carbon as an Efficient Electrocatalyst for the Oxygen Reduction Reaction. *Angewandte Chemie International Edition* **56**, 6937-6941 (2017). https://doi.org:https://doi.org/10.1002/anie.201702473

187   Liu, W. *et al.* Discriminating Catalytically Active FeNx Species of Atomically Dispersed Fe–N–C Catalyst for Selective Oxidation of the C–H Bond. *Journal of the American Chemical Society* **139**, 10790-10798 (2017). https://doi.org:10.1021/jacs.7b05130

188   García, Á. *et al.* Study of the evolution of FeNxCy and Fe3C species in Fe/N/C catalysts during the oxygen reduction reaction in acid and alkaline electrolyte. *Journal of Power Sources* **490**, 229487 (2021). https://doi.org:https://doi.org/10.1016/j.jpowsour.2021.229487

189   Wen, Z. *et al.* Nitrogen-Enriched Core-Shell Structured Fe/Fe3C-C Nanorods as Advanced Electrocatalysts for Oxygen Reduction Reaction. *Adv. Mater.* **24**, 1399 (2012).

190   Zhou, R., Zheng, Y., Jaroniec, M. & Qiao, S.-Z. Determination of the Electron Transfer Number for the Oxygen Reduction Reaction: From Theory to Experiment. *ACS Catal.* **6**, 4720-4728 (2016). https://doi.org:10.1021/acscatal.6b01581

191   Takeyasu, K., Furukawa, M., Shimoyama, Y., Singh, S. K. & Nakamura, J. Role of Pyridinic Nitrogen in the Mechanism of the Oxygen Reduction Reaction on Carbon Electrocatalysts. *Angewandte Chemie International Edition* **60**, 5121-5124 (2021). https://doi.org:https://doi.org/10.1002/anie.202014323

APPENDIX A: XPS peak-fitting

The peak-fitting of X-ray Photoelectron Spectroscopy (XPS) spectra has been performed using CasaXPS but can be performed using other available XPS curve fitting software.

To attempt to get a more precise deconvolution of the different peaks in the XPS spectra, several constraints were applied during the peak-fitting of the samples. The constraints are as follow and were met for most of the components during the fitting:

- Despite the fact that higher binding energy tails have been reported for MXenes in other studies[133], which would require a peak-fitting with asymmetric Gaussian-Lorentzian peaks, a gaussian-type distribution was chosen to make the deconvolution easier. It was assumed that a deconvolution of the XPS spectra with Gaussian components would not prejudice the analysis of the surface chemistry of the samples.

- The different component and their initial binding energy values were taken and based on studies focusing on the chemistry of MXenes, especially Ti_3C_2, carbides, nitrides, carbons, and N-doped carbons materials.

- The binding energy shift for a given component was constrained within a $\pm$ 0.5 eV window around the initial value.

- The full width at half maximum (FWHM) of a specific component was set, so that its value for a specific component would be similar in the different samples which would contain it.

In addition to these restrictions, another parameter specific to the Ti 2p spectra peak-fitting has been considered due to the $2p_{1/2}$ and $2p_{3/2}$ components:

- The peak splitting was kept within a window of 5 to 6 eV, as it englobes the values which have generally been reported for the peak splitting between Ti $2p_{1/2}$ and Ti $2p_{3/2}$ for different Ti oxidation states.[134]

- The intensity ratio between the Ti $2p_{1/2}$ and Ti $2p_{3/2}$ has also been restricted as follow:

$$I_{2p_{3/2}} = {I_{2p_{1/2}}}/{2}$$

Except for a few cases, the different constraints set for the deconvolution of the broad XPS peaks were met. The peak-fitting results for the different samples are given in the following tables.

Table 7.1: Ti2p XPS peak fitting

	Ti-C $2p_{1/2}$ / $2p_{3/2}$	**Ti^{2+}** $2p_{1/2}$ / $2p_{3/2}$	**Ti^{3+}** $2p_{1/2}$ / $2p_{3/2}$	**Ti^{4+}** $2p_{1/2}$ / $2p_{3/2}$
Ti$_3$C$_2$-550	Residual: 1.424			
Position (B.E. eV)	454.95 / 460.60	456.18 / 461.81	457.30 / 462. 77	458.98 / 464. 68
FWHM (eV)	1.5 / 2.0	1.3 / 1.9	1.2 / 2.5	1.3 / 2.3
Ti$_3$C$_2$-U1-550	Residual: 1.383			
Position (B.E. eV)	455.19 / 460. 61	456.21 / 461.68	457.29 / 463.10	458.61 / 464.27
FWHM (eV)	1.0 / 2.0	1.6 / 2.0	1.0 / 2.5	1.4 / 2.5
Ti$_3$C$_2$-U10-550	Residual: 2.110			
Position (B.E. eV)	455.25 / 460.59	456.30 / 461.75	457.29 / 462.79	458.60 / 464.25
FWHM (eV)	1.3 / 2.0	1.1 / 1.8	1.2 / 2.5	1.3 / 2.4
Ti$_3$C$_2$-U50-550	Residual: 0.586			
Position (B.E. eV)	455.30 / 460.80	456.22 / 461.60	457.30 / 463.10	458.60 / 464.73
FWHM (eV)	1.9 / 2.0	0.5 / 2	1.8 / 2.5	1.5 / 2.4
Ti$_3$C$_2$-U10-800	Residual: 1.082			
Position (B.E. eV)	455.31 / 460.00	456.20 / 461.38	457.39 / 462.64	458.72 / 464.38
FWHM (eV)	1.0 / 1.9	1.5 / 1.9	1.4 / 2.0	1.3 / 2.1
Ti$_3$C$_2$-U50-800	Residual: 1.805			
Position (B.E. eV)	455.17 / 460.02	456.37 / 461.52	457.79 / 462.90	458.70 / 464.38
FWHM (eV)	1.0 / 2.0	1.4 / 2.0	1.4 / 2.0	1.2 / 1.4
Ti$_3$C$_2$-U10-Fe-800	Residual: 0.894			
Position (B.E. eV)	455.20 / 460.01	456.20 / 461.00	457.66 / 462.77	458.70 / 464.37
FWHM (eV)	0.7 / 1.0	1.5 / 2.0	1.6 / 2.0	1.3 / 1.9
Ti$_3$C$_2$-U50-Fe-800	Residual: 1.193			
Position (B.E. eV)	455.35 / 460.06	456.40 / 461.45	457.73 / 462.90	458.70 / 464.39
FWHM (eV)	1.1 / 2.0	1.3 / 1.9	1.7 / 2.0	1.2 / 1.5

Table 7.2: C1s XPS peak fitting

	C-Ti	**C-Fe**	**C-C**	**C-O**	**N-C=N**	**C-F**	**π-π***
Ti$_3$C$_2$-550	Residual: 1.352						
Position (B.E. eV)	281.81	-	284.76	286.25	-	288.76	-
FWHM (eV)	1.5	-	2.0	2.0	-	2.0	-
Ti$_3$C$_2$-U1-550	Residual: 0.968						
Position (B.E. eV)	281.88	-	284.75	286.16	288.29	289.15	-
FWHM (eV)	0.9	-	1.4	2.0	1.8	1.9	-
Ti$_3$C$_2$-U10-550	Residual: 1.140						
Position (B.E. eV)	281.39	-	284.40	286.26	288.16	288.75	-
FWHM (eV)	0.8	-	1.5	1.9	1.5	1.9	-
Ti$_3$C$_2$-U50-550	Residual: 1.640						
Position (B.E. eV)	-	-	284.79	286.39	288.22	-	-
FWHM (eV)	-	-	1.4	1.3	1.3	-	-
Ti$_3$C$_2$-U10-800	Residual: 1.499						
Position (B.E. eV)	282.07	-	284.78	286.21	288.54	-	-
FWHM (eV)	1.4	-	0.9	1.6	2.1	-	-
Ti$_3$C$_2$-U50-800	Residual: 0.746						
Position (B.E. eV)	281.91	-	284.69	286.00	288.22	-	290.54
FWHM (eV)	0.9	-	1.5	2.0	2.4	-	3.0
Ti$_3$C$_2$-U10-Fe-800	Residual: 2.278						
Position (B.E. eV)	-	283.87	284.81	285.80	287.86	-	290.47
FWHM (eV)	-	0.9	0.9	1.8	2.0	-	3.0
Ti$_3$C$_2$-U50-Fe-800	Residual: 1.171						

Position (B.E. eV)	-	283.90	284.77	285.80	287.85	-	290.27
FWHM (eV)	-	1.5	1.1	1.9	2.0	-	3.0
C-U50-Fe-800	Residual: 3.155						
Position (B.E. eV)	-	283.92	284.82	285.80	287.80	-	290.56
FWHM (eV)	-	0.9	0.9	1.9	2.0	-	3.0

Table 7.3: N1s XPS peak fitting

	N-Ti	**N1 (pyridinic)**	**N2 (pyrrolic)**	**N3 (graphitic)**
Ti₃C₂-U1-550	Residual: 0.796			
Position (B.E. eV)	396.31	398.60	400.50	401.73
FWHM (eV)	1.2	2.1	1.6	2.3
Ti₃C₂-U10-550	Residual: 1.042			
Position (B.E. eV)	396.30	398.47	400.36	401.40
FWHM (eV)	1.3	2.6	1.2	1.0
Ti₃C₂-U50-550	Residual: 4.437			
Position (B.E. eV)	-	398.59	399.73	401.40
FWHM (eV)	-	1.2	2.0	1.1
Ti₃C₂-U10-800	Residual: 2.660			
Position (B.E. eV)	396.50	398.71	400.59	401.66
FWHM (eV)	1.6	2.2	1.2	1.2
Ti₃C₂-U50-800	Residual: 1.512			
Position (B.E. eV)	396.39	398.51	400.10	401.00
FWHM (eV)	1.7	1.9	1.6	2.0
Ti₃C₂-U10-Fe-800	Residual: 1.065			
Position (B.E. eV)	396.73	398.72	400.56	401.26
FWHM (eV)	1.5	1.9	2.0	1.9
Ti₃C₂-U50-Fe-800	Residual: 0.981			
Position (B.E. eV)	396.54	398.57	400.54	401.14
FWHM (eV)	1.6	1.9	2.0	2.0
C-U50-Fe-800	Residual: 0.844			
Position (B.E. eV)	-	398.80	400.49	401.67
FWHM (eV)	-	1.5	2.0	1.7

APPENDIX B: ^{57}Fe Mössbauer analysis parameters

The Fe-species assignment of the deconvolution is based on literature.[137,182,183]

Table 7.4: Site parameters and composition for Ti$_3$C$_2$-U50-800 sample

	CS (mm/s)	Δ (mm/s)	A (counts.mm/s)	w$_+$ (mm/s)	A$_-$/A$_+$	w$_-$/w$_+$	Composition
Doublet 1	0.409 (81)	0.91 (14)	4590 (820)	0.38 (12)	1*	1*	18.3 (33)
	CS (mm/s)	**ε (mm/s)**	**A (counts.mm/s)**	**H (T)**	**w$_3$ (mm/s)**		
Sextet 1	-0.034 (46)	0.034 (45)	6000 (1300)	32.84 (26)	0.207 (57)		23.8 (53)
Sextet 2	0.192 (15)	0.010 (15)	14500 (1200)	20.80 (11)	0.192 (20)		57.9 (48)

Reduced χ^2 = 0.543452

Table 7.5: Site parameters and composition for Ti$_3$C$_2$-U10-800 sample

	CS (mm/s)	Δ (mm/s)	A (counts.mm/s)	w$_+$ (mm/s)	A$_-$/A$_+$	w$_-$/w$_+$	Composition
Doublet 1	0.315 (31)	0.916 (52)	5450 (470)	0.291 (41)	1*	1*	15.8 (14)
	CS (mm/s)	**ε (mm/s)**	**A (counts.mm/s)**	**H (T)**	**w$_3$ (mm/s)**		
Sextet 1	0.002 (21)	0.023 (21)	5440 (740)	33.43 (12)	0.155 (27)		15.8 (21)
Sextet 2	0.1922 (63)	0.0070 (63)	23520 (770)	20.313 (47)	0.1989 (85)		68.3 (22)

Reduced χ^2 = 0.831822

Table 7.6: Site parameters and composition for C-U50-800 sample

	CS (mm/s)	Δ (mm/s)	A (counts.mm/s)	w$_+$ (mm/s)	A$_-$/A$_+$	w$_-$/w$_+$	Composition
Doublet 1	0.275 (55)	0.75 (10)	1730 (390)	0.202 (72)	1*	1*	7.0 (16)
	CS (mm/s)	**ε (mm/s)**	**A (counts.mm/s)**	**H (T)**	**w$_3$ (mm/s)**		
Sextet 1	-0.040 (39)	0.063 (39)	1470 (570)	33.16 (25)	0.099 (52)		6.0 (23)
Sextet 2	0.1942 (55)	0.0050 (54)	21360 (720)	20.796 (39)	0.1655 (73)		87.0 (29)

Reduced χ^2 = 0.695895